Plasma-based Surface Nanopatterning of Semiconductor Materials Using Block Copolymer Lithography

A thesis submitted to Dublin City University for the award of PhD by Shauna Flynn B.Sc., M.Sc.

Dublin City University
School of Electronic Engineering

2018

Supervisors:

Dr Susan Kelleher
School of Chemistry
University College Dublin
Belfield
Dublin 4

and

Dr Stephen Daniels
School of Electronic Engineering
Dublin City University
Glasnevin
Dublin 9

Declaration

I hereby certify that this material, which I now submit for assessment on the programme of study leading to the award of PhD is entirely my own work, and that I have exercised reasonable care to ensure that the work is original, and does not to the best of my knowledge breach any law of copyright, and has not been taken from the work of others save and to the extent that such work has been cited and acknowledged within the text of my work.

Signed:

____

ID Number:

____

Date:

____

Acknowledgements

I owe my sincere gratitude to every person whom has made this thesis possible and who has helped me directly and indirectly throughout my research career. I cannot begin to express my whole-hearted thanks to everyone. My most sincere thanks go to my funding agencies, Irish Research Council and Intel Ireland, without them this work would not be possible. To all members of the Kelleher Nanobiomaterials Research Group, thank you all for your help and for the meticulous proofreading, I'm very grateful. I would like to personally thank Conor Murphy for always being there to help when problems arose with the plasma tool. Huge thanks to Dr Ross Lundy and Dr Justin Bogan for contributing largely to this work and for their continuous support and motivation. Thank you to Susan Mulansky who performed the cell experiments. I would like to thank my Intel mentor, Matt Shaw, for always providing help whenever it was needed and for his encouragement throughout.

To my PhD supervisors, Dr Stephen Daniels and Dr Susan Kelleher. Stephen, you have been a strong support and provided me with excellent guidance over the past 5 years. You continue to impress me with your successful career, inside and out of academia. I will forever be grateful to you for taking me on as a research student. Susan, you inspire me every day. You have been a wonderful supervisor and friend. I consider myself very lucky to have done my PhD under your supervision. You provided me with endless direction and encouragement, and motivated me when times were difficult. I cannot thank you enough for all you have done for me. I look forward to working together in the future.

To my parents – Jackie and Vinny, and my siblings – Kate, Eoghan and Aoife, thank you for supporting me throughout my undergraduate and postgraduate degrees, I am very grateful and lucky to have such strong support behind me always. Kate and Mark, I cannot thank you both enough for the endless encouragement and help with proofreading this thesis. Finally, to Cian, I don't think I would have come so far without you by my side. Your support, reassurance and continuous encouragement was priceless.

Table of Contents

Publications

1. **S. P. Flynn**, R. Monaghan, J. Bogan, M, McKenna, A. Cowley, S. Daniels, G. Hughes and S. M. Kelleher. "Controlling wettability of PECVD-deposited dual organosilicon/carboxylic acid films to influence DNA hybridisation assay efficiency" Journal *of Materials Chemistry B,* 2017, 42, 8378-8388.
2. R. Lundy, **S. P. Flynn**, C. Cummins, S. M. Kelleher, M. N. Collins, E. Dalton, S. Daniels, M. A. Morris, and R. Enright. "Controlled Solvent Vapor Annealing of a High χ Block Copolymer Thin Film". *Physical Chemistry Chemical Physics*, 2017, 19, 2805-2815.
3. **S. P. Flynn**, M. McKenna, R. Monaghan, S. M. Kelleher, S. Daniels, and A. MacCormac. "Aqua-art: A demonstration of hydrophilic and hydrophobic surfaces fabricated by plasma enhanced chemical vapour deposition". *ACS Journal of Chemical Education*, 2017, 94, 221–225.
4. R. Lundy, **S. P. Flynn**, C. Cummins, S. M. Kelleher, M. N. Collins, E. Dalton, S. Daniels, M. Morris, R. Enright. "Nanoporous membrane production via block copolymer lithography for high heat dissipation systems." *Thermal and Thermomechanical Phenomena in Electronic Systems (ITherm), 2016 15th IEEE Intersociety Conference on*. IEEE, 2016.
5. **S. P. Flynn**, S. M. Kelleher, J. N. Alcorn, D. Kurzbuch, S. Daniels, C. McDonagh, E. Clancy, T. J. Smith and R. Nooney. "Ultrasensitive microarray bioassays using cyanine5 dye-doped silica nanoparticles". *Nanotechnology,* 2016*,* 27, 465501.
6. S. M. Kelleher, R. Nooney, **S. P. Flynn**, E. Clancy, M. Burke, S. Daly, T. J. Smith, S. Daniels and C. McDonagh. "Multivalent linkers for improved covalent binding of oligonucleotides to dye-doped silica nanoparticles". *Nanotechnology,* 2015*,* 26, 365703.
7. **S. P. Flynn**, J. Bogan, R. Lundy, K. Eltayeb, M. Shaw, S. Daniels, G. Hughes and S. M. Kelleher. "Selective removal of poly(4-vinyl-pyridine) from poly(styrene)-block-poly(4-vinyl-pyridine) block copolymer film using a controlled nitrogen reactive ion etch process" (to be submitted)
8. **S. P. Flynn**, R. Lundy, G. Reid, S. Mulansky, C. Cummins, R. Enright, S. Daniels and S. M. Kelleher. "The fabrication of silicon and poly (ethylene glycol) diacrylate nanopillars for antibacterial applications" (to be submitted)
9. **S. P. Flynn**, J. Koehne, B. Rodriguez, F. Bayer, Stephen Daniels and S. M. Kelleher. "Replica molding of nanostructured cicada wings". (to be submitted)

Conference Presentations

1. Oral and Poster Presentation: “Block copolymer solvent vapour annealing optimisation and brush layer modification using oxygen plasma”, School of Engineering and Computing, Dublin City University, January 2017
2. Oral Presentation: ‘Block by Block’, Thesis in Three National Final, Sugar Club, Dublin, November 2016
3. Oral Presentation: “Block copolymer solvent vapour annealing optimisation and brush layer modification using oxygen plasma”, Intel Ireland Research Conference, University College Dublin, October 2016.
4. Oral Presentation: “Block by Block”, Inspirefest Researchfest, Bord Gais Energy Theatre, Dublin, July 2016.
5. Oral Presentation: “Block copolymer solvent vapour annealing optimisation and brush layer modification using oxygen plasma”, EUPOC 2016, Lake Garda, Italy, May 2016.
6. Poster presentation: “Block copolymer nanopatterning and selective etching using plasma”, The Intel Ireland Research Conference, Smock Alley Theatre, Dublin, Ireland, October 2015.
7. Poster presentation: “Plasma-based surface nanopatterning of semiconductor materials using block copolymer lithography”, EMRS Spring Symposia, Lille, France, May 2015
8. Poster presentation: “Plasma based surface nanopatterning of semiconductor materials using block copolymer lithography”, The Intel Ireland Research Conference, Science Gallery, Dublin, Ireland, November 2014

Abbreviations

AAO	anodic aluminium oxide
AFM	atomic force microscopy
APCs	adipose-derived stem cells
ATR	attenuated total reflectance
BCP	block copolymer
DSA	direct self-assembly
EUV	extreme UV
FESEM	field emission scanning electron microscopy
FFT	Fast Fourier transform
GFP	green fluorescent protein
GISAXS	grazing incidence small-angle X-ray scattering
HSQ	hydrogen silisequioxane
IC	integrated circuits
IR	Infrared
mT	milliTorr
OES	optical emission spectrometry
PDMS	poly (dimethyl) siloxane
PECVD	plasma enhanced chemical vapour deposition
PEGDA	poly (ethylene glycol) diacrylate
PEO	polyethylene oxide
PPGDA	poly (propylene glycol) diacrylate
PFS	polyferrnocenyldimethysilane
PID	proportional–integral–derivative
PS – *b* – P4VP	polystyrene – *block* – poly4vinylpyridine
PS – *b* – PB	polystyrene – *block* – polybutadiene
PS – *b* – PLA	polystyrene – *block* – polylactide
PS – *b* – PMMA	polystyrene – *block* –polymethyl methacrylate
PSPD	photosensitive photo diode
PTPE	polytetrafluoroethylene
PVC	polyvinyl chloride
R_a	roughness Average
RIE	reactive-ion etch

RMS	root mean square
RTD	resistance temperature detector
s	seconds
SA	self-assembly
SAMs	self-assembling monolayers
SCCMs	standard cubic centimetres per minutes
SEM	scanning electron microscope
Si CMOS	silicon complementary metal oxide semi-conductors
W	watt
WCA	water contact angle

List of Tables

Chapter Three

Chapter Five

Chapter Six

Chapter Seven

List of Figures

Chapter One

Chapter Two

Chapter Three

Chapter Four

Chapter Five

Chapter Six

Chapter Seven

Abstract

Plasma-based surface nanopatterning of semiconductor materials using block copolymer lithography

Shauna Flynn

This project focuses on utilising block copolymers (BCPs) to fabricate silicon nanopillar arrays. The rationale for this was to use these silicon nanopillar substrates as a master to fabricate polymer nanopillars through replica molding techniques for applications in antibacterial surfaces. In the process, we aim to investigate reactive ion etch plasmas to modify polymer brush layers and to selectively remove polymer material from the surface.

The development of a highly-controlled annealing process for polystyrene – *block* – poly4vinylpyridine (PS – *b* – P4VP) using a custom built solvothermal annealing chamber was undertaken. This work eradicated the disadvantages associated with static annealing methods and allowed the fabrication of BCP templates with hexagonal ordering. The removal of P4VP cores using plasma was investigated. In this work, oxygen, argon and nitrogen plasmas were investigated. A key finding was that nitrogen plasmas were successful in removing P4VP over PS, with further etch investigations into P2VP leading to the hypothesis that the nitrogen in the aromatic ring of P4VP plays a vital role in the etch rate. Preliminary results for the modification of a preferential PS brush layer to a neutral brush layer to control BCP orientation have been presented. This work showed that the wettability and surface energy of the brush layer was modified when exposed to an oxygen plasma. BCP annealing on top of plasma modified brush layers provided and insight into how the addition of oxygen effects BCP orientation.

Replica molding methods were optimised using nanostructured cicada wings. This enabled polymer nanopillars surfaces to be fabricated. The swelling properties of these materials were investigated with the results revealing that the polymer swelling caused the nanopillar structure to increase in size. The fabrication of silicon nanopillar arrays using BCP templates of been demonstrated. These templates were transferred into the silicon substrate by converting the BCP into a hard mask and performing a silicon etch. Using optimised molding methods, polymer nanopillar surfaces were fabricated. These polymer surfaces were tested for antibacterial activity. Results showed nanostructured surfaces with pillars greater than ~50nm in height exhibited a greater antibacterial effect when compared to unpatterned surfaces and nanostructured surfaces with pillars less than 50nm.

Chapter One

1 Literature Review

1.1 Moore's Law

Gordon E. Moore, co-founder of Intel, published a paper in 1975 that would define the future of integrated electronics for years to come; at the time, Moore was the Vice President of Research and Development at Fairchild Semiconductor. In this article, numerous perceptive predictions including 'personal portable communications equipment', automated controls from automobiles and home computers, were discussed. The most important of these predictions was his estimate of how the future of integrated circuits would exponentially grow, see Figure 1.1.[1, 2] It was stated that the number of transistors on an integrated circuit would double every year. He projected this growth for the decade to come and in 1975 he revised his theory predicting the growth to continue every two years. [3]

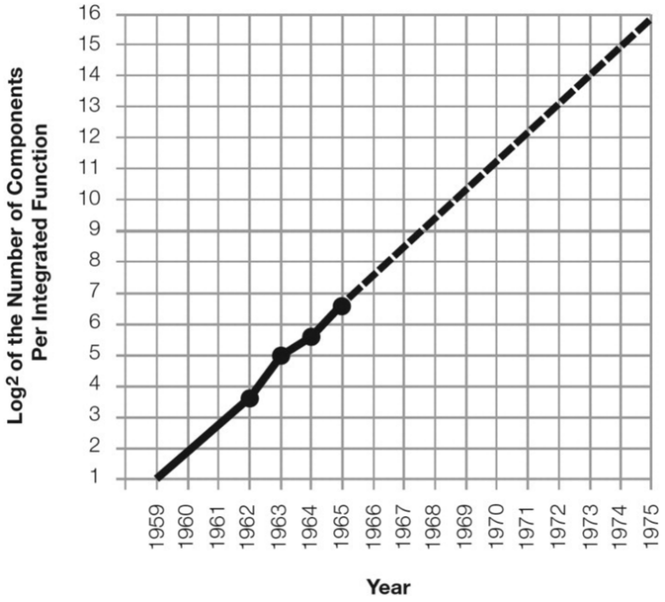

***Figure 1.1** The original chart that was presented in Moore's publication, showing the predicted density of components in integrated circuits.* [1]

At the time of publication, Moore only had three historical product data points which he could use to aid his prediction, in addition to the knowledge he had from working on a fourth prototype in Fairchild, making his observation even more noteworthy. It wasn't until several years later when Professor Mead in California Institute of Technology coined the projections, 'Moore's Law'. For over a half a century, Moore's

Law has continued unabated and is the founding principle of the semiconductor industry. [1-3] The major advances in lithography to date have led to the miniaturisation of components down to 14nm pitch. With the capability to produce such feature sizes and the volume of production available, silicon complementary metal oxide semiconductors (Si CMOS) technologies are the leading field of nanotechnology and will continue to be in the years to come.[3] However, CMOS development is now reaching numerous limitations that are hindering the continuation of Moore's Law, the first of which is the transistor scaling limits. As the density of transistors increases, the dimensions must decrease. Nevertheless, scaling down is leading to practical limits with current leakage at small gate lengths. Leakage refers to the leak of current from a charged transistor even when the device is in the off state. The problem at small gate lengths is that the drain voltage reduces the barrier height at the source, thereby causing a low source-to-channel barrier height even with the gate voltage off, which results in detrimental large off-state leakage. In the current gold standards in high-performance logic systems, the net leakage power of CMOS transistors is approximately 20-30% of the total power budget. It is apparent that this current leakage is already at the practical limit. To prevent further increases in leakage, gate length reduction has slowed in the last decade. [3]

The limits of photolithography are another barrier that needs to be conquered. Intel has developed 14nm features using excimer lasers, although the diffractive index of UV light makes scaling down from this point impossible using the current optical techniques. The move to extreme UV (EUV) light photolithography, electron beam or x-ray lithography to create sub 10nm features is now a possibility. This move to shorter wavelengths such as EUV brings other technical challenges such as source power output and the considerable cost, reported to be over €70 million per tool.[4, 5] Other techniques must be explored if Moore's law is to continue into the future.

1.2 Block Copolymers for Nanofabrication

As dimension size continues to scale down and with the limitations involved with current methods aforementioned, new technologies must be investigated. Extreme ultra-violet lithography, nanoimprint lithography, interference lithography and direct self-assembly (DSA) of block copolymers (BCPs) are among the methods considered as a potential solution for fabrication of sub-14 nm nodes. Top-down methods of fabrication have several limitations to their practical efficacy as previously mentioned; therefore, moving towards the bottom-up approach of BCP DSA has numerous advantages. The tune-ability of the size, shape and composition of the polymer materials makes them a cost-efficient method for nanotechnologies. These materials can form morphologies that are applicable for semiconductor applications by self-assembly. Moreover, the method of forming these features can be easily implemented into industry as many of the techniques are already utilised.[6] Self-assembly (SA) is a reversible process where the disordered components of the block copolymer for a highly ordered pattern under certain conditions. There are two routes in which this can happen, under static SA or dynamic SA. The former involves a system that doesn't dissipate energy and are at local equilibrium. The later may require energy for an ordered structure to form. This reversible spontaneous process of SA can be summarised from the Gibbs Free Energy equation (1.1) stated below.

$$\Delta G_{SA} = \Delta H_{SA} - T\Delta S_{SA} \tag{1.1}$$

When ΔG_{SA} is negative, SA is a spontaneous process. ΔH_{SA} enthalpy change is due to the interaction between BCP components and $T\Delta S_{SA}$ entropy change is due to a change in the process. From equation 1.1 it can be concluded that for a given system above a certain temperature for SA to occur, the enthalpy term must be negative and in excess of the entropy term. Thus, for SA to successfully occur, enthalpic forces must dominate.

1.3 Microphase separation

A BCP is two or more polymer materials connected by a covalent bond that are significantly chemically different, see Figure 1.2 The thermodynamic incompatibility between the polymers drives them to microphase separate into well-ordered periodic nanostructures. [7-9] This chemical dissimilarity and the molecular weight of the BCP defines the minimum feature size obtainable and the order periodicity.

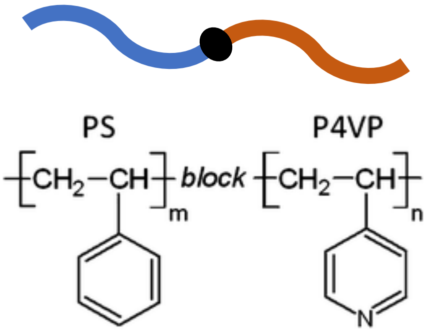

Figure 1.2 *Molecular structure of* polystyrene – *block* – poly4vinylpyridine *(PS – b – P4VP) BCP system with cartoon representation displayed above the molecule.*

The simplest BCP system is a diblock copolymer, which are two molecular units arranged in distinct segments. These segments can be represented as $A_n – B_m$ where A and B are the polymer units and *n* and *m* represent the number of repeating units within the polymer.[10, 11] The BCP microphase separation is a result of the system minimising repulsive high energy interactions between similar and dissimilar blocks and maximising attractive, low energy, interactions between similar blocks. The BCP system will attempt to minimise the interfacial surface area between dissimilar blocks. The covalent bond between blocks allows for the separation to only occur on the microscale, in other words, the feature size is controlled by the polymer chain size. [8] In a diblock copolymer, this microphase separation is controlled by three experimental parameters:

1. The degree of polymerisation *(N)* i.e. the number of repeated polymer units.
2. The BCPs or molar fraction *(f)* i.e. the ratio of block A to block B.
3. The A – B Flory-Huggins interaction parameter (χ) i.e. the measure of immiscibility of block A and block B.

The block volume fractions (f_A and f_B, where $f_A + f_B = 1$) and the polymer-polymer interaction parameter (referred to as χ) contribute to resulting morphology and the self-assembly dynamics of materials.[12, 13] The χ parameter itself represents the degree of incompatibility between blocks and it is this factor, which is the main driving force for microphase separation.[13] Diblock copolymers form geometries which can be finely tuned by controlling the degree of polymerisation ($N = N_A + N_B$). The Flory–Huggins equation (1.2) describes approximately how these parameters affect the free energy of a blend.

$$\frac{\Delta G_{mix}}{k_b T} = \frac{1}{N_A}\ln(f_a) + \frac{1}{N_B}\ln(f_b) + f_A f_B \chi \qquad (1.2)$$

ΔG_{mix} = Gibbs free energy
K_b = Boltzmann’s constant
T = Temperature
N_A = Polymerisation of block A
N_B = Polymerisation of block B
f_A = Volume fraction of block A
f_B = Volume fraction of block B
χ = Flory-Huggins Interaction Parameter

From the equation, terms 1 and 2 can be manipulated by the polymerisation of the BCP and relative volume fractions. In contrast term 3, χ, is a result of the molecules involved (f_A and f_B) and is directly related to temperature. [14]

The use of BCPs for lithographic applications was first explored by Mansky et al. using a sphere forming polystyrene – *block* – polybutadiene (PS – *b* – PB) system. [15, 16] The ability to self-assemble into ordered arrays of lines and spots was the most appealing feature of BCPs, as this was usually done by difficult and expensive lithographic processes. The etch contrast between PS and PB also made the system an excellent template for pattern transfer, the results were dense arrays of periodic hexagonal spot patterns, see Figure 1.3

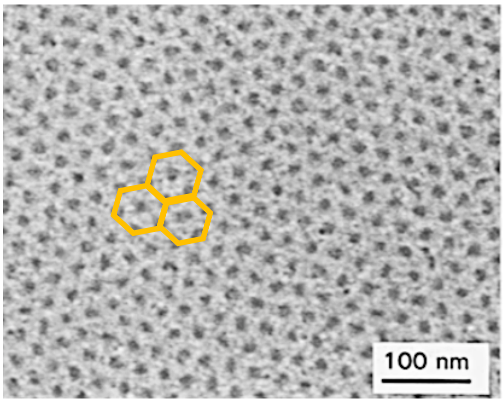

Figure 1.3 *PS – b – PB spot pattern first fabricated by Mansky et al., hexagonal ordering is marked with the yellow hexagons.*[15]

1.4 Diblock Copolymers

There are numerous symmetries in which blocks can be ordered. The classic morphologies include lamellae, hexagonal arrays of cylinders, spheres with body centered cubic symmetry and finally gyroids structures. [8] Figure 1.4. a) depicts the phase diagram of a diblock copolymer with volume fraction vs χ.N as predicted by self-consistent field theory and b) depicts these morphologies with the diblock molecules represented as simplified two-colour chains. The phase diagram shows the relationship of χ.N versus f. If χ and/or N value are reduced so that χ.N is below a critical value, entropic factors will produce a disordered phase. It should be noted that the product of χ and N, χ.N, plays a pivotal role in microphase separation occurring and theoretically a χ.N value above ~ 10.5 is needed for ordered morphologies to occur.

χ is determined by the BCP selected, while the volume fraction and polymerisation which influence the translational and configurational entropy are determined by the polymerisation stoichiometry. As determined from equation 1.2, χ is a temperature dependent parameter. For an ordered structure at equilibrium, polymer chains of the BCP will be arranged in minimum free energy configurations.

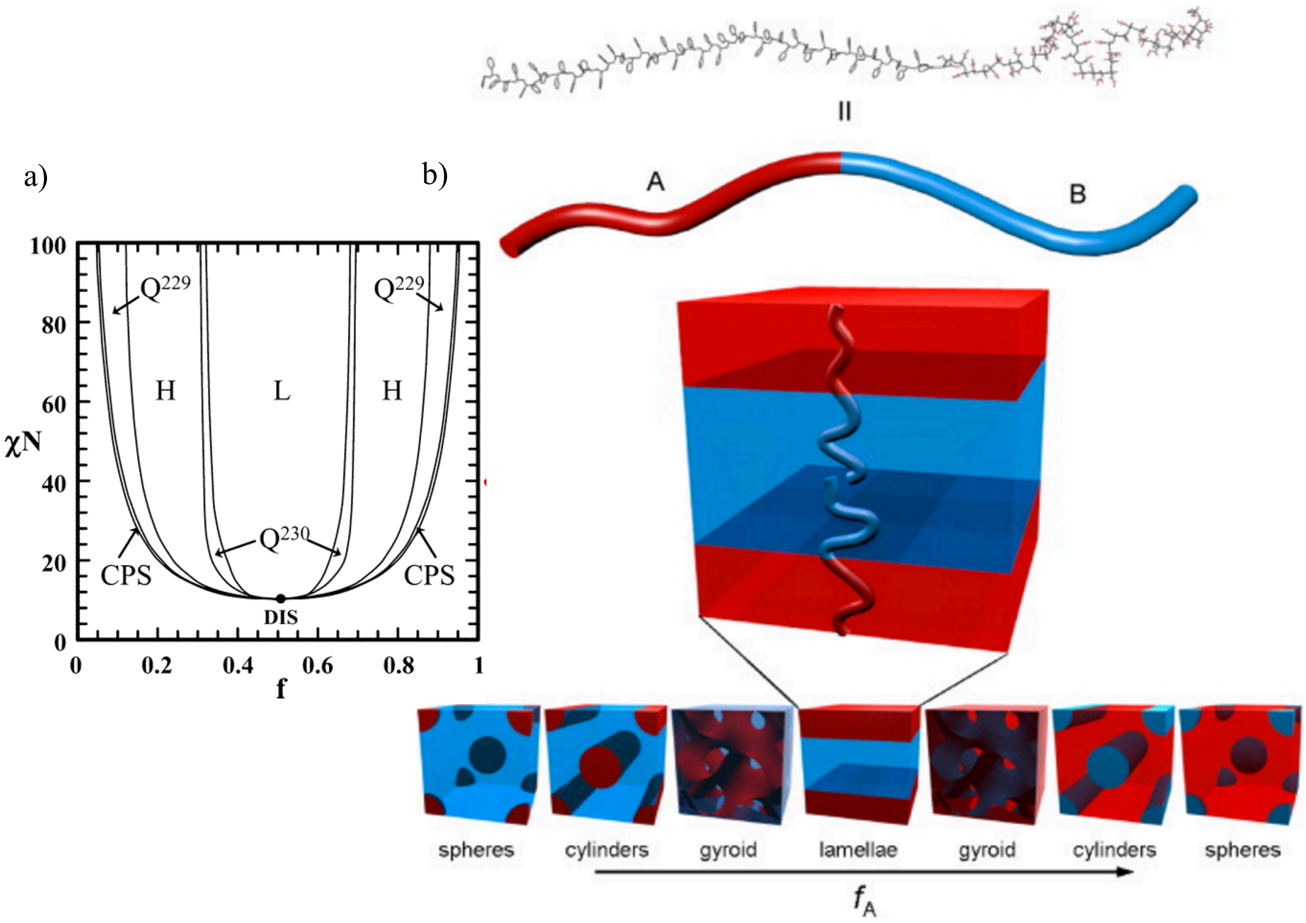

Figure 1.4 *a) Phase diagram of a diblock copolymer with volume fraction vs χ.N as predicted by self-consistent field theory. b) Schematics of thermodynamically stable diblock copolymer phases. The chains self-organize such that contact between the immiscible blocks is minimised, with the structure determined primarily by the relative lengths of the two polymer blocks (f_A).*[17]

In this thesis, the focus will be largely on the simplest form and the most studied, A – B diblocks. The reason for this being that diblock copolymers produce morphologies that can be used in semiconductor applications. It must be noted that several transition phases are observed experimentally but are not thermodynamically stable.[17] For the semiconductor industry and for this study, the two structures of greatest importance are 1) lamellae structure, which form BCPs arranged in lines, and 2) hexagonally packed cylinders within a matrix of the second block, see Figure 1.5.

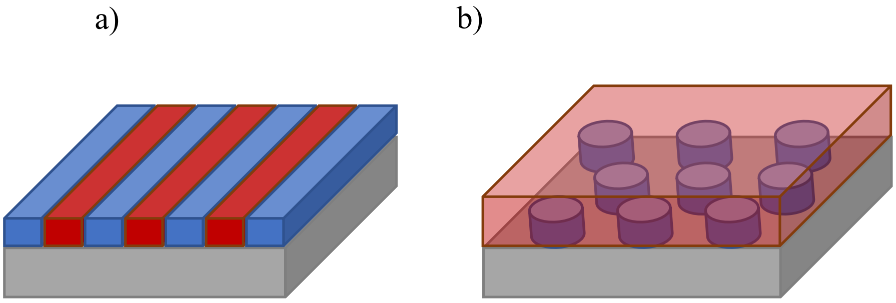

Figure 1.5 *a) Lamellae aligned perpendicular to the substrate. b) Cylinders aligned perpendicular to the substrate.*

1.5 Orientation

Controlling orientation, lateral ordering and placement of BCPs is essential for nanolithographic applications. Perpendicular orientation of lamellae and cylinders, see in Figure 1.5, are often most desirable. For symmetric A – B systems, there is preferential interaction between blocks and the surface, due to the difference in interfacial energies between blocks. [18] Usually, one block will have a lower surface energy and will be more likely to interact with the interface compared to the second block. With one block having an affinity for one interface, the orientation results in parallel lamellae sheets or cylinders, wetting layers and hole-island structures. [6] In order to change the orientation from parallel to perpendicular, these preferential interactions must be overcome and the surface energy at the interface must be controlled. The following are a number of strategies developed to control BCP orientation.

1.5.1 Surface Energetics and Film Thickness

In theory, a BCP system in contact with two neutral interfaces will be able to self-assemble into perpendicular morphologies no matter the thickness of the film. Once the preference of surface interactions is minimal, the orientation of perpendicular structures is controlled by surface interactions and film thickness. Substrates can be neutralised to provide non-preferential surface interactions by manipulating the chemistry of the surface, which will be discussed at a later stage. However, the air-film interface is more difficult to control. The air is usually replaced with solvent or vacuum. On account of this, BCP systems with near equal surface tensions are of most interest, such as polystyrene – *block* –poly (methyl methacrylate) (PS – *b* – PMMA), the most widely researched BCP system.[18]

1.5.2 Brush Layers

A brush layer is a thin layer (usually less than 6nm) of polymer material used to change the surface chemistry of the substrate. They are considered to be the simplest and most appropriate form of surface modification to enable complete control of BCP orientation. There are a variety of brushes that can be used such as self-assembled monolayers (SAMs), [19] end-grafted homopolymers,[20] end-grafted random copolymers [21] and cross-linked polymer mats.[22] Homopolymers and random copolymers are end-grafted with hydroxyl groups to allow irreversible covalently binding between the brush and the silicon substrate, see Figure 1.6. The most common form of surface modification is the use of random copolymer brushes.

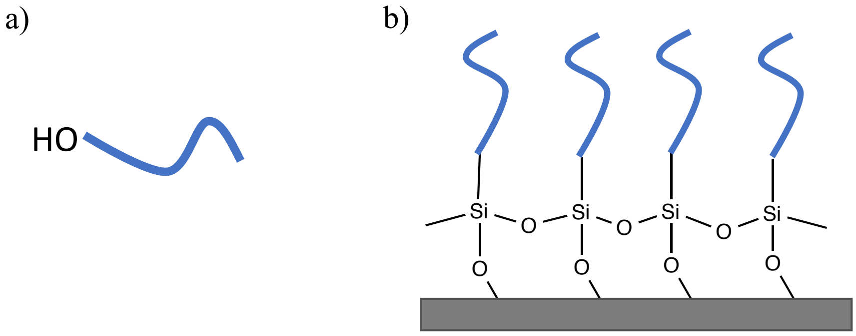

***Figure 1.6** a) Brush layer end-terminated with a hydroxyl group to allow covalent attachment to the silicon substrate. b) A brush layer attached to a silicon substrate.*

During annealing when BCPs enter the phase above the glass transition temperature T_{g}, the morphology of the BCP is controlled by the preferential interactions at the surface. T_{g} is the temperature where the polymer changes from a hard, glassy material to a soft, rubbery material. The preferential interaction for one block to interact with the surface and the other block to interact with the air interface, leads to parallel orientation in cylinder and lamellae systems. To obtain perpendicular orientation the surface must be neutralised to interact both blocks, see Figure 1.7.[6]

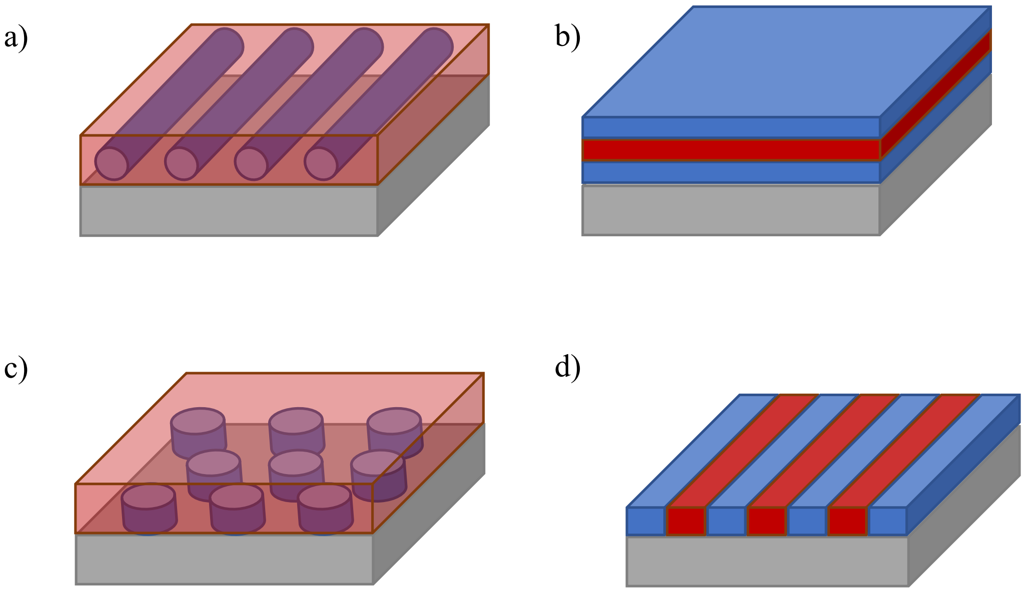

Figure 1.7 *a) Parallel aligned cylinders, b) Parallel aligned lamellae. Preferential wetting brush layers will result in these BCP morphologies. c) Perpendicular aligned cylinders, d) Perpendicular aligned lamellae. Neutral wetting brush layers will result in these BCP morphologies.*

PS – *b* – PMMA is a classic example of the phenomenon. PMMA cylinders have a preferential interaction with oxide layers on a silicon substrate, resulting in parallel orientation of the domains. To control the preferential interaction, the most popular method of modifying or neutralising the substrate is by using hydroxyl-terminated random copolymers, such as PS – *r* – PMMA.[18] Mansky et al. were one of the first to report on this phenomenon. Their work describes precise control of PS – *b* – PMMA orientation which can be regulated by controlling the interfacial energy of the substrate. This was achieved by anchoring a thin film of the random copolymer PS –

r – PMMA.[23] This random copolymer brush layer provides a neutral interface for both blocks to interact equally, leading to perpendicular orientation of the microdomains.[23, 24] This modification of substrates has been widely reported on for the past 20 years. Mansky et al., again, was one of the first to investigate random copolymers as a way to manipulate the surface chemistry. Their work showed that by varying the styrene content of the brush layer, the wetting behaviour at the surface, where the brush was attached, could be controlled.[23]

Ji, Bates and Ryu have done similar work using different variations of random copolymers with different BCP systems in order to control wetting behaviours at the interface.[25-27] Another strategy that has been explored is the use of SAMs. Peters et al. used SAMs that were chemically modified by X-rays to control the wetting behaviour of PS – b - PMMA BCPs.[28]

1.6 Alignment

The importance of BCP orientation has been discussed above, however, efficiently aligning BCPs to get patterns of straight lines and hexagonal array is also of great importance when considering BCP for semiconductor applications. Before alignment, lamellae systems form ‘fingerprint’ like patterns, see Figure 1.8. These ‘fingerprint’ patterns formed by perpendicular orientated lamellae have very limited application towards fabrication of interconnects and vias in integrated circuitry in their natural form. However, if these films can be directed to align in any direction to generate long-range ordered patterns, the applications in integrated circuit (IC) manufacturing are substantial.[6]

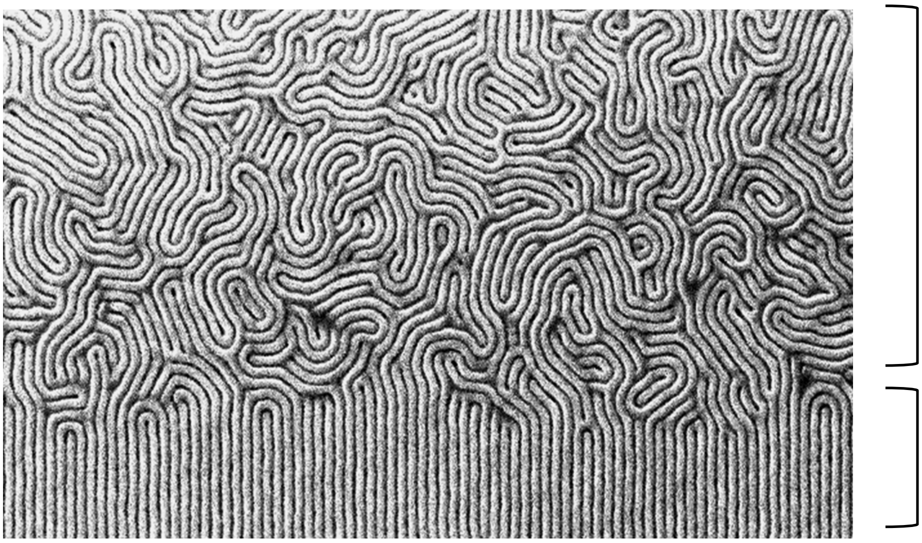

a) Unaligned BCP pattern on chemically neutral surface

b) Aligned BCP pattern controlled by a chemical wetting stripe

Figure 1.8 *SEM images of lamellae-forming PS – b – PMMA film that is a) self-assembled on chemically neutral substrates and b) directed to assemble on striped chemical patterns.* [19]

Methods to direct a BCP pattern to obtain long-range ordered arrays include solvent flow, shear force and zone annealing, have been investigated and can described collectively as directed self-assembly (DSA). Two methods of DSA that are of most interest as they are easily carried out and can be potentially integrated into IC manufacturing are grapheoepitaxy and chemical epitaxy (chemoepitaxy).

Graphoepitaxy uses topographic features to align BCPs, where chemoepitaxy uses chemical modification of the surface to direct BCP alignment. These DSA techniques combine the advantages of traditional lithography to spontaneously form sub 10nm nanostructure with limited defects.

1.6.1 Graphoepitaxy

Graphoepitaxy, or physical epitaxy, uses topographic features on the substrate to induce orientation and for controlling lateral ordering of microdomains.[24] It is still a chemically facilitated form of DSA as it relies on the preference of one block to selectively wet the edge of a topographic feature. This form of BCP alignment is particularly useful due to the ease at which topographic features can be induced on a surface with standard photolithography methods. Typically, the pattern size for the grapheoepitaxy ranges from 2-3 times the lattice spacing in the BCPs to a few microns.[8]

The major disadvantage to this method is large surface coverage is lost due to the macro-scale topographic features needed for the grapheoepitaxy, however, long range lateral ordering can be easily achieved using typical processing conditions which are essential for the semiconductor industry. Cheng et al. have shown the alignment of a sphere forming polystyrene – *block* – polyferrnocenyldimethysilane (PFS) in pre-patterned templates. In this work, they investigated the formation of defects by changing the width of the patterned trenches, highly-ordered arrays were obtainable in both constant-width and varying-width templates.[29]

Borah et al. have demonstrated large surface area coverage of perpendicular orientation PS – *b* – PMMA aligned using topographic lines created by electron-beam patterning of hydrogen silisequioxane (HSQ), a typical e-beam resist material, see Figure 1.9. [30]

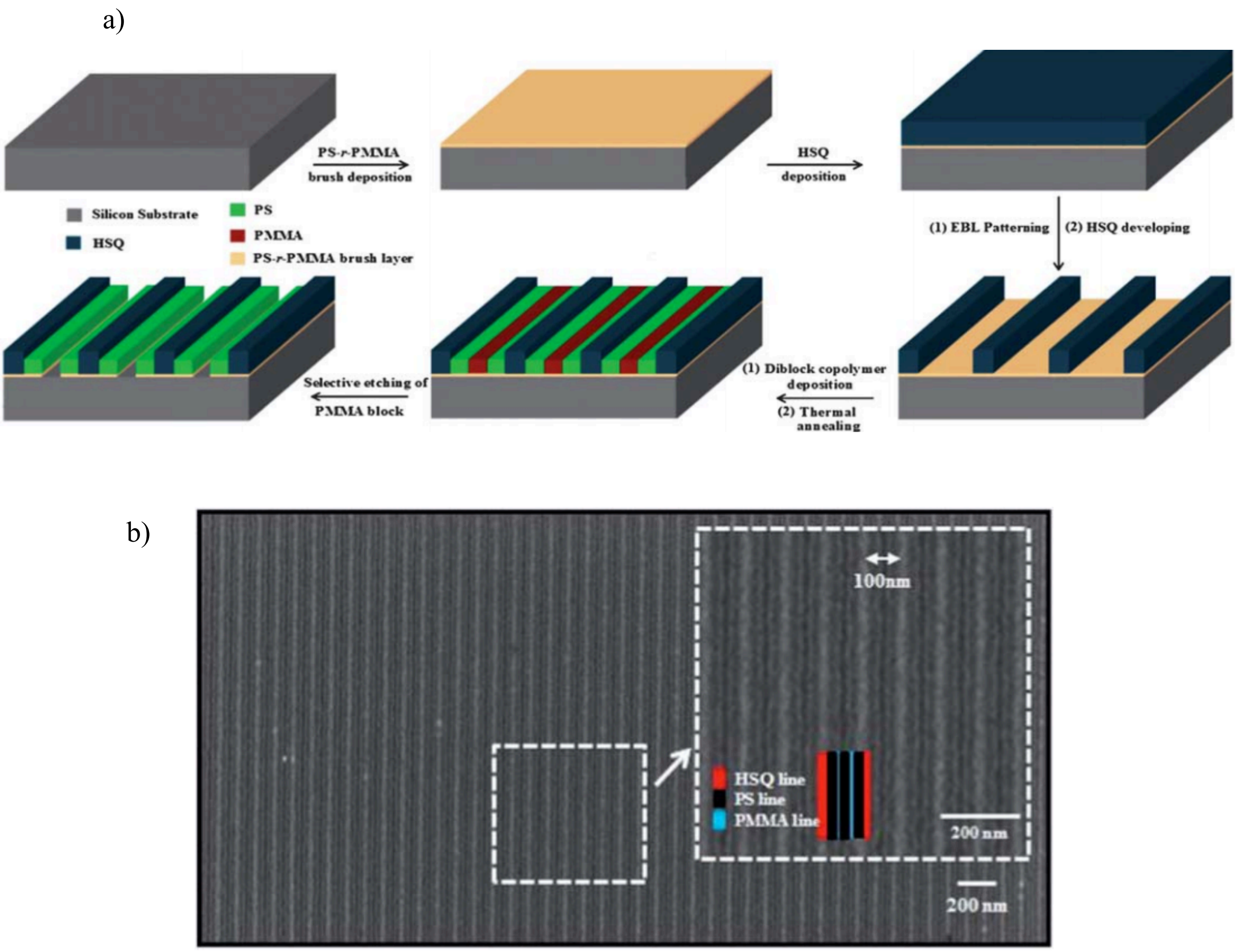

Figure 1.9 *a) Schematic of the process flow depicting HSQ pattern writing by EBL process on silicon substrate pre-coated with PS – r – PMMA brush, PS – b – PMMA BCP deposition and self-assembly, and plasma etching to selectively remove PMMA block b) Top-down SEM image of large area alignment of PS – b – PMMA BCP patterns on narrow HSQ gratings (light grey lines: PS and dark grey lines: removed PMMA). Insets show the organisation of HSQ, PS and PMMA blocks.*[30]

Similarly, Xiao et al. have showed the ability to fabricate patterned magnetic dot arrays using BCP lithography. In their work, they obtained long-range ordering of cylindrical domains orientated perpendicular to the substrate with hexagonal ordering. They achieved this by pre-patterning the substrate with a trench feature and chemically modifying the surface to induce a neutral brush layer. The metal dot arrays were then fabricated by sputtering the metal on a PS porous BCP matrix and removing the PS using both wet and dry etch techniques, see Figure 1.10. [31]

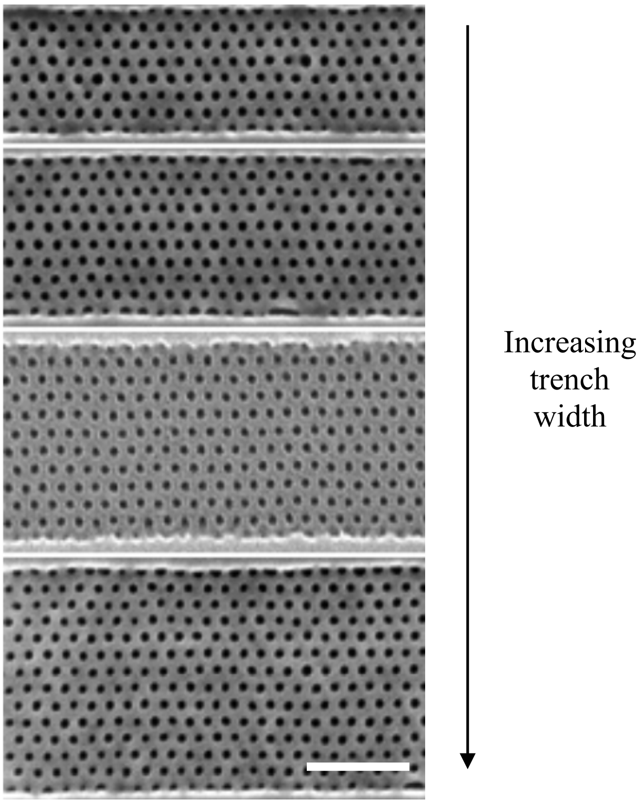

Figure 1.10 *PS –b– PMMA thin films that have been annealed on topographic trench patterns. The width of the trench feature was modified to study BCP alignment. Scale bar is 250nm.*[31]

1.6.2 Chemoepitaxy

Using chemically patterned surfaces is another method that has been widely investigated to control lateral ordering of BCP microdomains. The theory behind this method is that BCPs can conform to surface patterns when a strong surface interaction between the blocks and substrate is present.[32] The process consists of a primary step of chemical patterning on the substrate using extreme ultraviolet, interferometric lithography, or e-beam lithography, followed by a secondary step of spin-coating lamellae forming BCPs onto the chemically patterned substrate. The physical properties of the chemical pattern applied to the surface, such as width of the wetting stripe and of course, the interfacial energies between blocks, play a vital role in directing the BCP films. [33] The period of the pattern L_s, and the width of the wetting stripe W are optimised to be $L_s \approx L_0$ and $W = ½ L_0$, respectively, where L_0 is the domain period of the perpendicular lamellae structure in a thin film on top of a uniform surface. [34]

Edwards et al. have demonstrated that the broader the difference in interfacial interactions, the stronger the directing ability. Moreover, they have shown, using the optimal values of $L_s = L_0$ and $W = ½ L_0$, the chemically patterned substrates generate defect-free lamella-forming BCP patterns. [21] However, a slight deviation of the two sizes from the optimal values significantly reduces the ability to guide the pattern and the resulting morphologies have a high percentage of defects as further demonstrated by Kim et al. and seen in Figure 1.11. [19] For Figure 1.11 a) where L_s = 55nm and $L_s > L_0$ disordered features was observed. For b) where L_s = 47.5nm and $L_s \approx L_0$ perfect ordering was achieved.

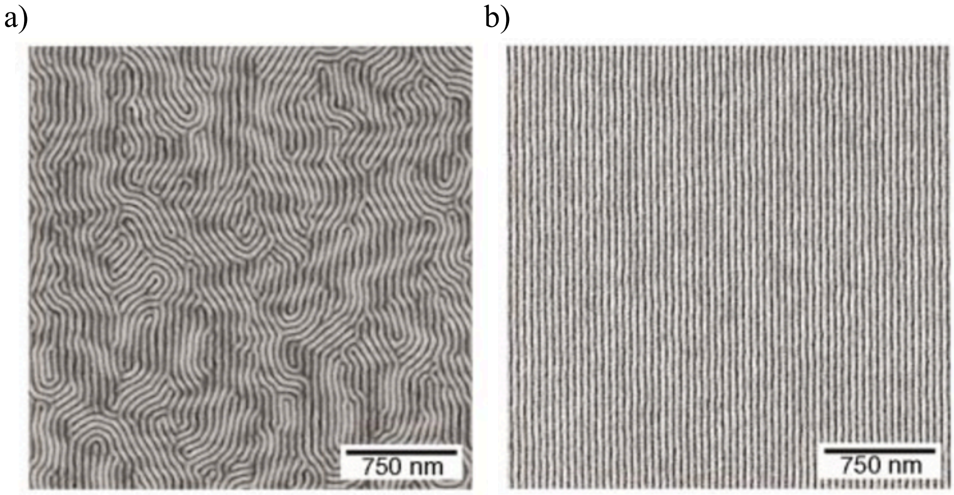

Figure 1.11 *Top down SEM images and corresponding Fourier transform analysis of PS – b – PMMA on chemically patterned surfaces.*[19]

The study carried out by Edwards and co-workers directly proves that a larger contrast in interfacial energy enhances the ability of the chemical pattern to direct a BCP. This increases the window of permissible deviations between periodicity, L_s, of the chemical pattern and the BCP domain period, L_0, without losing the ability of defect-free pattern formation. [21, 33]

1.7 Annealing methods

The most common annealing techniques for inducing microphase separation are thermal annealing and solvent annealing. Both processes are described below. Other forms of annealing have been investigated, these include, solvent injection annealing, sub -100°C annealing and rapid thermal annealing to mention a few. [35-37] Solvent and thermal annealing are the most relevant methods of annealing for the BCP system which are used herein and are of most importance for industry; therefore, other methods will not be discussed in this thesis.

1.7.1 Thermal Annealing

Thermal annealing is a process by which the BCPs are heated above the glass transition stage T_g, allowing for microphase separation. Above T_g the diffusivity, D (T) of a polymer chain is inversely proportional to time (t), as described by the Arrhenius equation (1.3), where ΔE_α is the activation energy of the polymer, A is a constant, T is temperature and R is the ideal gas constant.

$$\frac{1}{t} \sim D(T) = A \exp(-\Delta E_\alpha / RT) \tag{1.3}$$

Increasing the annealing temperature will induce a faster annealing time, by increasing assembly kinetics to obtain the equilibrium ordered structure. [18] The process is usually performed in ambient conditions or under vacuum. Thermal annealing is usually a slow process that can exceed 48 hr; however, rapid heating methods have been investigated.[38] Perpendicular orientation of BCP domains is most desired for semiconductor applications, as mentioned previously. In order to achieve this the surface energy (γ) of both blocks must be almost equal under annealing conditions. When the difference in γ values ($\Delta\gamma$) is great enough, a wetting layer will form at the free surface. Both γ and $\Delta\gamma$ are temperature dependant in most BCP systems. Mansky et. al. determined the γ values for PS – *b* – PMMA and found that the difference in surface energies was less that 1% at 170°C, making PS – *b* – PMMA an excellent system for use in DSA. [23]

1.7.2 Solvent Annealing

Solvent annealing is another common method to induce self-assembly of BCPs. Similar to thermal annealing, in which BCP films are heated above the glass transition stage T_g. This method of annealing films uses solvent vapour, originating from a saturated solvent atmosphere to partially solubilise and therefore, plasticise the BCP film. By doing this, the mobility of the system is increased. [39] It is important to consider that the solvent can only escape the film at the surface, leading to a highly directional process. This also leads to the concentration of the solvent throughout the film being uneven. The concentration being lowest at the surface and highest within the film. As evaporation occurs, this gradient propagates until the solvents has evaporated fully from the film. This presence of solvent within the film performs several key functions:

1. The solvent mediates surface energies and hence tends to orient microdomains neutral to the surface, provided there are no preferential interactions of the solvent with one of the blocks.
2. During solvent annealing, the gradient in the solvent concentration corresponds to a gradient in the ordering of the BCP, with microphase separation occurring initially at the film surface first. As the solvent evaporates, subsequent microphase separation of the BCP is templated by the ordered structure at the surface of the film.
3. The presence of the solvent enables significant mobility of the BCP, reducing the glass transition temperature T_g, leading the grains of the microdomains to coarsen.

Therefore, during the solvent evaporation, multiple key processes are occurring which will ultimately decide BCP orientation depending on the balance of the kinetics associated with each parameter. [40] The solvent chosen for annealing will usually have no preference for one block over another. Moreover, the solvent should induce annealing at a range of temperatures as well as the ambient. In a solvent-saturated atmosphere, the BCP films become highly swollen and are driven into a disordered phase. It is during the evaporation of the solvent from the surface of the film when the morphologies reach an ordered phase, and this ordering spreads from the surface down. [24]

Solvent annealing is conventionally carried out by placing the spin-coated BCP thin film and a reservoir of solvent, together in a glass container for a period of time. The solvent vapour will build up in the jar and eventually reach saturated vapour pressure. After the annealing process has taken place, the sample is removed and allowed to air dry.[41] There are many limitations involved with this solvent annealing set-up, the major disadvantage being lack of control over the annealing process. Solvent and sample temperature cannot be finely controlled. Solvent vapour pressure and the final removal of solvent from the BCP can also not be controlled. Furthermore, if BCP are to be integrated into industry, a more controllable and reliable process will be needed. To overcome these downfalls a number of annealing chambers that incorporate a continuous gas flow have been set-up.[42] These solvent annealing chambers provide a completely controllable process. The solvent is normally carried into the chamber using an inert gas, and the system can be easily purged following annealing. Optical reflectometry and ellipsometry have been incorporated to observe film swelling during the annealing phase. Resulting films are highly ordered with limited defects, see Figure 1.12.

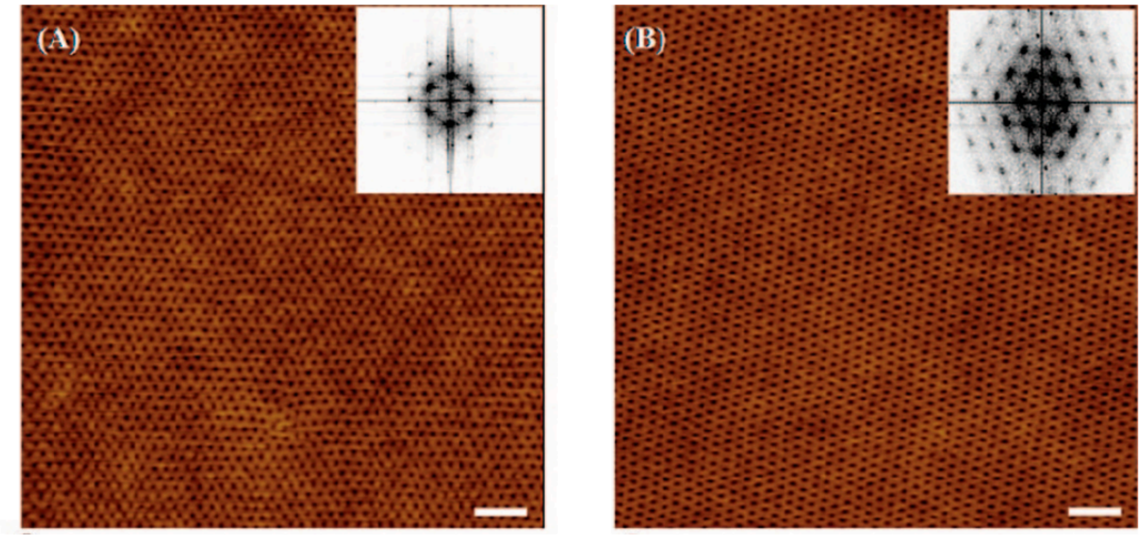

***Figure 1.12** Height mode AFM images of highly ordered polystyrene – block – poly4vinylpyridine (PS – b – P4VP) films to silicon. a) Solvent annealed films. b) Surface reconstruction of the ordered films. The impressive degree of order is reflected in the Fourier transform, as shown in the inset. Scale bar is 200 nm.*[40]

1.7.2.1 Solvent annealing mechanism

During solvent annealing, the BCP film undergoes two stages. A swelling stage whereby the film is swollen with the solvent and the drying phase whereby the solvent is removed from the film. It is unclear if the microdomains form in the swollen state or during the drying process. Paik et al. have proposed a mechanism for the self-assembly of a cylinder-forming poly (α-methylstyrene – *b* – 4-hydroxystyrene) (PαMS-*b*-PHOST) film in tetrahydrofuran (THF) and acetone solvent vapours by grazing incidence small-angle X-ray scattering (GISAXS). Here they report quasi-equilibrium and quenching mechanism.

When a BCP film is swollen during solvent annealing the chain mobility increases with the swelling ratio. When the chain mobility is at its optimal, microdomains assemble and begin to equilibrate in films. Therefore, the morphology of the swollen film depends on the solvent and the swelling ratio, and is not dependant on time. Once the films are rapidly dried, morphologies can be maintained throughout the film. [40]

1.8 Defects

For the potential use as lithographic tools in the semiconductor industry, the processing of BCPs to form well-ordered films with limited defects is essential. To achieve this, there are a number of processing parameters that must be taken into consideration. Firstly, BCP films must have uniform thickness and be relatively thin (sub 50nm). Thick films are of limited use as once one of the blocks is removed to leave behind a matrix of the final block, the remaining structures lack robustness and results in deformed structures due to relaxation. Secondly, another crucial parameter to control is the microphase separation of the BCP as aforementioned. To use such films as etch masks and lithographic tools, films must transition from the disordered state to an ordered arrangement. The equilibrium between the two states must be reached. And lastly, defects from impurities must be taken into consideration. Large surface area of perfectly aligned morphologies are critical if integration into the IC manufacturing industry is possible, as Morris et al. has discussed in a recent review paper.[6]

These defects in BCP patterns are the limiting factor delaying the incorporation of BCP into IC manufacturing. The target is to achieve a process with less than 0.01 defect per cm^2 i.e. roughly ten defects per layer. Recent advances at IMEC have shown reduced defects in BCP systems resulting in defect densities of 100 per cm^2; this however, it still a huge leap from the stated process target. Moreover, how these defects can be identified, characterised and quantified remains a challenge. Repeated SEM imaging across the wafer seems to be the best method and what is used in industry at present.[40] Thus, image analysis software and other effective methods of detecting defects must be developed. It must be also noted, as feature size decreases, high-resolution images of samples will become increasingly difficult to obtain by conventional imaging techniques.

1.9 Patterns to Masks

As new patterning techniques begin to emerge, the ease of integrating these new methods into the nanofabrication industry is essential to consider. This is one of the strongest advantages of BCP self- assembly; as the tools needed to prepare such templates are already implemented in manufacturing lines. Although BCP are valuable for creating a nanopattern, they are of limited use for IC fabrication in their original state due to the lack of etch contrast. The blocks must be converted into on-chip masks that will allow the features generated by the BCP to be transferred into the semiconductor material. Enhanced etch resistance of one block can be achieved through the inclusion of an inorganic heteroatom into one of the blocks. Atomic layer deposition (ALD) and sequential infiltration synthesis have also been investigated where BCP films can be used as whole or one of the block is removed prior to hard mask incorporation.[40, 43]

Darling and co-workers have dominated this niche of enhanced etch contrast using selective infiltration of alumina into PS – *b* – PMMA systems. In the process, the PMMA block is selectively infiltrated with alumina creating an inorganic nanostructure that is the same morphology of the BCP template pattern.

This infiltrated film then becomes resistant to a large variety of plasmas making it a very effective hard mask, see Figure 1.13. [40]

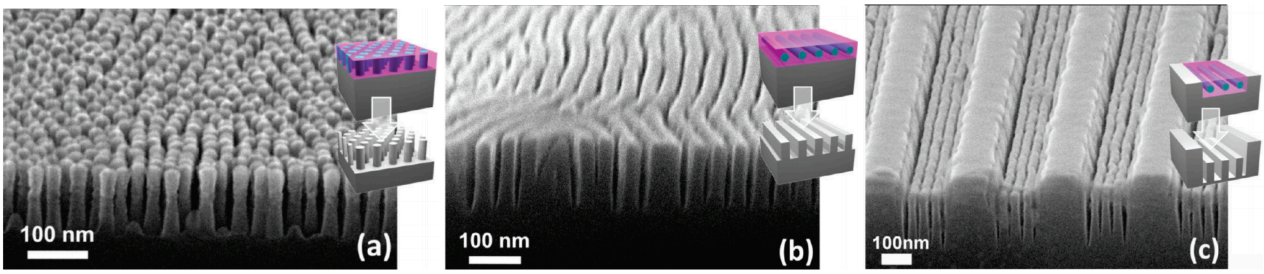

Figure 1.13 *Pattern transfer into silicon using HBr based plasma, with the SIS-enhanced PS-b-PMMA film as etch mask. (a) From perpendicular orientated PMMA cylinders. (b) From in-plane PMMA cylinders. (c) From in-plane PMMA cylinders aligned using grapheoepitaxy.*[17]

Selectively removing one block and proceeding with an evaporation or sputtering of hard mask material is another common method.[44, 45] Tu et al. have demonstrated the fabrication of cobalt nanostructures using polystyrene-block-polydimethylsiloxane (PS – *b* – PDMS) as a template. In this process, one block is removed from a microphased BCP thin film by plasma. The remaining patterning is sequentially back filled with cobalt. Another plasma process and the removal of the remaining polymer material results in cobalt nanostructures, see Figure 1.14.[44]

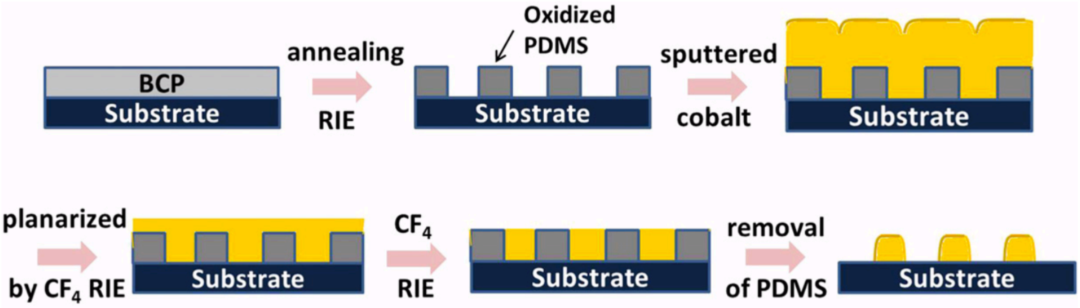

Figure 1.14 *Schematic of pattern transfer process from BCP templates to cobalt nanostructures.*[44]

A metal salt inclusion process enables conversion of an ‘activated’ BCP film to a nanoscale patterned hardmask. In this method, the BCP template is activated with a solvent followed by spin coating of a hard mask material.[46, 47] More recent work using systems containing a polyethylene oxide (PEO) block show how the physical properties of the polymer can be exploited. Goshal et al. and Schulze et al. have both demonstrated the selective inclusion of metal cations into the PEO domain. This can then be oxidised *in situ* to create a hard mask for pattern transfer, see Figure 1.15 and Figure 1.16. [48, 49]

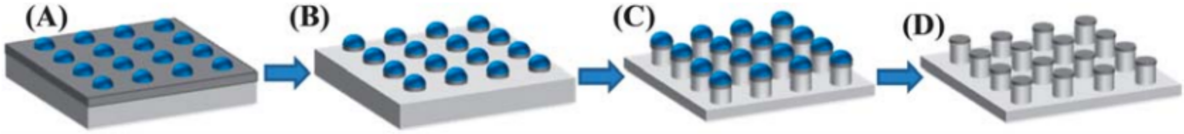

Figure 1.15 *Schematic diagram of the fabrication of Si nanopillar arrays: (A) hexagonally ordered iron oxide nanodots on the Si substrate with a native oxide layer, (B) nanodots after the SiO2 etch, (C) nanopillars formed after the Si etch and (D) Si nanopillars with a native oxide at the top after removal of iron oxide.*[49]

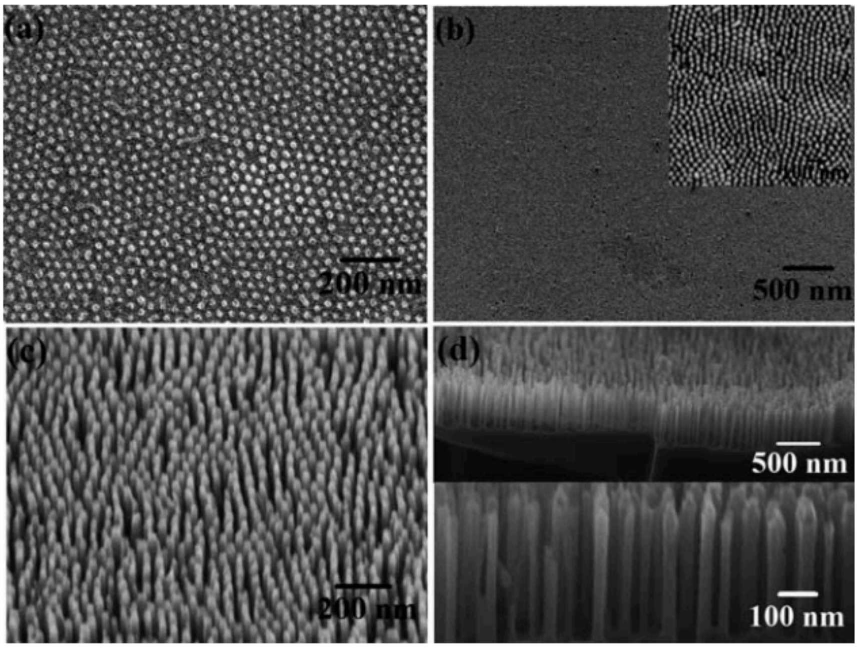

Figure 1.16 *Scanning electron microscope (SEM) images of (a) hexagonally ordered iron oxide nanodots on the Si substrate, (b) nanopillar arrays with iron oxide nanodots at the top formed after pattern transfer onto silicon, (c) Si nanopillars after removal of the mask and (d) cross-sectional image of 500 nm long Si nanopillars. Insets of (b) and (d) show the corresponding higher magnification SEM images revealing the hexagonal arrangement.*[49]

1.10 Block copolymers for bioapplications

The range of morphologies and surface patterns generated by BCPs are hugely advantageous towards miniaturisation on integrated circuits for the semiconductor industry as aforementioned. The large majority of research of these materials is aimed at these applications. However, there are also many applications for such surfaces and nanostructures in the biological and biomedical field. In recent years, there has been a drive for the development of smart surfaces capable of killing pathogens and bacteria present on the surface of phones, hospitals tools and food packaging. [50-52] To prevent biofilm formation and the spreading of bacterial infections, these surfaces must be chemically or structurally modified. Chemical modification of the surface is undesirable due to several disadvantages. The interaction of a modified antibiotic surface with the bacteria is limited to the top layer of the biofilm, with little effect on the bacteria within the microcolonies. Once a biofilm is formed the colonies become increasing difficult to attack.[53] The limitation for antibiotics to penetrate the biofilm allow for antibiotic resistance to build over time which is the leading cause for antibiotic failure against biofilm formation.[54, 55] For these reasons, modifying surface properties without chemically changing the surface has been of interest to tackle this problem. Research has shown biofilm formation can be inhibited if the bacterial adhesion is prevented at the initial stage.[56] Therefore killing bacteria upon contact at the surface interface is crucial.

Consequently, several studies have been explored to kill bacterial through a physical mechanism. Bioinspired surfaces are highly researched as several species are known to have antibacterial surfaces that kill microbes upon contact with the surface. The effects are due to the presence of nanopillar structures, typically ranging from 50nm – 250nm in height with different densities present on the surface. Although the exact killing mechanism is still under debate, it is thought these nanopillars impale bacteria upon contact causing rupture of the cell wall, leading to cell death.[57] Cicada wing nanostructures are one bioinspired surface of interest. The surface of cicada wings has been studied and characterised, see Figure 1.17. These surfaces have shown to have bactericidal effects and antibiofouling properties.[58, 59] Ivanova et al. were this first to report on these unique properties displayed by cicada wings. The nanopillar surface structures are extremely effective at killing *Pseudomonas aeruginosa* cells in a matter of minutes. Moreover, this effect is physio-mechanical and the properties remained when the chemistry of the surface was modified. [58]

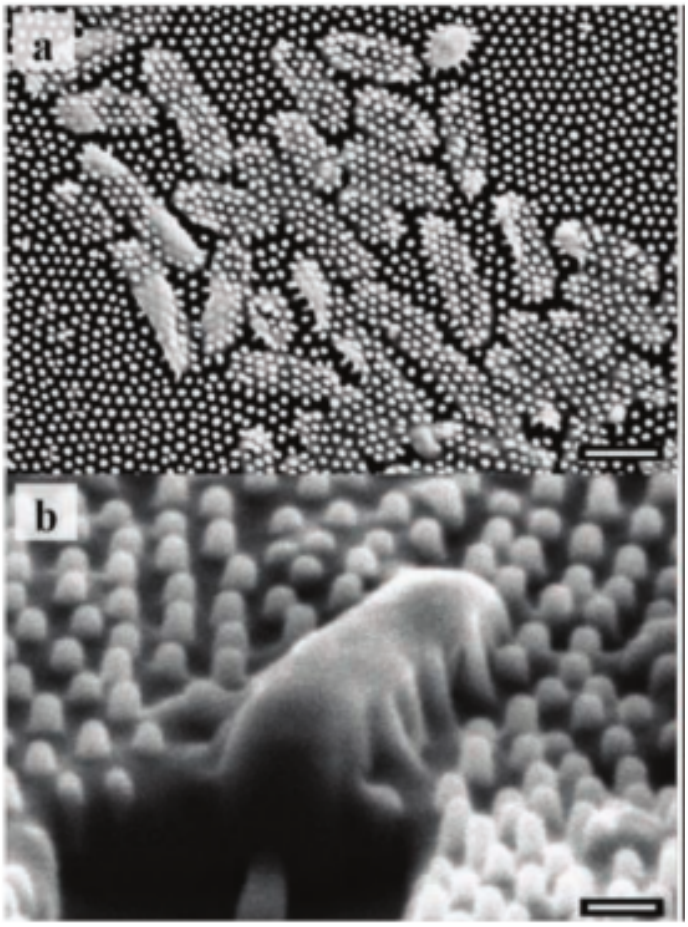

Figure 1.17 *a) SEM micrograph Pseudomonas aeruginosa cells on the surface of a cicada wing. b) Side-on SEM micrograph of Pseudomonas aeruginosa on cicada wing. In both images, the bactericidal effect of the wing is demonstrated. The cell can be seen to sink between the nanopillar.*[58]

Kelleher at al. have carried out a detailed investigation of several species of cicada wings and their bactericidal activity. Their work shows two cicada species were successful in killing *Pseudomonas fluorescens*, a gram-negative bacterium, through impalement causing rupture of the cell wall leading to cell death, see Figure 1.18. Moreover, their work demonstrated that there is a correlation between the level of bactericidal activity and nanopillar size and structure.[59]

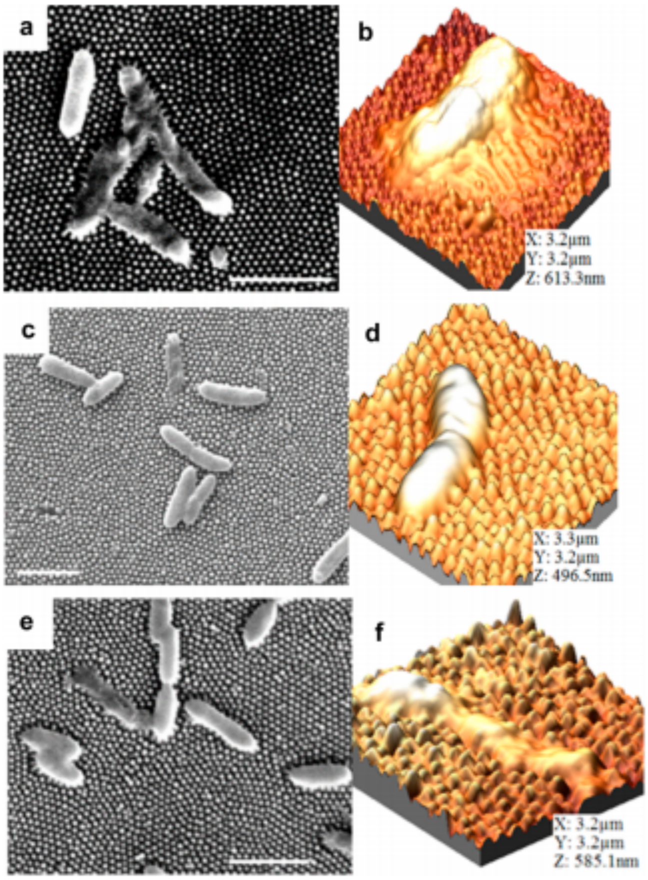

Figure 1.18 *SEM images of fixed bacterial cells on cicada wings. Scale bars on SEM images are 2 µm in length; atomic force microscopy (AFM) images of bacterium on cicada wings. All AFM images are 3.2 × 3.2 µm.*[59]

Watson and co-workers have investigated antibacterial properties of gecko skin. Gecko feet are usually investigated for their unique adhesion properties, however, the surfaces of the skin contains dome shaped scales with hexagonal ordering. These scales consist of closely packed spinules with lengths ranging from hundreds of nanometres to microns, see Figure 1.19. The nanostructured skin exhibit super-hydrophobic properties which can self-clean. They have investigated the antibacterial activity using *Porphyromonas Gingivalis,* a Gram-negative bacterium.[60] The multifunctional surface is a potential template for synthesis of manufactured surfaces through replica molding techniques.

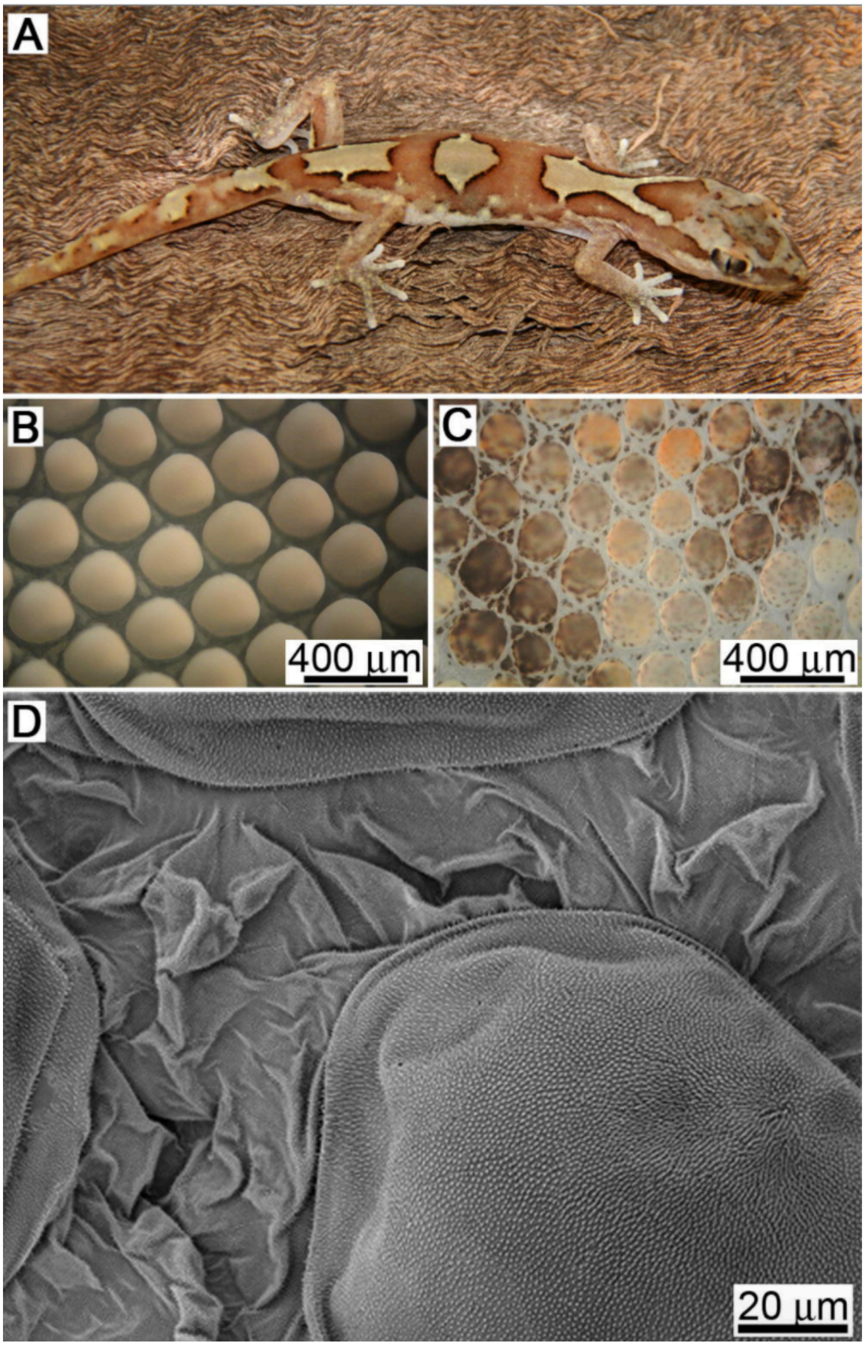

Figure 1.19 *a) Photograph of the gecko Lucasium Steindachneri. b) Optical image showing the micro structuring of the outer skin of the gecko and c) dorsal region. These regions primarily consist of dome shaped scales in a relatively close-packed hexagonal patterning. d) Topographical SEM image of the epidermal dome regions (scales) and areas between scales on the dorsal region of the lizard.*[60]

It goes without saying that the natural surfaces described above cannot be scaled up to allow mass production of antibacterial surfaces. They are also extremely delicate and can be damaged easily. For these reasons, another method to generate surfaces with similar structures and properties must be investigated. Soft lithography techniques can be used to harness these nanostructure surfaces, using industry relevant materials such as poly (ethylene glycol) diacrylate (PEGDA). Coined by Whitesides et al., 'soft lithography' was first employed as an alternative to photolithography for use in nanofabrication. The process involved using a stamp, mold or master, which was fabricated by an elastomer, typically PDMS.[61, 62] They explored numerous techniques, one of which was replica molding. Possible with UV or temperature curable polymers, the process is simple and outlined in the schematic in Figure 1.20. The technique allows the fabrication of three-dimensional topologies in one processing step and can generate complex structures reliably, in a cost-efficient way.[63]

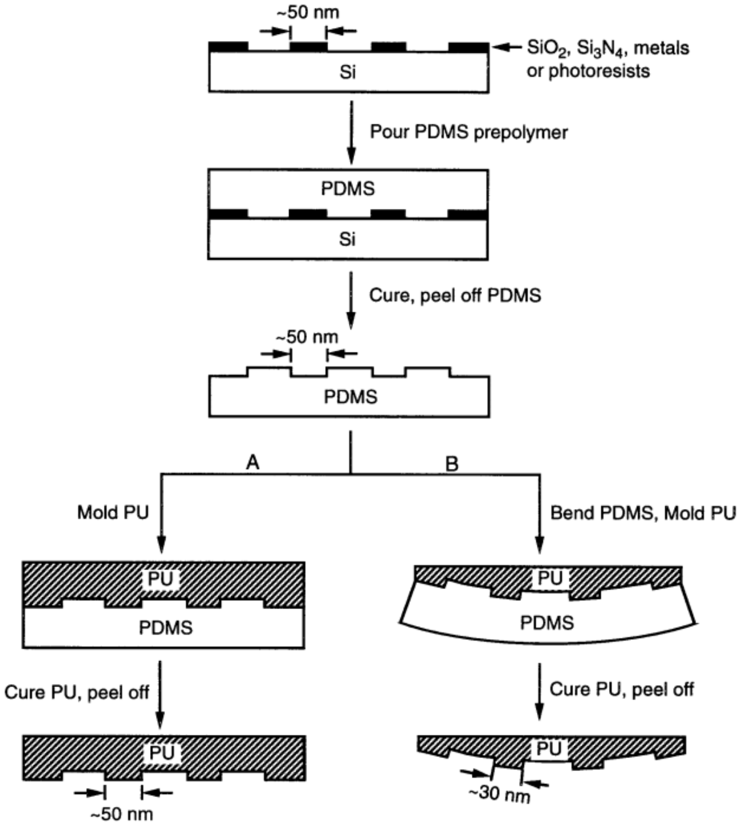

Figure 1.20 *Schematic procedure replica molding against a PDMS mold. The PDMS mold is fabricated by casting against nanostructures fabricated using x-ray lithography or e-beam writing. Replica molding conducted using deformed PDMS, shown in (B). The dimensions of the lines were reduced in this process while the spacing between the lines increased slightly.*[63]

The master mold is predominantly fabricated by photolithography, which is molded using PDMS to create a primary mold. This in turn is molded to create a secondary mold, a replica of the master mold. The secondary mold is usually formed using a different polymer material than the primary mold, in this case polyurethane (PU). This will limit the interaction between both polymers during the curing phase, allowing easy separation of the molds. [63, 64] Xia and co-worker also found that a master mold could be used to generate >30 replicas without showing reduction in the quality of molds. This was the first-time nanostructured materials could be patterned with the properties of this elastomer. Molds were easily bent, stretched and compressed. Since the first reporting of the process, replica molding has been shown to generate structures at the nanoscale from silicon masters. [65-67] and even biological masters, such as a blue morpho butterfly wing.[68]

In addition to antibacterial applications, Park et al. have carried out exciting research between the interactions of nanopatterned surfaces with mammalian cells. These surfaces of nanopatterned polystyrene showed the ability to regulate the differentiation of human adipose-derived stem cells (ASCs). Here, nanopores and nanopillars are fabricated through hot-embossing of anodic aluminium oxide (AAO) templates. The resulting porous surfaces induced higher adipogenic differentiations of ASCs where the pillared surfaces induced higher osteogenic differentiation.[69] Similarly, Wei et al. demonstrated how an array of polypyrrole nanotubes and nanotips could alter surface adhesion leading to differentiation of mesenchymal stem cells (MSCs). Their work highlighted that switching from nanotubes to nanotips through an electrochemical oxidation/reduction process resulted in controllability of the wetting properties of the surface. When investigated with MSCs, this electrochemical switching led to dynamic attachment and detachment to the MSCs at the nanoscale. This process activated intracellular mechanotransduction and osteogenic differentiation independent of surface stiffness and chemical induction. Thus, providing an alternative to classical cell culture substrates for regulating stem cell fate commitment. [70] Although both studies use different methodologies to fabricate nanostructured surfaces, this work highlights where BCPs can be utilised in bioapplications.

Phillip et al. have proposed using the porous membranes easily prepared by BCPs systems as water filtration membranes.[71] Their work reports 24nm diameter monodispersed nanoporous membranes fabricated from polystyrene – *block* – polylactide (PS – *b* – PLA) system on top of a microporous structure. The microstructure provides a strong reinforcement needed support the BCP, by exploring numerous solvents they achieved perpendicular orientation of the BCP on top of the microstructure substrate, see Figure 1.21. The membranes have shown to be successful at rejecting PEO solutes from 14.0 kDa to 100.0kDa. [71]

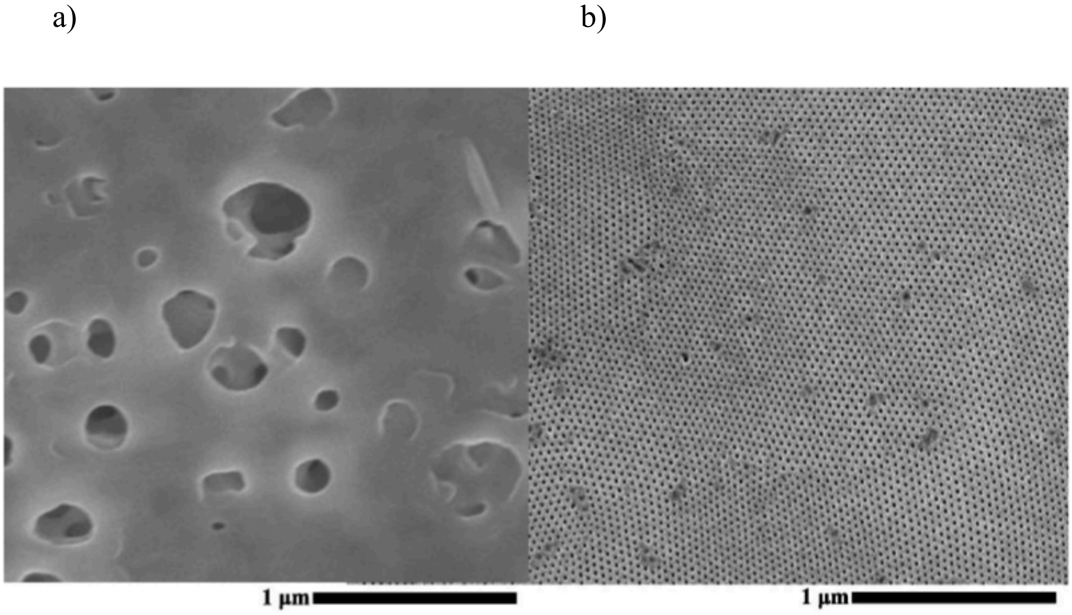

Figure 1.21 *a) Microporous substrate PS – b – PLA is spin coated onto. b) nanopores produced by solvent annealed PS – b – PLA. PLA cores have been removed by an acid wash.*[71]

Recently, Song et al. have demonstrated a nanopillar arrayed triboelectric nanogenerator as a self-powered sensor for sleep monitoring. In their work, they have used AAO templates to fabricate an aluminium−plastic laminated film with a nanopillar array, which in turn is used in a triboelectric nanogenerator. The self-powered and sensitive device has been demonstrated as a smart body motion sensor of sleep monitoring for diagnosis of sleep disorders due to its high sensitivity and excellent stability.[72]

Nanoneedle arrays have also displayed the ability for drug delivery as well as intracellular sensing and single-cell stimulation through direct contact to the cell cytoplasm. The minimal invasive impact of nanoneedle arrays to the membrane and endolsosomal system enables this process. Leaders in the field, Stevens et al., have recently reported on a biodegradable mesoporous silicon nanoneedle array that exhibits tight intercede with the cell rapidly negotiating local biological barriers to grant temporary access to the cytosol with minimal impact on cell viability. See Figure 1.22. [73]

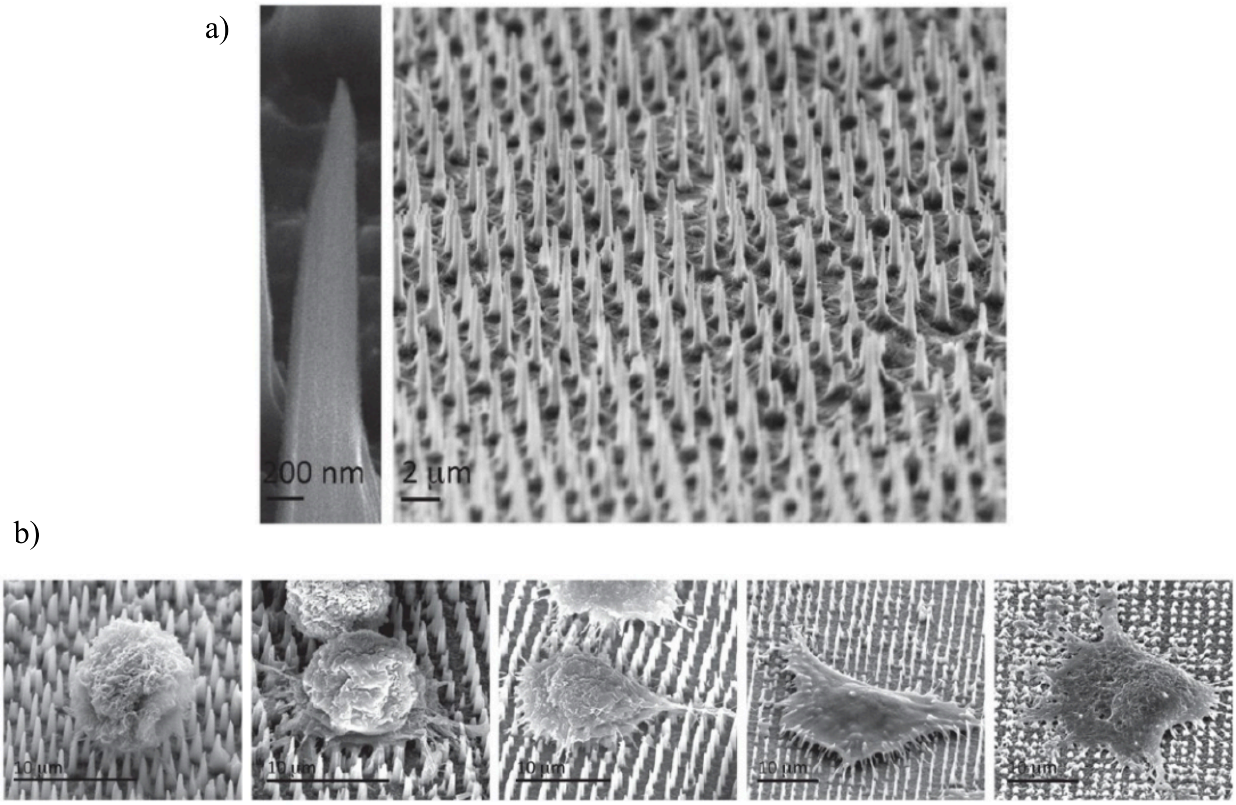

Figure 1.22 *a) SEM images of porous silicon nanoneedle array. b) SEM images showing retained cell morphology over 72 hours.*[73]

Their work demonstrated delivery of cell-impermeant quantum dots *in vivo* and live intracellular sensing of pH. The fast application of nanoneedles *in vivo* to the surface of tissues resulted in the localised delivery of quantum dots to the superficial cells and their prolonged retention. This work not only provided an understanding of the dynamics of nanoneedle surfaces, but highlights the ability to carry out highly local intracellular delivery of drugs with live tissues.[73]

It must be noted that certain surfaces described above are in the microscale and are not in the nanoscale, demonstrated with the some BCP systems previously mentioned. However, this innovative work demonstrates other areas in which BCPs can be used to prepare nanostructured surfaces, outside of the semiconductor industry. Using these highly-researched materials for areas other than next generation technology is exciting and worthwhile investigating.

1.11 Thesis Outline

This chapter has provided a general literature review of the mechanisms which control the self-assembly of BCPs to enable the formation of nanostructures on surfaces. The use of these materials in lithographic and biomedical application has been discussed briefly. Chapter two describes the characterisation techniques used in this project, outlining the fundamental properties of each procedure. Chapter three discusses the materials, instrumentation and experimental methods used for this work. Chapter four focuses on the development of a highly-controlled annealing process of PS – *b* – P4VP in a custom built solvothermal annealing chamber. This work not only eradicated the disadvantages associated with static annealing methods, but allowed the fabrication of ideal BCP templates resulting in hexagonal ordered P4VP cores in a PS matrix.

Chapter five outlines an investigation into the removal of P4VP from a PS – *b* – P4VP film using plasma. In this work, oxygen, argon and nitrogen plasmas were investigated with the aim to selectively remove P4VP over PS. A key finding was that nitrogen plasma was successful in removing P4VP over PS, with further etch investigations into P2VP leading to the hypothesis that the nitrogen in the aromatic ring of P4VP places a vital role in the etch rate. Chapter six discusses the preliminary results for the modification of a preferential polystyrene brush layer to a neutral brush layer to control BCP orientation. The rationale behind this work was to gain an understanding into what are the key contributors to BCP orientation. This work showed how a PS brush layer wettability and surface energy was modified when exposed to an oxygen plasma. This modification was shown not to be attributed to changes in surface topography, but changes in surface functionality. BCP annealing on top of plasma modified brush layers provided and insight into how the addition of oxygen effects BCP orientation.

Chapter seven focuses on using the processes optimised in chapter four to fabricated silicon nanopillar arrays. Before this was carried out, methods were optimised using a test substrate, nanostructured cicada wings. Replica molding enabled polymer replicas of the cicada nanostructure to be fabricated. The swelling properties of these materials were investigated by performing air and aqueous AFM. Results showed that the polymer swelling properties cause that the nanopillar structure to increase in size.

Using the solvothermal annealing chamber, BCP templates were prepared, which were transferred into the silicon substrate by converting the BCP into a hard mask. Silicon etching of the samples generated silicon nanopillar arrays. Using optimised replica molding methods, PEGDA nanopillar surfaces were fabricated. These polymer surfaces were tested for antibacterial activity, with results showing nanostructured surfaces with pillars greater than ~50nm had high antibacterial effect when compared to unpatterned surfaces and nanostructured surfaces with pillars less than 50nm.

Chapter Two

2 Characterisation Techniques

This chapter discusses the characterisation techniques utilised in this work. Film thickness calculations were determined by ellipsometry and reflectometry. Wettability and surface energy was determined by calculating the contact angle of the surface using both water and diiodomethane. Surface topography and sample images were obtained using atomic force microscopy and field emission scanning electron microscopy. Surface analysis was performed using attenuated total reflectance, secondary ion mass spectrometry and X-ray photo electron spectroscopy. Plasmas were characterised using optical emission spectrometry.

2.1 Ellipsometry

Ellipsometry is an optical characterisation technique used for measuring thickness and crystalline nature of materials. The method measures the change in polarisation of a monochromatic light source reflected at a slanting angle of incidence. This technique is indirect, meaning that the returning polarised light does not in fact directly relay the relevant data and must instead be interpreted and analysed in optical models. The method is powerful and sensitive with a resolution as high as 0.01nm for thickness values.[74] The signal measured is the change in polarisation as the incident radiation interacts with the material. The polarisation change is quantified by the amplitude ratio, Ψ, and the phase difference, Δ. This measured response depends on the properties of the material such as thickness and crystalline nature, thus these properties can be determined.[75] In this study, ellipsometry is the workhorse for measuring the thickness of polymer thin films.

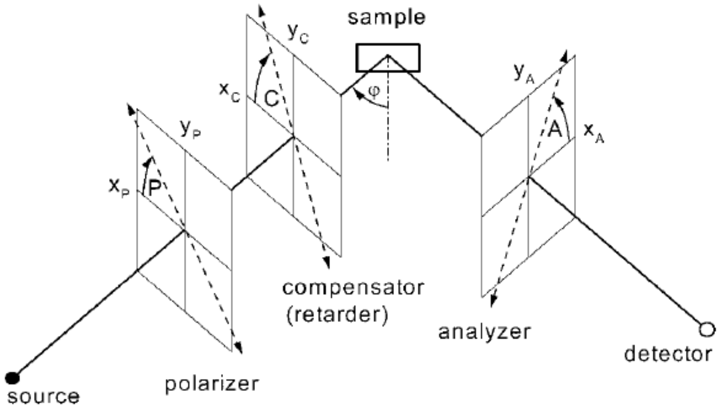

Figure 2.1 *Schematic of ellipsometer set-up.* [74]

2.2 Spectroscopic reflectometry

A reflectometer is an instrument used for the determination of film thickness, refractive index and surface roughness of thin films. The principle behind reflectometry is absolute reflectance spectroscopy, which analyses the intensity versus wavelength of light reflected from a sample to extract the measurement. The spectrometer uses light at normal incidence to the sample surface. There are three ways in which this light can be reflected:

1. Light is reflected from the top of the thin film
2. Light transmits into the film.
3. Light is transmitted into the film, reaches the substrate surface and is reflected.

The light from each of these reflections recombines to generate varying levels of constructive and destructive interference depending on the wavelength of light and the optical distance the light travels. A model is used to fit the reflected intensity versus wavelength data to extract film thickness and other measurements.[76] Spectroscopic reflectometry was used to determine *in situ* film thickness measurements during solvent annealing in this work.

2.3 Water Contact Angle

Surfaces are characterised as hydrophilic or hydrophobic by measuring contact angle (θ) of a sessile drop on a surface; this is the angle usually measured through the liquid, where the liquid-vapour interface meets the solid surface. Although a relatively simple characterisation method, the contact angle of a surface influences a range of properties, such as the adhesive capabilities of the surface, biological interactions, and flow capabilities.[77, 78] The shape of a droplet at the interface of a surface is determined by the Young-Laplace equation, with the contact angle (θ) value being utilised as a boundary condition for the equation.[77] The Young equation (2.1) assumes a perfectly flat and homogenous surface, with θ_C being used as the equilibrium contact angle.

$$\gamma_{SV} = \gamma_{SL} + \gamma \cos\theta \qquad (2.1)$$

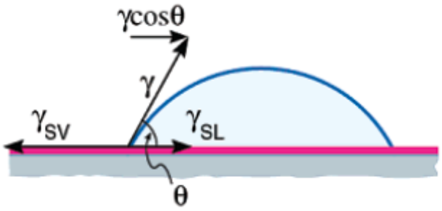

Figure 2.2 *Schematic representation of contact angle constituents between a liquid droplet and a solid surface.*[79]

In this equation, γ_{SV} represents the surface energy of the substrate, γ_{SL} represents the interfacial tension between the solid and the liquid, and γ represents the surface tension. Although this idealised equation gives a good indication of a surfaces contact angle, the actual value will likely cover a spectrum of different angles, as the surface contact is also dependant on a range of other interfering constituents, such as surface roughness. By measuring the advancing or receding contact angle and not just static contact angle, these difficulties can be overcome; when a droplet on a surface is decreased in size by withdrawing water from the droplet with a micro-syringe, the droplet will decrease in volume and in contact angle. As the droplet recedes it maintains contact with the surface and thus maintains the same constant receding angle, $\theta_{R.}$ This receding angle will be characteristic of the surface topography and chemistry.

On the other hand, if this droplet is increased in size by adding water to the droplet with a micro-syringe, the droplet will increase in volume and contact angle. As the droplet advances across the surface it remains in contact with the surface until the droplet begins to advance. Once advancing across the surface it does so at a constant advancing angle, $\theta_{A.}$ This advancing angle will again be characteristic of the surface features and chemistry. Therefore, it is more important to measure advancing or receding angles of a surface in question rather than static contact angle. Metastable angle is less significant and only designates and angle somewhere between θ_R and θ_A [80, 81] In this thesis, all contact angles reported are advancing contact angles.

Moreover, once contact angles are determined, these values can be used to measure the surface energy of the surface. The surface energy of a material quantifies the disruption of intermolecular bonds that occur when a surface is created. Surface energy can also be described as the work which must be expended to increase the size of the surface of a phase and is referred to as the surface free energy.[79] In this study the Owens, Wendt, Rabel and Kaelble (OWRK) method is used to calculate surface energy. This method distinguishes between a polar and a disperse component of the surface energy and uses the geometric mean of these in the expression for γ_{SL}, the liquid-solid interface. Using this method, two liquids of known polar and disperse parts must be used. Herein, contact angle of water and diiodomethane were used to calculate surface energy. This method of calculating surface energy is applicable to surfaces with low charge and moderate polarity, therefore is best for polymer thin films.[82, 83]

According to Young's equation, there is a relationship between the contact angle θ, the surface tension of the liquid γ_{LG} , the interfacial tension, γ_{SL} between liquid and solid and the surface energy γ_{SG} of the solid. Therefore, by measuring the contact angle, the surface energy can be calculated. To be able to calculate the surface free energy by the OWRK method from contact angle measurements, at least two liquids with known disperse and polar parts of the surface tension are required to determine the surface free energy of the solid, wherein at least one of the liquids must have a polar part.[79, 82]

2.4 Atomic Force Microscopy

Binnig and Rohere won the Nobel in Physics for their invention of the scanning tunnelling microscope in 1986.[84] This invention led to many other scanning probe microscopes, with atomic force microscopy (AFM) being the most successful of these new techniques. Arguably the most versatile and powerful microscopy technology, this system operates by measuring the force between a probe and the sample surface. The probe in this case is a sharp tip, usually pyramidal in shape and composed of silicon, which is mounted on a cantilever spring, see Figure 2.3. To acquire an image, AFM measures the vertical and lateral deflections of the cantilever optically by reflecting a laser beam off the tip. [84-86]

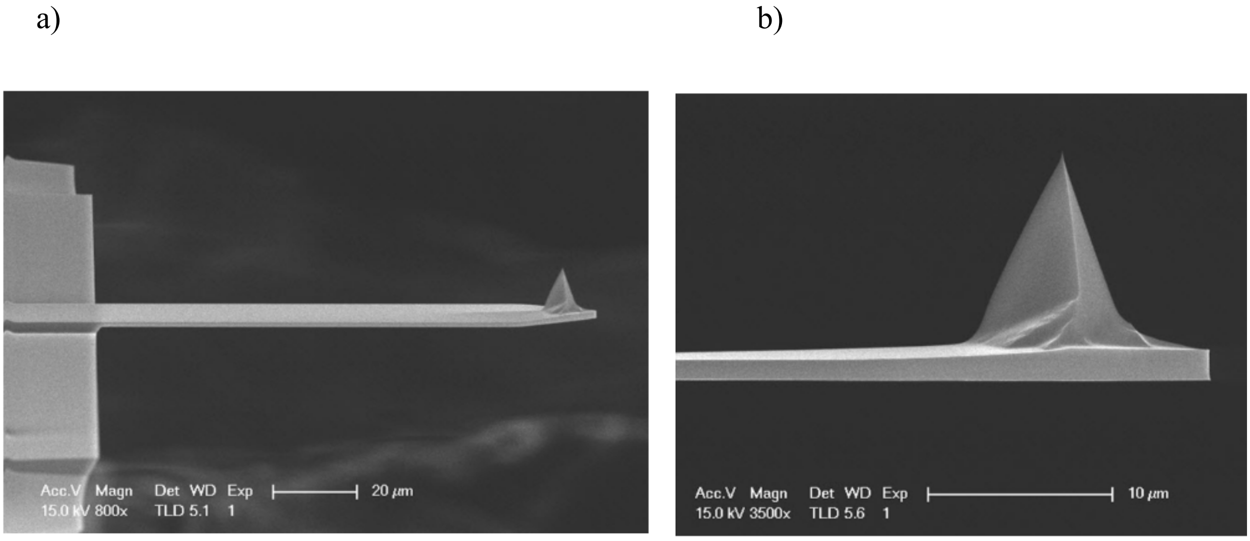

Figure 2.3 *a) SEM micrographs of an AFM cantilever, b) SEM micrograph of an AFM tip.*[87]

Generally, the sharp tip (probe) is loaded into the sample holder and is brought into close contact to the surface, keeping deflection at a constant. The atomic interaction forces between the surface and the tip lead to cantilever deflection due to forces exerted by the surface topography. The laser is the used to detect these deflections by reflecting an incident beam off the flat top of the cantilever to a photosensitive photo diode (PSPD), which then tracks the changes in deflections.[86] The movement of the probe over the surface is controlled by a piezo scanner, which provides precise movement between the x, y and z scales. The signal from the PSPD passes through a feedback circuit, into the z-movement part of the piezo to ensure the distance between the probe and sample is a set value. Deflections are recorded by the laser and relayed to the PSPD. By using a feedback loop to accurately control the position of the tip above the surface and maintaining constant laser position, accurate topographic maps of the surface can be generated.[85] A cartoon representation of AFM set-up is shown in Figure 2.4. This characterisation technique not only provides a three-dimensional topographical image, but also other surface measurements such as surface roughness and elasticity of samples can be obtained. AFM generates atomic resolution images with minimal sample preparation or damage. [84] AFM can be performed is various modes, most common are contact mode and tapping mode.

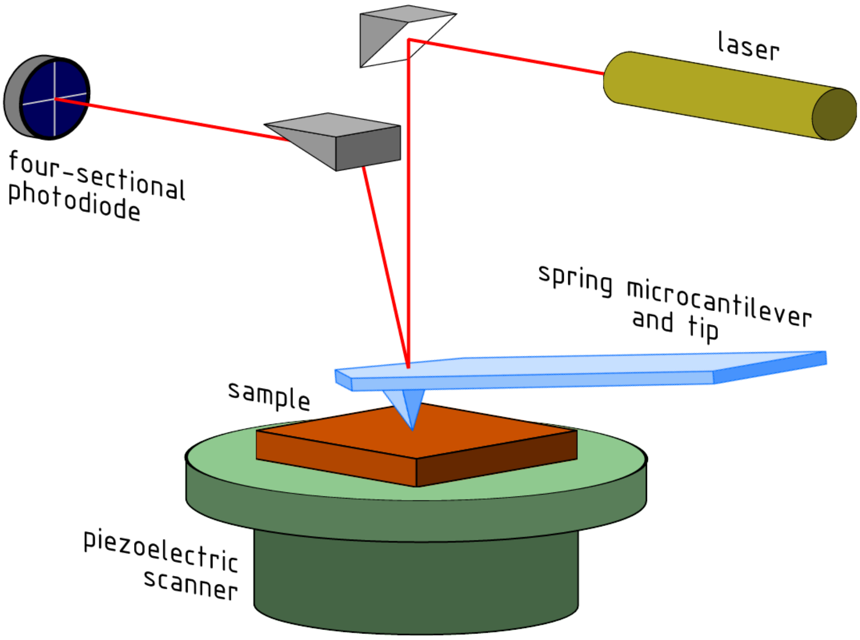

Figure 2.4 *Schematic representation of AFM set-up.*[88]

During contact mode, the probe is in continuous contact with the sample when moving across the surface. The topography of the surface is measured using either the deflection of the cantilever or the feedback signal required to keep the cantilever at a constant position. Limitations associated with this mode are sample and tip damage. As the probe drags across the sample during imaging, soft samples can become damaged easily as well as the tip picking up material during scanning. In the ambient, samples usually develop a liquid meniscus layer due to humidity in the atmosphere. This causes the short-range forces between the tip and the sample, leading to samples becoming difficult to measure due to the tip sticking to the surface. It was this problem which led to the development of tapping mode. In this method, the cantilever is driven to oscillate at a set resonance frequency. This oscillation is achieved using the piezo element within the cantilever holder. The amplitude of this oscillation can range from a few nanometers up to 200nm. The amplitude of the oscillation is used as the feedback parameter. As little contact between the sample and the probe occurs in this mode, sample and tip damage is avoided while still obtaining accurate topological images.

2.4.1 Liquid AFM Imaging

For samples which require aqueous environments, liquid AFM can be carried out. Not only is this beneficial for biological samples, supple or delicate samples that can be easily damaged using conventional AFM can be imaged in liquid for a softer approach. It also allows for samples to be compared in different mediums.[89] In this work two liquid imaging techniques were used. The first method was carried out in collaboration with NASA Ames Research Center. Here a Bruker Multimode AFM tool equipped with a Veeco flow cell was used for imaging. Figure 2.5 shows a photograph and a schematic diagram of the fluid cell. This cell is predominately used for tapping mode, force modulation, and contact mode experiments in liquid. Since using conductive liquids can potentially damage the piezoelectric actuator, the flow cell is designed to insulate and separate it from the liquid media.

From Figure 2.5 (b) the cantilever (1) is placed in a small groove in the centre of the O-ring (3) and held in position by a clip and a spring (2). The silicone O-ring provides an enclosed fluid environment between the fluid cell and the scanner. The flow of liquid to this enclosed environment is controlled by two microchannels (4). The piezoelectric material is positioned above one of the supporting holes (5) and the wire from it passes through the fluid cell to connecting chip (6). This design ensures the whole electronic system is completely insulated from the fluid.[90]

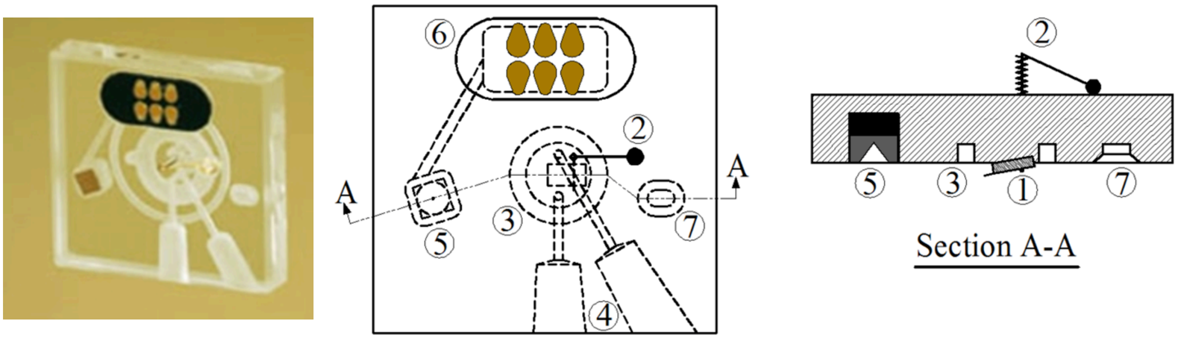

Figure 2.5 *Photograph and schematic of Veeco flow cell model number MTFML.*[90]

However, using a system described above can have its disadvantages. The spring holding the chip in place can become weak and unsecure. If the O-ring isn't sealed perfectly the system will leak. This flow cell is designed for predominately flat surfaces; if the sample isn't completely flat and fails to provide a good seal, the system will leak. One of the advantages of using liquid AFM is that you can image supple samples. However, using this flow cell, a strong seal between the O-ring and sample is required. If samples are delicate, they can be easily damaged leading to the sample breaking and debris being suspended in the liquid media. [90]

For these reasons, other such liquid AFM protocols have been studied. In collaboration with The Conway Institute, UCD, AFM imaging using no flow cell was carried out, see Figure 2.6. This set-up can only be used in a system where the original tip holder can come in contact with fluids and not be damaged. The process is simple in nature, a droplet of the medium is placed on the sample. The tip holder is lowered until a meniscus is formed between the sample and the tip holder. After this point, the tip can approach the surface and imaging can begin. Using this set-up, the limitations associated with flow cells can be overcome. All liquid AFM in this work was carried out using this imaging method.

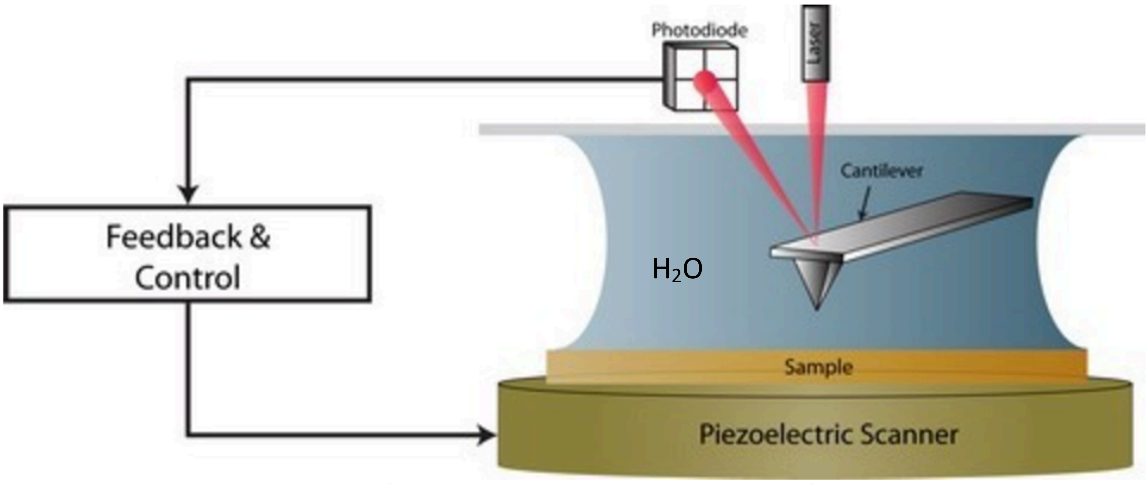

Figure 2.6 *Schematic representation of liquid AFM set-up using no flow cell.*[91]

2.5 Scanning Electron Microscopy

Scanning electron microscopy (SEM) is a widely-used characterisation technique to generate images of nanostructured and microstructured materials. This method focuses a beam of high-energy electrons over the sample to image it. The electrons are formed by passing high current through a tungsten filament; electrons are accelerated towards an anode and are focused in the column by various lenses. The electrons from the beam interact with the sample, which in turn produce a variety of signals that can be used to obtain information about the surface topography and composition.[92] A schematic representation of a SEM tool is shown in Figure 2.7. A SEM contains five major components:

1. The source of electrons
2. The column in which the electrons travel
3. Electron detectors
4. Sample chamber
5. A computer to view the image

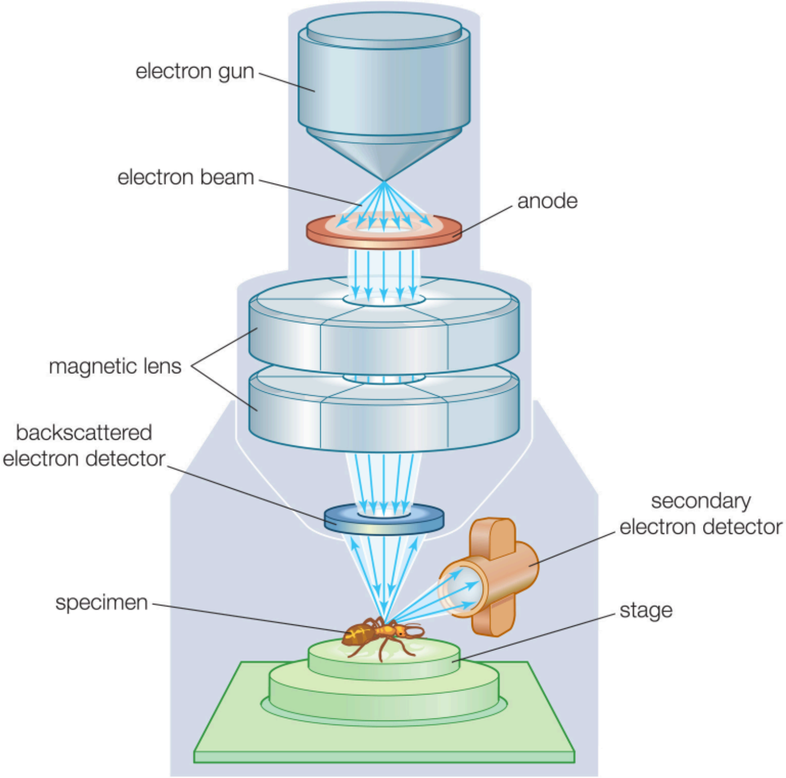

Figure 2.7 *Schematic representation of SEM.*[93]

The sample is loaded in the sample chamber, after which the chamber is evacuated by means of a pump and the sample is placed under the column. Electrons are generated at the top of the column before being accelerated down the column where the beam can be focused using a range of lenses and apertures. Once electrons come into contact with the sample; they penetrate deep into the sample surface depending on the accelerating voltage and the density of the sample. In doing so, they produce secondary electrons, backscattered electrons and characteristic X-rays, see Figure 2.8. A detector is then used to form an image of the sample by collecting these signals. Secondary electrons and backscattered electrons are most commonly detected and used to fabricate an image. Secondary electrons are generally used to show morphology and topography of a sample while backscattered electrons are more valuable for obtaining information about the composition of the material.[92, 94]

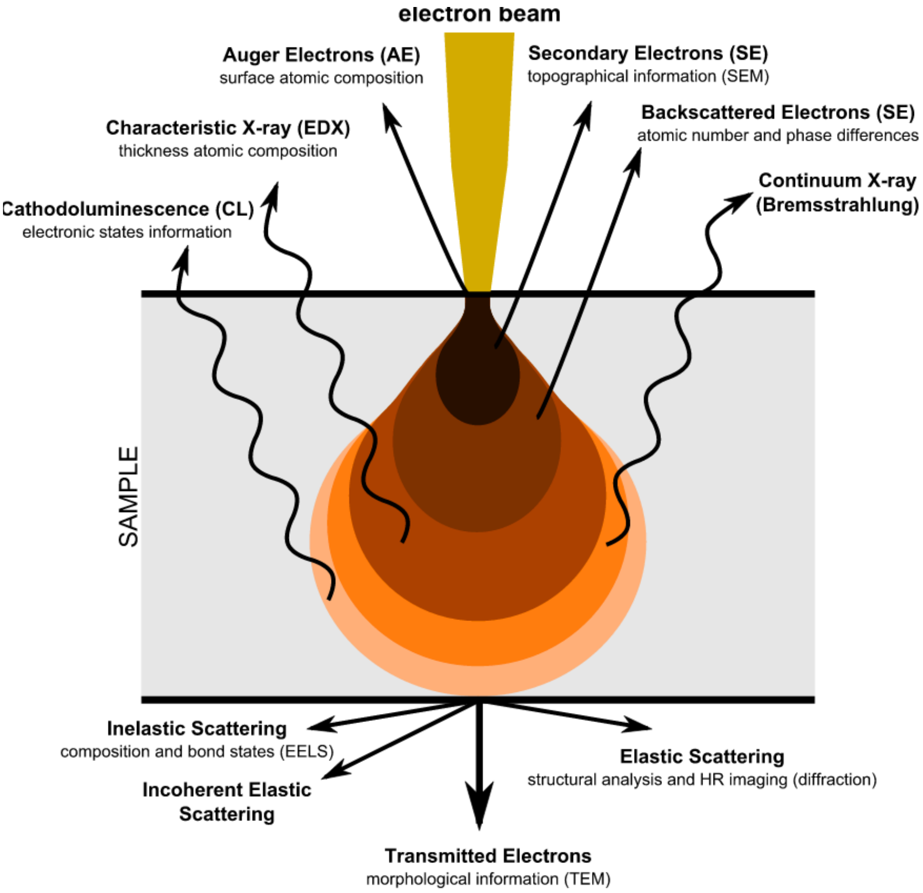

Figure 2.8 *Schematic representation of electron interactions with a sample.*[95]

SEM is the principle characterisation technique for obtaining images in the microscale and down to around 200nm. To obtain high-resolution images for samples with features below 200nm a field emission SEM (FESEM) must be used. The main difference between SEM and FESEM is the emitter. Instead of a conventional thermoionic emitter a field emitter is used. In this set-up, the filament is not heated to generate electrons, a large electrical potential gradient is utilised. This electron beam can generate smaller electron spots than conventional SEM and therefore an improved spatial resolution and minimal sample charging and damaged is obtained. All SEM characterisation in the work was obtained using a FESEM tool. Samples can also be coated with a conductive material to enhance imaging. This not only reducing charging but using a high Z material, such as gold, creates high electron scattering.

2.6 X-Ray Photoelectron Spectroscopy

XPS is a highly surface sensitive technique used to identify the chemical species present in surface of a material. This is achieved by irradiating the sample with mono-energetic soft X-rays resulting in the emission of photoelectron which energies are distinctively characteristic of the elements within the sample, see Figure 2.9. The typical depths of analysis can range between 1-10nm. Changing the position of the sample can focus the incoming beam at different angles.

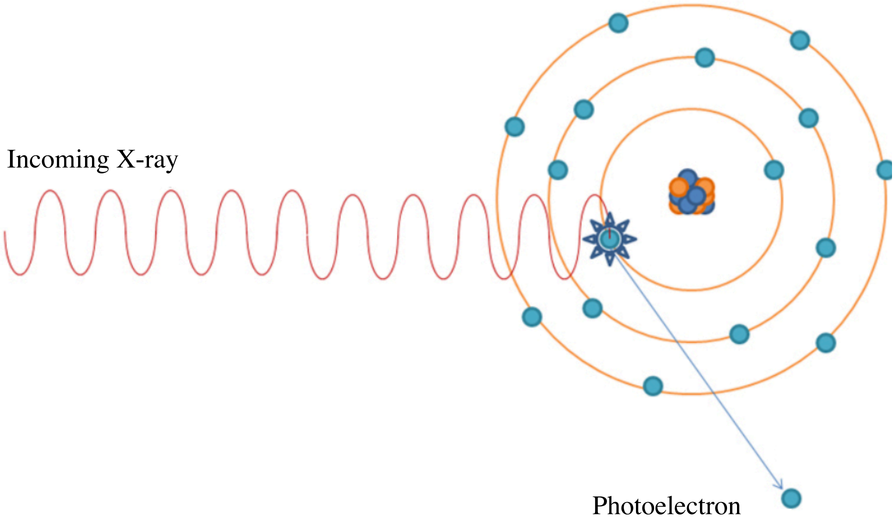

Figure 2.9 *Creation of a photoelectron via the absorbance of an incident X-ray photon.*[96]

Conventional XPS typically utilises a dual X-ray anode configuration of a magnesium (Mg) and aluminium (Al) anode in order to produce characteristic X-ray lines of Mg Kα (1253.6 eV) and Al Kα (1486.6 eV) energies.

As the sample is irradiated by either anode radiation, electrons are emitted from the sample surface via the photoelectron effect with binding energy (E_b) given as equation 2.2.[97]

$$E_b = h\upsilon - KE \qquad (2.2)$$

Where h is Planks constant (6.626 x 10-34 m2 kg/s), υ is the frequency of the electromagnetic radiation which caused the photoelectron to be ejected and KE is the kinetic energy of the electron ejected from the atom. Due to the fact that the photon energy ($h\upsilon$) is well defined, a measurement of the kinetic energy of the emitted electron should give the necessary information needed to obtain the binding energy of the electron from its initial atomic state. In addition, due to the well-defined electron energy levels within an atom, elemental identification can be achieved via the measurement of the kinetic energy of electrons emitted from the sample surface during irradiation from the anode target. The energies of emitted electrons are analysed using an electron spectrometer, with the subsequent recorded data culminating in an X-Ray photoelectron spectrum, which is typically a graph of counts (or intensity) versus electron binding energy. [98-100] A cartoon representation of XPS is shown in Figure 2.10. Collaborators from the Hughes research group in DCU carried out all XPS measurements shown in the thesis.

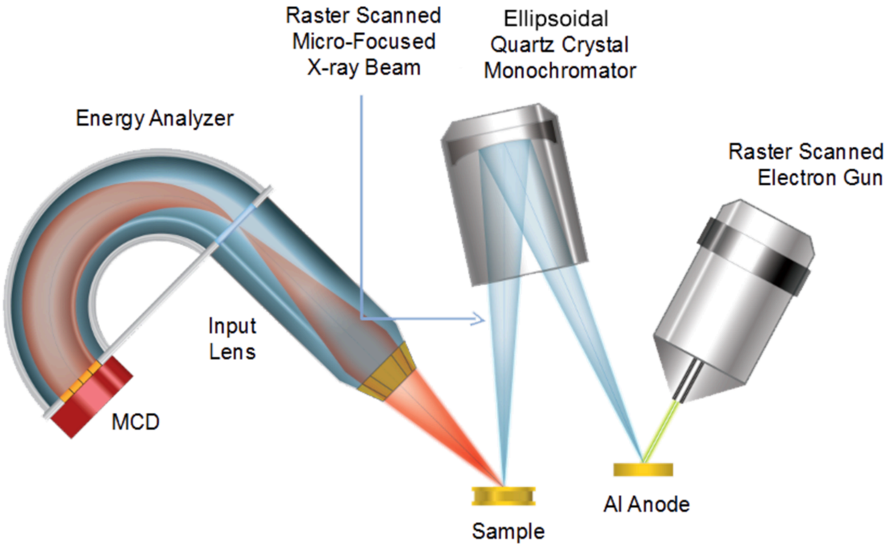

Figure 2.10 *Schematic representation of XPS set-up.* [101]

2.7 Secondary ion mass spectrometry

Secondary ion mass spectrometry (SIMS) is a characterisation technique used to define the chemical composition of solid surfaces and thin films. This is measured by sputtering the sample with a primary ion beam which in turn generates secondary ions from the sample that are measured with a mass spectrometer to determine elemental, isotopic or molecular composition of the surface. Depth profiling to determine information of the sample composition variation below the surface can also be performed using SIMS. Such information is highly beneficial for layered samples. Since SIMS is a naturally destructive technique, a depth profile can be obtained by simply recording sequential SIMS spectra, which will gradually erode the surface exposing under layers. Since there is a large variation in ionisation of materials, it is important to note SIMS is a qualitative characterisation technique. [102, 103] A cartoon representation of SIMS is shown in Figure 2.11.

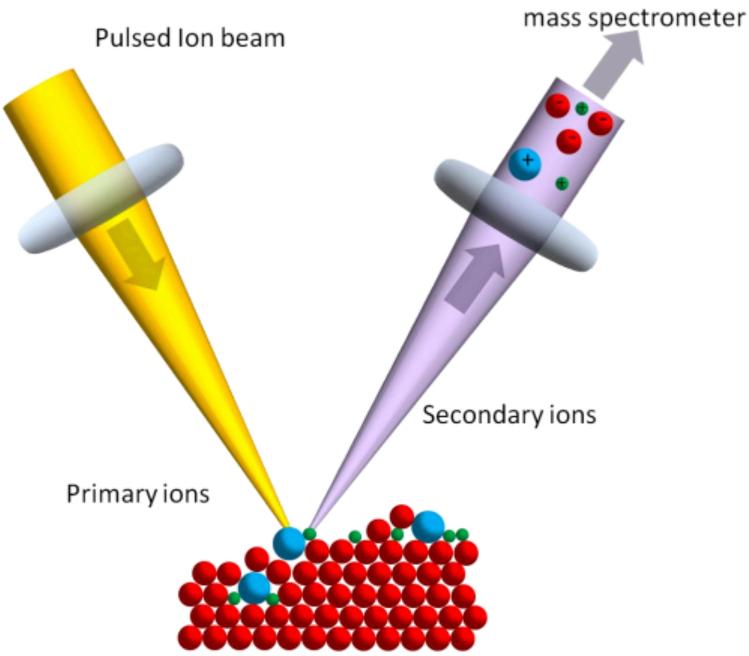

Figure 2.11 *Schematic of secondary ion mass spectrometer set-up.* [104]

2.8 Attenuated total reflectance

Attenuated total reflection (ATR) is a surface technique used in conjunction with infrared (IR) spectroscopy which enables surface functionality to be measured. ATR uses the property of total internal reflection to create an evanescent wave. A beam of infrared light enters the ATR crystal in such a way that it reflects of the sample surface in contact with the crystal. This reflection forms the evanescent wave which extends into the sample. The beam penetrates between 0.5 and 2 microns into the sample surface. The number of reflections can be modified by changing the angle of incidence. A detector is used to collect the beam which exits the crystal. It is important to note that this evanescent effect only works if the crystal is made of an optical material with high refractive index than the sample being studied. Otherwise the light will be lost to the sample. All ATR measurements made in this thesis were carried out using a germanium crystal. The sample is placed in direct contact on the crystal and is firmly clamped in place to ensure that trapped air is not the medium which the evanescent wave travels as this will cause interference. The signal to noise ratio obtained depends on the number of reflections.[105]

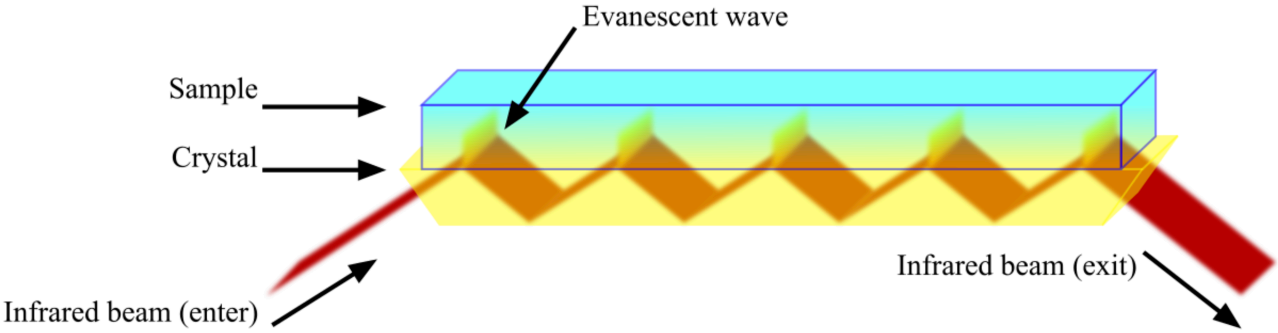

Figure 2.12 *Schematic showing the internal reflections of light as it enters the ATR crystal of high refractive index (shown in yellow) and the sample (shown in blue).*[106]

2.9 Optical emission spectroscopy

Optical emission spectroscopy (OES) is a plasma diagnostic method used for the determination of plasma composition, temperature and energy distribution. The technique is universal for various plasma types and has no influence on the process. OES spectrometers are similar to ultraviolet-visible (UV-VIS) spectroscopy in principle. UV-VIS refers to the absorption or reflectance spectroscopy in the UV-VIS spectral region. Absorption of the UV radiation results in the excitation of electron from the ground state to a higher energy state. The energy of the UV radiation that is absorbed is equal to the energy difference between the ground state and the higher energy state, expressed in equation 2.3 where h is Planck's constant (6.626 x 10-34 m2 kg/s) and f is the frequency of radiation.

$$\Delta E = h\mathrm{f} \tag{2.3}$$

UV spectroscopy obeys the Beer-Lambert law, which states that: *when a beam of monochromatic light is passed through a solution of an absorbing substance, the rate of decrease of intensity of radiation with thickness of the absorbing solution is proportional to the incident radiation as well as the concentration of the solution*, and is expressed as equation 2.4. A is absorbance, I_o is intensity of light incident on sample cell, I is intensity of light leaving the sample, c is molar concentration of solute, l is length of sample cell and ε is molar absorptivity.[107]

$$\mathrm{A} = \log_{10}\frac{I_o}{I} = \varepsilon c l \tag{2.4}$$

From the Beer-Lambert law it is clear that greater the number of molecules capable of absorbing light of a given wavelength, the greater the extent of light absorption. This is the basic principle of UV spectroscopy. OES spectrometers have much higher spectral resolution than UV-VIS with some instruments reporting better than 0.01nm resolution. The gratings with density higher than 300 gr/mm are used for overview spectra. Adjustable slits are positioned at the entrance of the spectrometer.[108] The measurement is made by placing an optical fibre against the plasma chamber viewport and ensuring no external light is measured by covering the port with black cloth. OES spectrometry was used to compare the characteristics of different plasma chambers in this thesis.

Chapter Three

3 Experimental

3.1 Materials

Diblock copolymers were purchased from Polymer Source, Canada and used without further purification. PS – *b* – P4VP molecular weights were 24,00 kg mol^{-1} and 9,500 kg mol^{-1} with a polydispersity index (PDI) of 1.10. PS – *b* – PMMA molecular weights (Mw) were 46,100 kg mol^{-1} and 21,000 kg mol^{-1} with a PDI of 1.09. PS – *r* – PMMA molecular weight was 15,000 kg mol^{-1} with a PDI of 1.2 and a styrene content of 58 mol %. Polystyrene homopolymer Mw 35,000 kg mol^{-1}, P4VP homopolymer Mw 60,000 kg mol^{-1}, P2VP Mw 37,500 kg mol^{-1}, sulfuric acid (98%), hydrogen peroxide (30 wt%), toluene (98% anhydrous), tetrahydrofuran (THF) (99.8% anhydrous), ethanol (dehydrated, 200 proof), acetone (99.0% anhydrous), iso-propanol (IPA)(99% anhydrous) ethylene glycol (95%), iron(III) nitrate nonahydrate, 2-Hydroxy-4′-(2-hydroxyethoxy)-2-methylpropiophenone (98%), poly(ethylene glycol) diacrylate Mw 575g/mol, Poly(propylene glycol) diacrylate Mw 800g/mol were purchased from Sigma Aldrich, Dublin, Ireland. P-type silicon was donated by Intel Ireland. AFM probes with force constants ranging from 0.5 – 40 N/m were purchased from Windsor Scientific.

3.2 Instrumentation

The solvothermal chamber was custom built for processing BCP films on substrates with diameters up to 4 inches. The chamber consists of a stainless-steel ISO straight connector (full nipple) part with 4 x KF 40 fittings (90° intervals) machined around the chamber with an internal volume of 1.94 litres. Two Swagelok feedthroughs are used for gas in and out lines and a 9-pin SubD feedthrough is used to transmit power to and receive resistance temperature detector (RTD) signals from within the chamber. A quick access door with glass viewport (Kodial) is located at the top of the chamber for sample loading and optical reflectometry access. A N_2 carrier gas is passed through a flow meter and into a heated gas bubbler containing tetrahydrofuran via a polytetrafluoroethylene sparging head before entering the annealing chamber. The temperature of the bubbler was monitored *in situ* with a T-type thermocouple and was used to determine the vapour pressure of the THF vapour entering the annealing chamber. A PID controller is used to monitor and control the heating stage within the chamber. The surface topography of the BCP thin films, polymer molds on a silicon nanostructures were imaged by atomic force microscope using a Veeco Dimension 3100 in tapping mode. Liquid AFM imaging was performed using two instruments, a Bruker Multimode AFM equipped with a Veeco flow cell and an Asylum research MFP-3D AFM. Field emission scanning electron microscopy (FESEM, Carl Zeiss Ultra) using a secondary electron detector (in lens) at an accelerating voltage of 5 eV was used to show template morphology that formed during solvent annealing. Deionised water (<18 M) was obtained from a Milli-Q system from Millipore, Ireland. Ellipsometry was carried out in an open environment at room temperature on an M-2000UI ellipsometer (J.A. Woolam Co Inc.).

Dynamic contact angle analysis and surface energy measurements was obtained using a data-physics OCA tool and images were processed post measurement using ImageJ and the drop-snake plugin to obtain accurate contact angle measurements. ATR measurements wear obtained using a Perkin Elmer Spectrum GX FTIR used in the horizontal attenuated total reflection (HATR) mode (equipped with a ZnSe crystal, Perkin Elmer). Both chambers (detector and sample) were filled with nitrogen during measurements. SIMS measurements were obtained using a Scientific Analysis Instruments MiniSims tool with primary ion bombardment from a Gallium beam at 6 eV. Plasma experiments were performed using a Plasmalab System 100 plasma enhance chemical vapour deposition (PECVD) reactor (Oxford Instruments).

UV/ozone (UVO) treatment was carried out on a Novascan PSD-UV bench top cleaner. Spin coating was performed using a specialty coating systems 6800 spin coater series. XPS analysis was carried out using a VG Microtech electron spectrometer at a base pressure of 1×10^{-9} mbar. Photoelectrons were excited with a conventional Mg Kα ($h\nu = 1253.6$ eV) x-ray source and an electron energy analyser operating at 20 eV pass energy, yielding an overall resolution of 1.2 eV. All curve fitting analysis presented in this study was performed using AAnalyzer curve fitting software program version 1.20. All Si 2p spectra were fitted with Voigt doublet profiles composed of Gaussian and Lorentzian line shapes with a Lorentzian value of 0.40 eV. All O 1s and C 1s spectra were fitted with Voigt profiles with Lorentzian values of 0.55 eV and 0.40 eV, respectively. Film thickness calculations were performed using the NIST EAL database program version 1.3.

3.3 Methods

PS – *b* – P4VP ordered films: The PS – *b* – P4VP copolymer was dissolved in a toluene/tetrahydrofuran solvent mixture (80/20, w/w) by stirring overnight at room temperature to yield a 0.3 wt. % polymer solution. Silicon substrates were cleaved into 2cm by 2cm coupons and sonicated in acetone for 30 minutes and toluene for 30 minutes before being cleaned in piranha solution (hydrogen peroxide in sulfuric acid, 30/70 v/v) at 80 ºC. After cleaning the surface was functionalised with a 5 wt. % (ethylene glycol in ethanol) brush layer by spin-coating at 3000 rpm for 30 s and dried in the ambient for 30 minutes. Following this PS – *b* – P4VP BCP solution was spin-coated onto silicon substrates at 3000 rpm for 30 s. Samples were placed in either a jar for oven annealing or in the solvent thermal annealing chamber. Oven annealing was carried out for 5 hr at 50 ºC. After completion of the solvent vapour annealing process, the jar was removed from the oven, the lid was taken off the jar and after 1 min when the sample temperature dropped, the coupon can be taken out of the jar. After solvent vapour annealing process was completed in the chamber, the chamber was purged with N_2 to quench the BCP film. Before imaging the PS-b-P4VP films were immersed in ethanol for 20 min to selectively swell the P4VP block.

Solvothermal Annealing Chamber Process: Spin coated BCP films were placed into the chamber and exposed to THF vapour in N_2 carrier gas for 0.25-2 h to induce mobility and allow microphase separation to occur. To control the solvent vapour treatment process, the samples were annealed at a range of temperature with the vapour saturated with solvent (bubbled through a gas bubbler). The concentration of solvent in the chamber was used at fixed flow rate of 60 mUmin. Solvent was removed from the film by passing pure nitrogen through the chamber for 40 min.

Iron Nitrate Inclusion*:* PS-b-P4VP films are reconstructed with ethanol to selectively swell the P4VP cores. A solution of iron nitrate at a concentration of 0.5 wt% was spin-coated on top of the BCP film at 3000 rpm for 30s. The coupon was then treated with UV/O_3 for 3 hr. During this time, the PS matrix was degraded and the nitrate is converted to the oxide, resulting in the formation of iron oxide nanodots.

Homopolymer films: homopolymer solutions were prepared by dissolving polystyrene in toluene and P4VP in chloroform and stirring for 2 hr. The concentration of the solution determined the thickness of the homopolymer film. Silicon substrates were cleaned in piranha solution (hydrogen peroxide in sulfuric acid, 30/70 v/v) and the surface was coated with homopolymer by spin coating the solution onto the silicon at 3000 rpm for 30 s. After spin coating, the silicon coupons were placed in an oven at 60°C for 2 hr. This bake ensured that any remaining solvent was removed from the films.

Plasma etch experiments*:* Coupons were loaded into the loading chamber and the chamber evacuated to vacuum. The specific plasma recipe was entered into the plasma system. Samples were carried into the etch chamber using a robotic arm after which the plasma process were run. Post processing sample was removed using the robotic arm into the loading chamber, which was then vented to atmosphere so samples can be unloaded.

Ellipsometry measurements*:* ellipsometry models were optimised in-house for PS and P4VP. The models were checked against films that were measured using AFM. This was done by creating a trench in the surface. Using AFM, the height of the trench could be measured, which was equal to the film thickness. Film measurements were recorded three times across the coupon. An average of the three measurements recorded gave the film thickness.

Water Contact Angle*:* Dynamic contact angle was determined by recording the contact angle when a water droplet was advancing across the surface. Three measurements were made across the surface. Images were processed using ImageJ and the dropsnake plugin to obtain an accurate measurement. The average of all measurements gave the water contact angle of the sample.

Surface Energy: To determine surface energy of polymer thin films using the Owens, Wendt, Rabel and Kaelble (OWRK) method, two contact angles of two liquids with known disperse and polar parts were obtained. The advancing contact angle using water and diiodomethane was determined using the method described above. The two contact angles were then used to determine surface energy by solving the equation (3.1), the OWRK method surface free energy equation.

$$\sigma_{sl} = \sigma_s + \sigma_l - 2\left(\sqrt{\sigma_s^D \cdot \sigma_l^D} + \sqrt{\sigma_s^P \cdot \sigma_l^P}\right) \tag{3.1}$$

PPGDA and PEGDA preparation: 0.1% photo initiator (w/v) was placed in a glass vile and dissolved with 2-3 drops of acetone. To this solution either PPGDA or PEGDA was added and vortexed to ensure a homogenous solution was generated. The vile was covered in tinfoil to avoid curing by UV light. The solution was degassed to removed bubble and acetone from the solution. This was done by placing the vial into a desiccator and pulling a vacuum for 30min.

Cicada wing preparation: Using a clean scissors, the wing was cut into appropriate size and placed into a beaker of DI H_2O which was sonicated for 30min to remove debris from the wing. Following this the wing was dried under a stream of nitrogen.

Replica molding: PDMS and elastomer curing agent solution was mixed at a ratio of 15:1, the solution was degassed to remove bubbles by placing the vile into a desiccator and pulling a vacuum for 30min. the PDMS solution was poured into a petri dish until a small layer (<1cm) covered the bottom of the dish. The clean cicada wing was carefully placed on top of the uncured PDMS ensuring the wing did not sink deep into the PDMS or the sides of the wing were covered. The petri dish was placed in an oven at 70°C for 1 hr to cure the PDMS. Upon completion, the wing showed strong adhering to the dish due to the PDMS. PPGDA was used to mold the wing by places a small drop of the polymer solution on top on the wing. Under an oxygen free environment in a nitrogen glove box, the dish was placed under long wave UV light at a distance of 8cm from the lamp for 1 hr. After which the dish was removed from the glove box and the PPGDA primary mold removed from the wing carefully using a sharp tweezers. See Figure 3.1. The process was repeated using PEGDA as the molding polymer and the PPGDA primary mold as the master to fabricate a secondary mold.

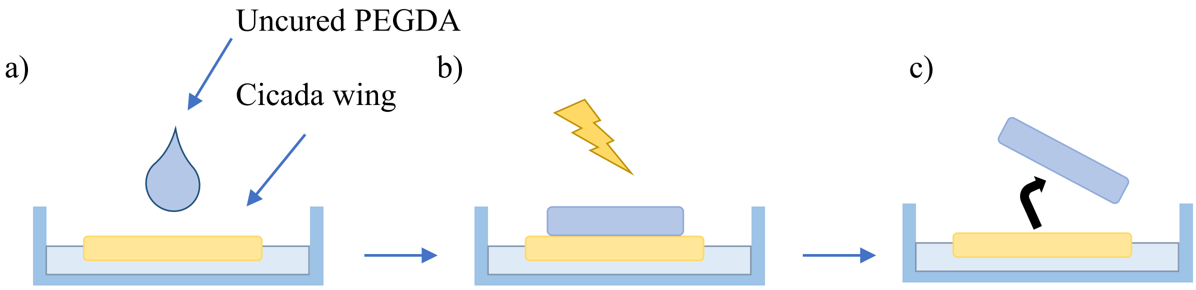

Figure 3.1 *Schematic of replica molding process. a) the master mold (cicada wing or primary mold) is adhered to the petri dish by imbedding in PDMS. PPGDA or PEGDA is poured onto the master mold surface. b) the dish is exposed to long wave UV light for 1hr. c) the mold is removed from the master using tweezers.*

PS – *b* – PMMA ordered films: The PS – *b* – PMMA copolymer was dissolved in toluene solvent by stirring overnight at room temperature to yield a 1 wt. % polymer solution. Silicon substrates were cleaved into 2cm by 2cm coupons and sonicated in acetone for 30mins and toluene for 30 mins before being cleaned in piranha solution (hydrogen peroxide in sulfuric acid, 30/70 v/v) at 80 ºC. After cleaning the substrate were neutralised with the brush of interest. PS – r – PMMA was prepared was dissolved in toluene solvent by stirring overnight at room temperature, followed by annealing on a hotplate for 5min at 220 ºC. The neutralised substrates were rinsed with toluene to produce brush layer of ~6nm. Following this, the BCP solution was spin-coated onto silicon substrates at 3000 rpm for 30 s. BCP were subsequently annealed on a hot plate for 10mins at 190 ºC.

Antibacterial testing:

Table 3.1 *Media and solutions*

Name	Composition
***E. coli* SM2029**	*ara, (lac-pro), thi attb:bla-Pa1/04/03-gfp**-T0/ pOX38km traD411
LB-Medium	5 g/L meat extract, 10 g/L tryptone, 10 g/L NaCl, pH 7
BF-Medium	1 mM $MgCl_2$, 0,1 mM $CaCl_2$, 3,7 mg/L Fe-EDTA, 1 µM Propidium Iodide After autoclaving: 10 % A10, 1 mM Glucose, 1 µg/mL Thiamine, 10 µg/mL Proline
A10	20 g/L $(NH_4)_2SO_4$, 60 g/L $Na_2HPO_4 \cdot 2\ H_2O$, 30 g/L KH_2PO_4, 30 g/L NaCl
Kanamycin solution	50 mg/mL Kanamycin sulphate dissolved indH_2O; sterile filtrated
PBS	9 g/L NaCl, 0,98 g/L Na2HPO4, 0,16 g/L KH2PO4, pH 7,4

Samples were adhered to a support using silicon glue. The sample was sterilized with UV-light and ethanol and then attached to a sterile petri dish using sterile glue.

Pre-culture was prepared by the following:

1. 20 mL LB-Medium incl. 50 µg/mL Kanamycin (add 20 µL the stock solution)
2. thaw cryo culture, centrifuge for 5 min at 5000 rpm at RT; resuspended pellet in 250 µL fresh LB medium
3. add 200 µL of resuspended *E. coli* cryo culture (OD_{600} ca. 0.1) to the 20 mL Medium
4. Incubate for 4-5 h at 30 °C and 250 RPM

Biofilm Medium was prepared by the following:

Table 3.2 *Composition of Biofilm-Medium*

Stock Solution (concentration)	Final concentration	for 2L	for 1L	for 0.5 L
dH_2O	-	1800 mL	900 mL	450 mL
1 M $MgCl_2$ in dH_2O (sterile filtrated)	1 mM	2 mL	1 mL	500 µL
1 M $CaCl_2$ in dH_2O (sterile filtrated)	0.1 mM	200 µL	100 µL	50 µL
10.000 x Fe-EDTA in dH_2O (sterile filtrated)	3.7 mg/L	200 µL	100 µL	50 µL
A10	1/10	200 mL	100 mL	50 mL
1 M Glucose in dH_2O (sterile filtrated)	1 mM	2 mL	1 mL	500 µL
1 mg/ml Thiamine in dH_2O (sterile filtrated)	1 µg/mL	200 µL	100 µL	50 µL
10 mg/ml Proline in dH_2O (sterile filtrated)	10 µg/mL	200 µL	100 µL	50 µL

Table 3.3 *Composition of A10*

Components	1 L	0,2 L
$(NH_4)_2SO_4$	20 g	4 g
Na_2HPO_4 x 2 H_2O	60 g	12 g
KH_2PO_4	30 g	6 g
$NaCl_2$	30 g	6 g

Inoculation was carried out by measuring measure OD (optical density) of the cell suspension (solution should have around OD_{600} = 1,5). The cell solution was filtered through a 5 µm filter to separate cell agglomerates. OD of filtrate was recorded. Cell concentration was calculated using: N[1/mL] = OD_{600} x 6,3 x 10^8 cfu/mL. Cell solution was diluted by1 x 10^8 cfu/mL (BF-Medium). 8 mL of the diluted cell suspension to each petri dish and incubated for 30 min at 30°C. Washing steps were performed in triplicate and done by slowly adding 8 mL cell-free Medium into petri dish and removing the suspension. Microscopic analysis was carried out using at least 10 images of each sample ensuring equal light intensity and illumination time for each image.

Chapter Four

4 The optimisation of solvothermal annealing of PS – b – P4VP BCP thin film

4.1 Introduction

As mentioned in chapter one, semiconductor feature size continues to shrink, driven by the increasing demand for high speed and low energy consumption computation by the semiconductor industry, the physical limit of patterning technologies is fast forthcoming. Limitations involved with the state-of-the-art lithography methods; such as huge cost and output power has led to new patterning strategies being explored and BCPs are among the methods considered as a potential solution for fabrication of sub-14 nm nodes. High χ BCP systems, such as poly(styrene)-*block*-poly(4vinylpyridine) (PS – b – P4VP) are desirable for obtaining good microphase separation with small interfacial widths for minimal line edge roughness and small microdomain size. The χ value for PS – b – P4VP is estimated to be $\chi_{\text{S-4VP}} = 0.56$ at $T = 298K$).[109-112] High χ BCP systems are vital for obtaining sub 10nm features. For this reason, cylindrical forming PS – b – P4VP was chosen as the BCP system to be used to fabricate self-assembled hexagonal arrays in the work.

However, such systems possess low block retraction diffusivity ($D \sim e^{-\chi N_A}$) leading to long thermal annealing times where the maximum annealing temperature is limited by polymer decomposition.[113] Solvent vapour annealing is an attractive alternative annealing approach, as solvent absorption into the polymer film significantly improves the kinetic pathway for phase segregation by plasticizing the polymeric blocks *via* a reduction in the effective interaction parameter ($\chi_{\text{eff}} < \chi$).[114] A advantage of this process is the significantly reduced annealing times in comparison to thermal annealing, since the order-disorder transition is often above the polymer degradation temperature for high-χ polymer systems. The conventional method for solvent annealing BCPs is shown in Figure 4.1. In this process, the sample is placed inside a jar along with a reservoir of solvent. Over long annealing times the atmosphere becomes saturated with solvent vapour and microphase separation occurs. This method is widely used to prepared microphased BCP films.[115, 116] However, this process hinders reproducibility and the lack of control over solvent temperature, solvent vapour pressure, sample temperature and ultimately the removal of the solvent from the film is a massive limitation.

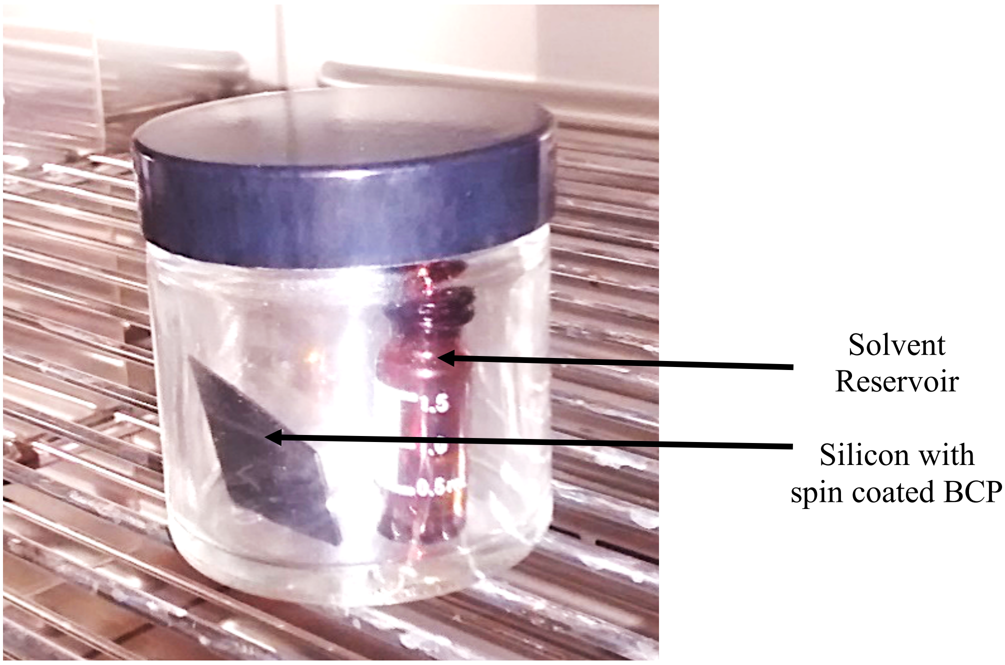

Figure 4.1 *Conventional solvent vapour annealing using a solvent reservoir inside a jar; the sample is placed beside the vial and the jar placed in an oven at the appropriate temperature.*

The biggest concern about this process is the lack of long range ordering due to a dewetting issue that occurs during annealing, see Figure 4.2. Dewetting is condensation of the solvent on the surface of the substrate which results in delamination of BCP films leading to unpatterned regions. Polymer dewetting can arise from two general mechanisms; bulk solvent condensation leading to polymer dissolution [117] and film rupture driven dewetting in the presence of solvent vapour.[118] Bulk condensation of the solvent vapour onto the polymer film occurs when the solvent vapour, $P_v(T_{sat})$, is at a higher pressure than the corresponding saturated solvent pressure of the polymer surface at temperature T_{sub} resulting in supersaturation (4.1). [119, 120]

$$S = P_v(T_{sat})/P_v(T_{sub}) > 1 \tag{4.1}$$

Thermodynamically-driven film rupture occurs during solvent annealing where the BCP is brought towards an equilibrium structure and solvent swelling can allow the substrate-polymer interface to move into a thermodynamically more favourable morphology that differs from the as-deposited film structure. For thin films (<100nm) the long-range van der Waals repulsion and a short-range attraction can result in hole nucleation and spinodal dewetting,[120] that produces droplets through the growth of uniformly distributed surface undulations.[121] Thus, dewetting can be a significant issue, affecting the final film morphology, and is dependent on the polymer/surface interactions, degree of swelling,[122] choice of solvent,[117] the anneal temperature and gas pressure.[118]

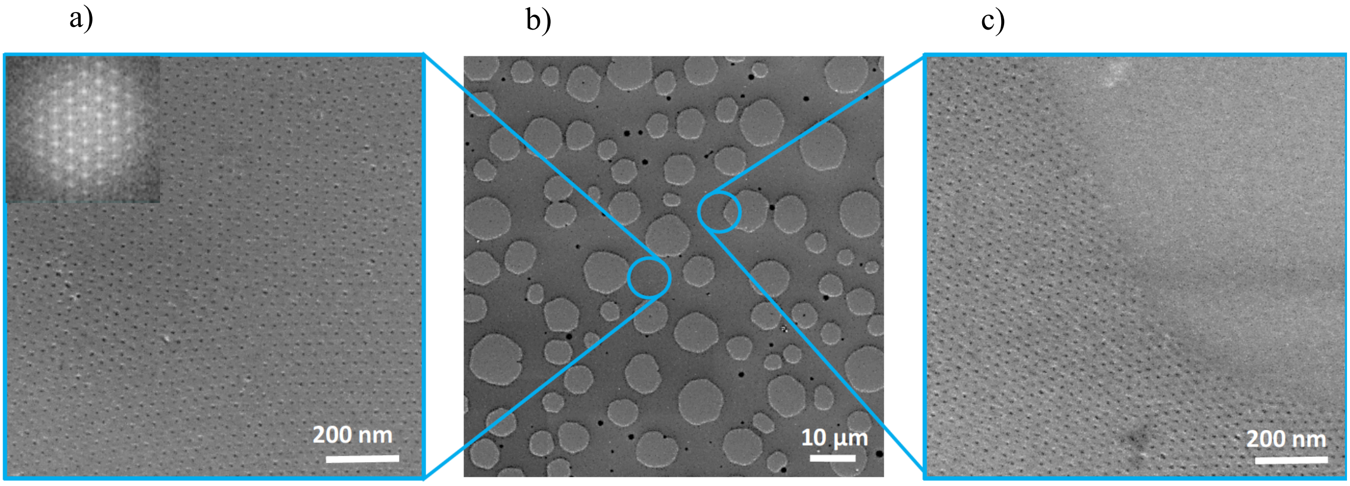

Figure 4.2 *a) PS – b – P4VP BCP that has been selectively reconstructed with ethanol to remove the P4VP cores. A FFT (fast Fourier transform) of the film is shown on the inset. A well-ordered hexagonal pattern is seen across the wafer. b) at the micron scale, large amounts of dewetting is observed due to the nucleation of solvent on the surface. c) Unpatterned areas caused by dewetting of films.*

To limit these drawbacks and to provide a highly controllable system, solvent annealing chambers have been explored. Park et al. have designed and optimised a solvent annealing system to produce perpendicular aligned PS – *b* – P4VP arrays. In this system, spin-coated BCP films were exposed to THF solvent which was carried into the annealing chamber by a N_2 gas. The temperature was kept constant at 23 ºC and annealing times varied from 30 minutes to 4 hours. To characterise their surfaces

AFM in tapping mode and grazing incidence small-angle X-ray scattering (GISAXS) was used. Their work demonstrated large range ordering enhanced by increasing annealing times in their controllable annealing process.[123]

Similarly, colleagues from the Ross Research group at Massachusetts Institute of Technology have investigated a range of solvents in a chamber system to produce hexagonal ordered arrays of BCPs. Their solvent annealing chamber incorporated a reflectometer to allow for *in situ* film thickness measurements; which demonstrated the swelling of the films during initial solvent uptake. Using SEM to characterise their films, they found by heating the films after the swelling process, well-ordered morphologies were produced in extremely short annealing times of 30 seconds to 4 minutes. [44, 124, 125]

From the work carried out by Park et al. and Ross et al., it is evident the importance of using a controllable annealing system to produce long-range ordered morphologies. Using this work as motivation, a new annealing process for PS – *b* – P4VP using a custom-built chamber was investigated. The experimental agenda is outlined in the schematic in Figure 4.3.

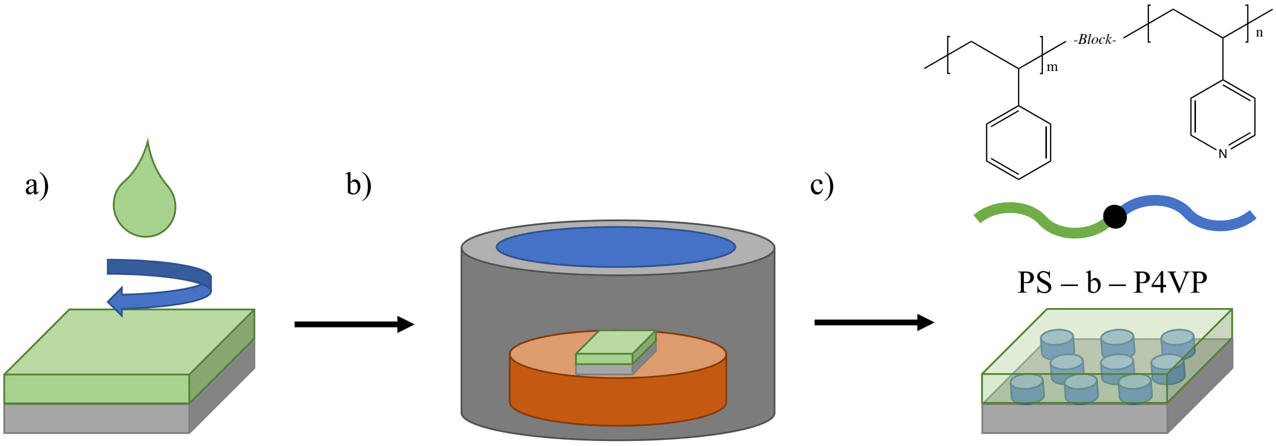

Figure 4.3 *a) PS – b – P4VP solution is spin-coated on top of neutralised silicon surfaces b) dynamic solvent annealing of PS – b – P4VP under THF solvent vapour in a custom-built solvent annealing chamber c) microphased PS – b – P4VP thin films are generated with perpendicular orientated P4VP cores imbedded in a PS matrix.*

A solvothermal annealing chamber was designed by collaborators, Dr Ross Lundy and Dr Ryan Enright, to create a highly controllable process. Moreover, previous annealing chambers discussed are typically implemented for small scale processing and the use of this technique to achieve rapid pattern formation while avoiding polymer dewetting over wafer-scale areas has not been demonstrated.

A schematic of the chamber can be seen in Figure 4.4. Capable of processing up to 4 inch wafers the chamber also allows for light transmission through a borosilicate glass viewport. Although not yet implemented, this viewport could be used for *in situ* reflectometry measurements. A nitrogen carrier gas stream, controlled by a flow meter, is introduced into a temperature controlled solvent bubbler. The solvent saturated nitrogen carrier gas stream then flows through a sealed steel chamber containing the BCP film, which is heated on an annealing stage using a proportional–integral–derivative (PID) controller. On completion of the solvent annealing cycle the gas bubbler line is by-passed to allow pure nitrogen to flow through the chamber for a controlled removal of the solvent from the BCP film. This chamber provides complete control over solvent temperature, sample temperature and solvent flow. By annealing under a dynamic solvent flow and heating the substrate slightly above the solvent saturation temperature, solvent condensation and therefore dewetting can be avoided.

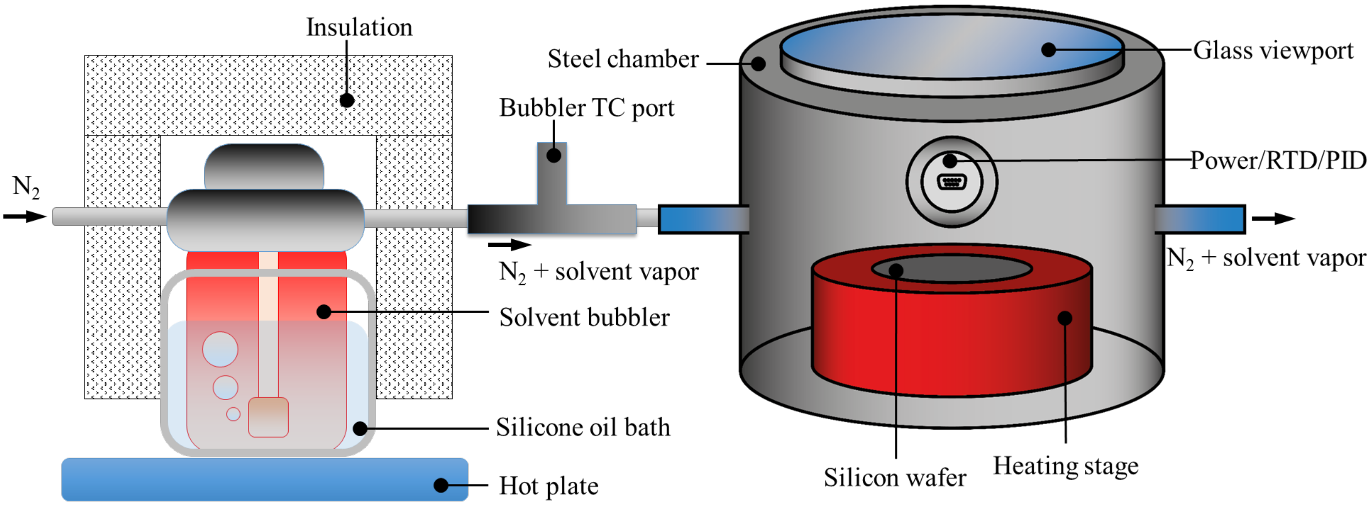

***Figure 4.4** Schematic representation of the solvothermal annealing chamber.*

4.2 Results and Discussion

Given that the set-up of this solvothermal annealing chamber was completely novel, a range of conditions for block copolymer annealing were investigated to generate ordered films with apparent microphase separation. Since GISAXS characterisation is not available in our laboratory; BCP films must be characterised using SEM and AFM. It is important to consider what is the optimal film morphology. Figure 4.5 shows cartoon of an optimal a) and poor b) microphased cylindrical PS – *b* –P4VP system.

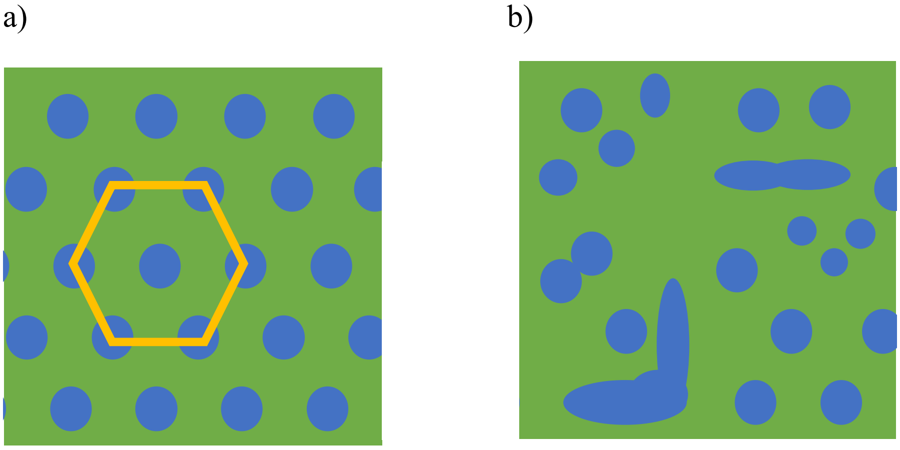

Figure 4.5 *a) Shows a cartoon representation of the optimal phase separation of PS – b –P4VP. The film is hexagonally ordered (shown by the yellow hexagon). b) Shows a cartoon of a poorly phase separated film with micelle-like structures and inconsistent core sizes.*

The optimal phase separation to be achieved (Figure 4.5 a)) has P4VP cores of equal diameter and pitch arranged in a hexagonal array (shown by the yellow hexagon). Poor phase separation (Figure 4.5 b)) contains pores with different diameter, pores that have joined and micelle features. During annealing, when transition to a disordered state is incomplete; a range of micelle morphologies such as slightly elliptic, rod-like and vesicle will result.[126] Such features are characteristic of insufficient block diffusion at low BCP film swelling ratios with values for supersaturation ($S \leq 91$). It is important to obtain S values closest to 1 as the order-disorder transition occurs when $S \approx 0.99$ for the range of annealing temperatures explored. Moreover, annealing at S values greater that 0.96 is expected to result in rapid phase separation.[112]

An initial set of anneals were carried out; PS – *b* –P4VP films were spin-coated onto neutralised silicon substrates and placed in the solvothermal anneal chamber between temperatures of 21°C, 30°C and 40°C at 15, 30, 60 and 120 min intervals under a dynamic THF solvent vapour flow. Figure 4.6 shows a matrix of SEM micrographs of annealed films.

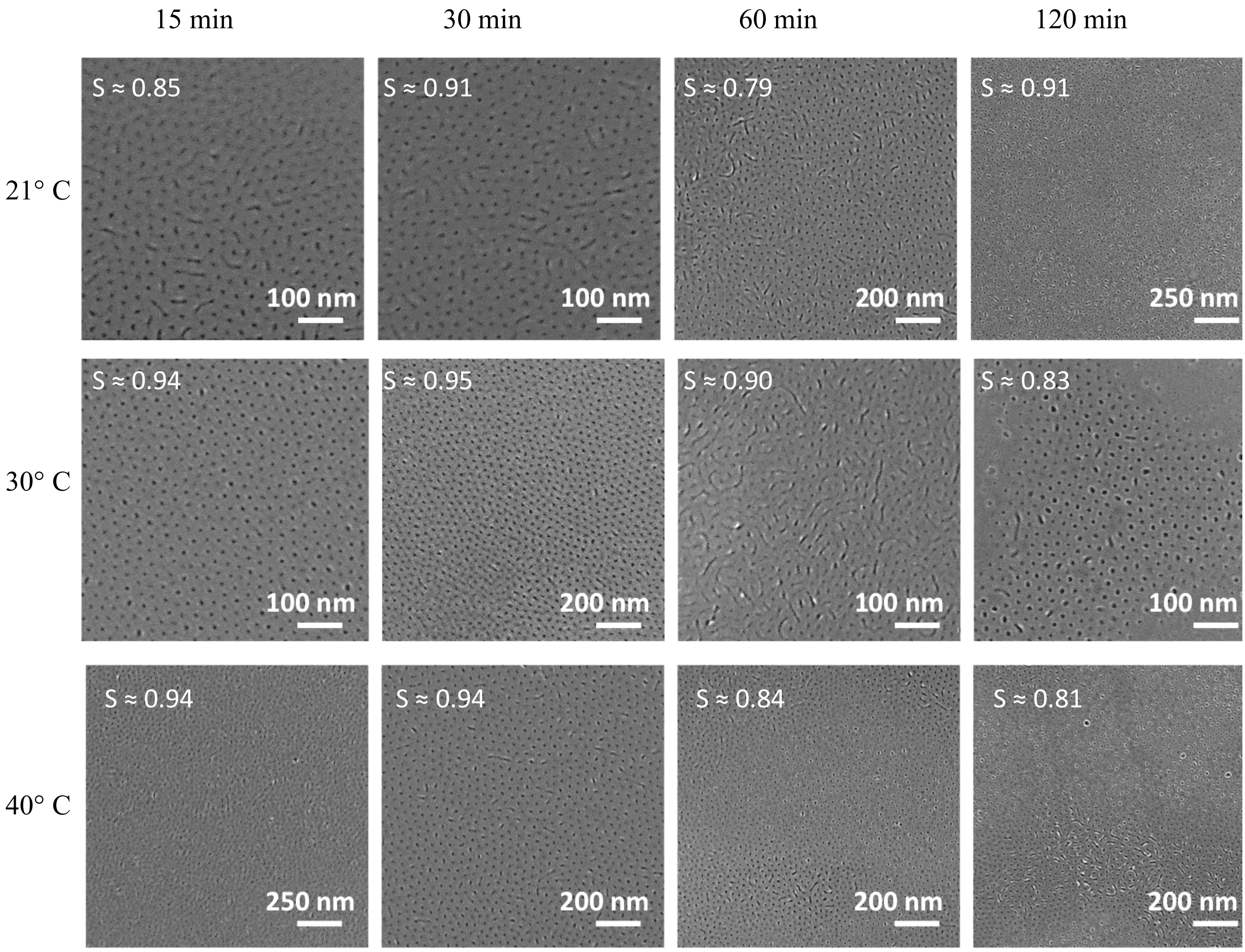

Figure 4.6 *SEM Micrographs of PS-b-P4VP annealed films at 25℃, 30℃ and 35℃ at 30, 33, 36 and 39 min. Films were reconstructed with ethanol before imaging. Supersaturation values reached for each anneal are given in the top left inset of each image.*

To obtain a topographic surface needed for SEM characterisation, the BCP thin films were reconstructed by soaking in ethanol for 20 min. Although the exact mechanism is still under debate, this ‘reconstruction’ process is thought to selectively swell the P4VP core, causing it to collapse, creating pore structures.[127] The supersaturation for each anneal was calculated and is displayed in the top left inset of each SEM image. Since nitrogen flowrate of 120 ml/min was used, it takes ~ 15 minutes for $P_v(T_{sat})$ to reach its maximum pressure within the chamber (internal chamber volume 1.9 L). Therefore, calculating the supersaturation is more accurately based on the temperatures at the end of the anneal. For example, the anneal at 30°C at 30 minutes had temperatures of T_{sat} = 30.4 °C and T_{sub} = 31.3 °C for the bubbler and annealing stage respectively at the end of the anneal. From the Antoine equation (4.2), where P is the pressure in mmHg, T is temperature in °C and the parameters A = 6.99515, B = 1202.29 and C = 226.254 are THF component-specific constants and were taken from Dortmund Data Bank. Using these values to calculate THF partial pressures of T_{sub} = 28.31 and T_{sat} = 26.81, giving a value for S = 0.947.

$$P = 10^{A-\frac{B}{C+T}} \tag{4.2}$$

From the SEM characterisation in Figure 4.6, it was evident that anneals at 21°C for 15 min – 2 hours resulted in morphologies that were predominately micelle-like, which corresponded to insufficient block diffusion at low BCP film swelling ratios. The S values obtained for these anneals correlate to the features seen. Anneals carried out at 30°C at 15 minute and 30 minute showed the desirable morphology of perpendicular aligned P4VP cylinders; with higher S values calculated. However, at 60 and 120 minute the films had transitioned into micelle like features again with some parallel cylinder features seen (rod-like structures). Anneals at 40°C showed a variety of morphologies, mostly consisting of perpendicular and parallel aligned features, with the longer times being micelle-like. The key information from this initial set of anneals was that annealing times between 15 minute and 30 minute at 30°C generate morphologies of interest. These films look similar to Figure 4.5 a) with perpendicular oriented cores of near equal diameter and pitch. More importantly, it has been shown that annealing at conditions which generate the supersaturation values closest to 1 results obtain patterns of interest. This was achieved by setting the substrate temperate slightly higher than the solvent temperature, but keeping this difference at a minimum ($T_{sub} \approx T_{sat}$ + 1K). This was difficult as seen with the anneals in Figure 4.6. As annealing time is increased, the solvent temperature will decrease due to evaporation. For the substrate temperature, as annealing time is increased, the temperature increases due to the radiant heat from the chamber walls. For these reasons, controlling S values at long annealing times can be increasingly difficult.

The films were assessed to see if there was a presence of dewetting. This was done by repeated SEM analysis across samples. SEM images revealed that across the wafer, no dewetting was observed, see Figure 4.7. The colour difference seen in Figure 4.7 is a feature of different film thickness, not dewetting, as the area in these regions still has surface features.

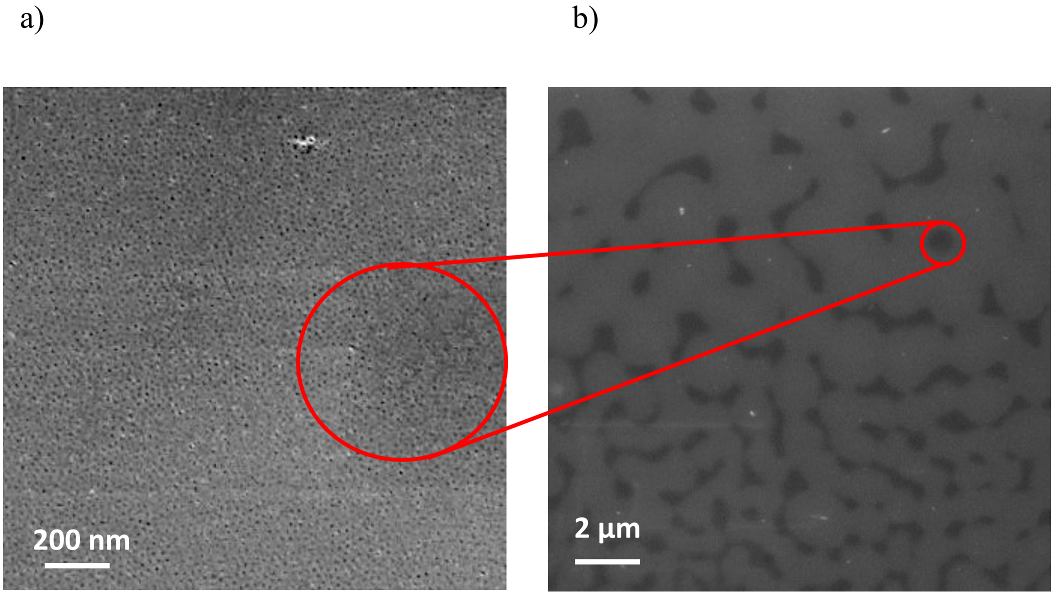

Figure 4.7 *SEM Micrographs showing large scale coverage of perpendicularly aligned cylinders with no dewetting across the wafer. a) and b) are the same sample imaged at different scales to show the eradication of dewetting. The difference in colour observed (marked by the red circle) is due to the difference in film thickness across the wafer which occurs during solvent annealing.*

Bulk condensation induced dewetting of the BCP template film was avoided in this process by implementing a PID-controlled annealing process in the chamber; this allowed sample temperature to be accurately controlled by the heating stage, ensuring that the local supersaturation of the film surface was kept below supersaturation.

Using the information learned from the initial set of anneals, another set was carried out to further optimise the solvothermal annealing process. During these experiments, the conditions were controlled to keep the difference between the solvent temperature and the substrate temperature to a minimum, which would result in high S values. From the experiments previously carried out, annealing at temperatures higher than 40°C and longer than 60 minutes has been shown to produce poor phase separated films, therefore shorter annealing times and lower temperature were examined. Anneals were carried out at 25°C, 30°C and 35°C at 18, 21, 24, 27, 30, 33, 36 and 39 minute intervals. SEM micrographs are shown below, see Figure 4.8.

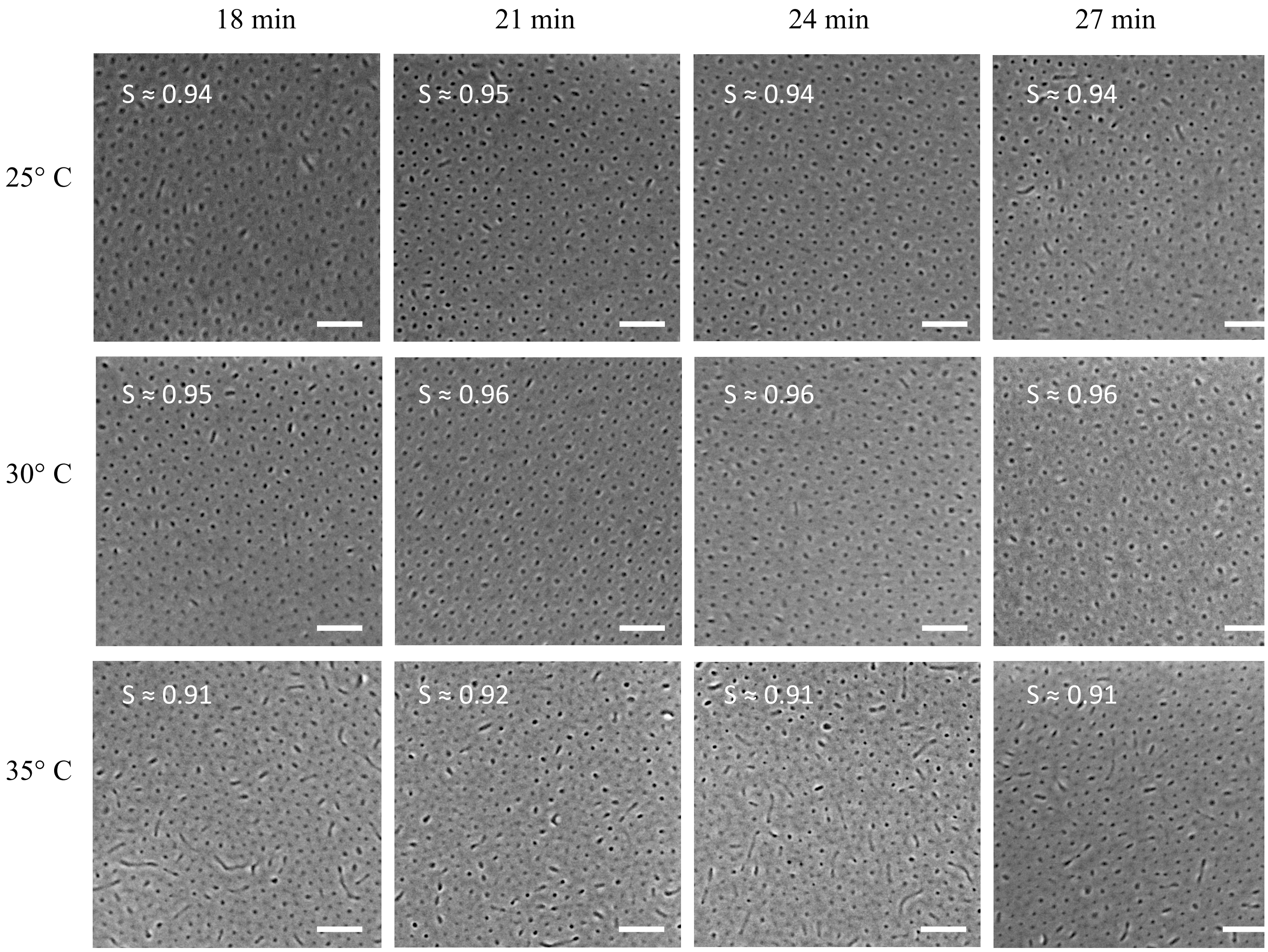

Figure 4.8 *SEM micrographs of PS – b – P4VP films that have been ethanol reconstructed. Supersaturation values reached for each anneal are given in the top left inset of each image. All scale bars are 100nm.*

The anneals at 25°C and 30°C between intervals of 18, 21, 24, 27 minutes showed morphologies of interest with perpendicularly aligned P4VP cylinders. S values calculated were between 0.94 and 0.96. Although some cylinders are seen to be joining, the overall phase separation appears to be acceptable with perpendicular aligned cylindrical features seen. The patterns annealed at 35 °C presented mixed morphologies with both parallel and perpendicularly aligned cylinders, indicating poor phase separation. The S values ranged between 0.91 and 0.92, which was expected with such features. As temperature is increased the difference between solvent temperature and substrate temperature become increasingly difficult to control, leading to lower S values.

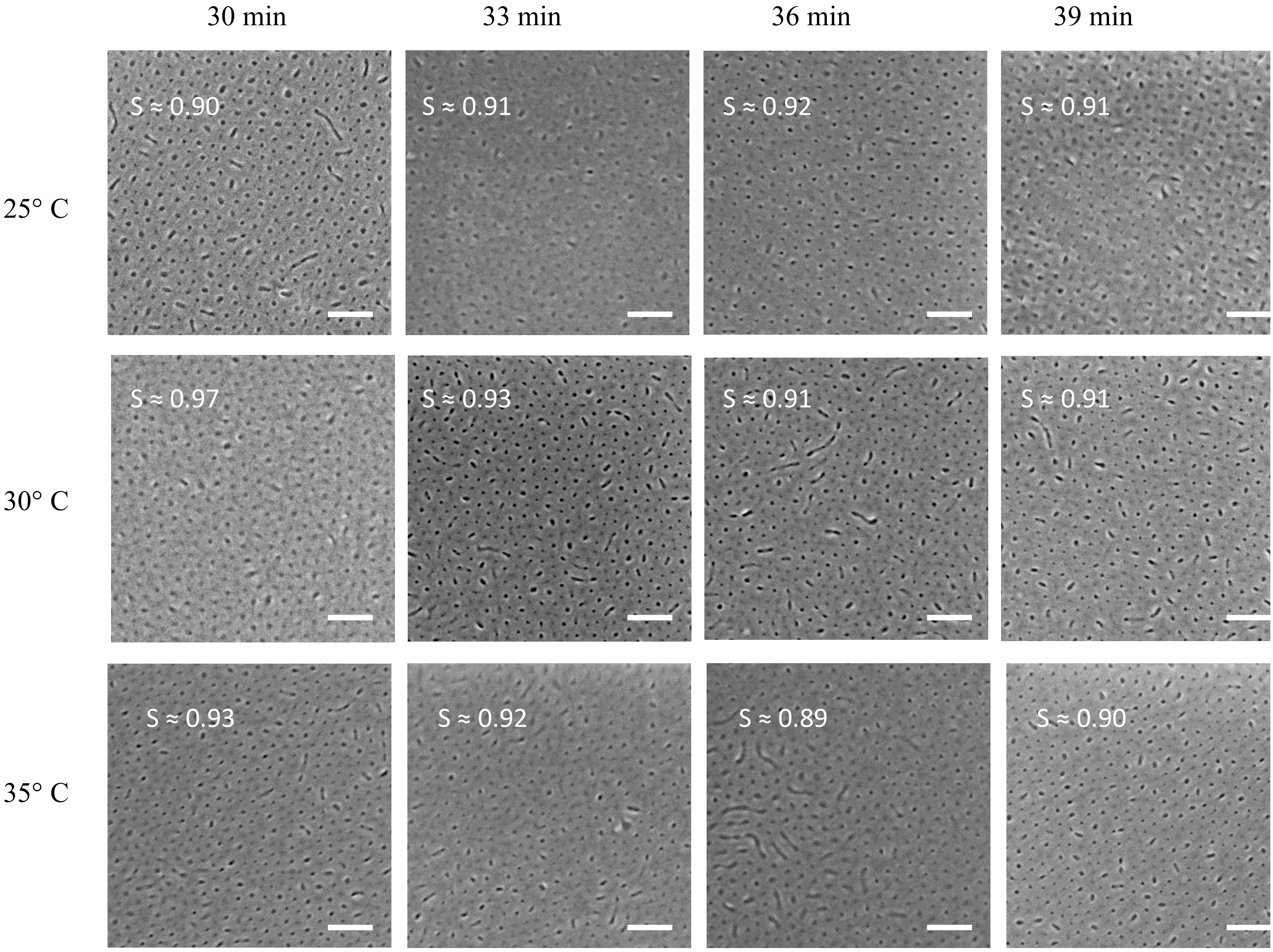

Figure 4.9 *FESEM micrographs of PS-b-P4VP films that have been ethanol reconstructed. Supersaturation values reached for each anneal are given in the top left inset of each image. All scale bars are 100nm.*

From Figure 4.9, films annealed for 30, 33, 36, 39 minutes at 25°C also displayed mixed morphologies. Such features are characteristic of insufficient block diffusion at low BCP film swelling ratios with low values for supersaturation as seen in previous experiments. From Figure 4.9, it is clear that the film annealed at 30°C for 30 minutes shows adequate phase separation with perpendicular aligned cylinders. The pores are clearly aligned perpendicular to the substrate and little defects are seen. For at 33, 36 and 39 minute intervals at 30°C the films resulted in undesirable morphologies. The pores have joined in places and micelle-like features are visible. S values are low ranging between 0.91 and 0.92. The intervals of 30-39 minutes at 35 °C presented mixed morphologies with both parallel and perpendicularly aligned cylinders. Controlling the substrate temperature at high temperature proved difficult due to the radiant heat from the chamber walls leading to low S values.

From this result, it was concluded that annealing films over 30°C and over 33 minutes do not generate well-ordered BCP arrays. While 30 minutes at 30 °C showed acceptable phase separation, as seen in the initial annealing experiments. From the SEM analysis, these parameters indicated optimal conditions to generate patterns of interest. Once more, samples were repeatedly imaged to determine if dewetting had occurred and samples were shown to be free of this defect. It must be noted that although perpendicular aligned cylinders of P4VP have been generated, perfect hexagonal ordering has not been achieved. It is thought this is attributed to the relatively slow quench step during the process. In contrast, the quench step carried out in static solvent annealing methods are fast as the sample is removed from the container into the ambient once the annealing time is reached. This suggests that the new solvothermal annealing process can be further optimised by varying the speed of solvent extraction from the film to improve the ordering. This hypothesis draws parallels with the work carried out by Gotrik et al. Their work demonstrated that quench time played an important role in achieving highly ordered films.[125]

Although the SEM characterisation carried out provided excellent information, there are merits to carrying out AFM characterisation also. This provided additional information for surface topography and phase separation. AFM analysis was carried out on ethanol reconstructed films. Representative height images are shown in Figure 4.10 and 4.11. Silicon AFM probes were used with a force constant of 40 N/m and a resonance frequency of 300 kHz in tapping mode. Each BCP had a thickness ranging between 18 – 21nm.

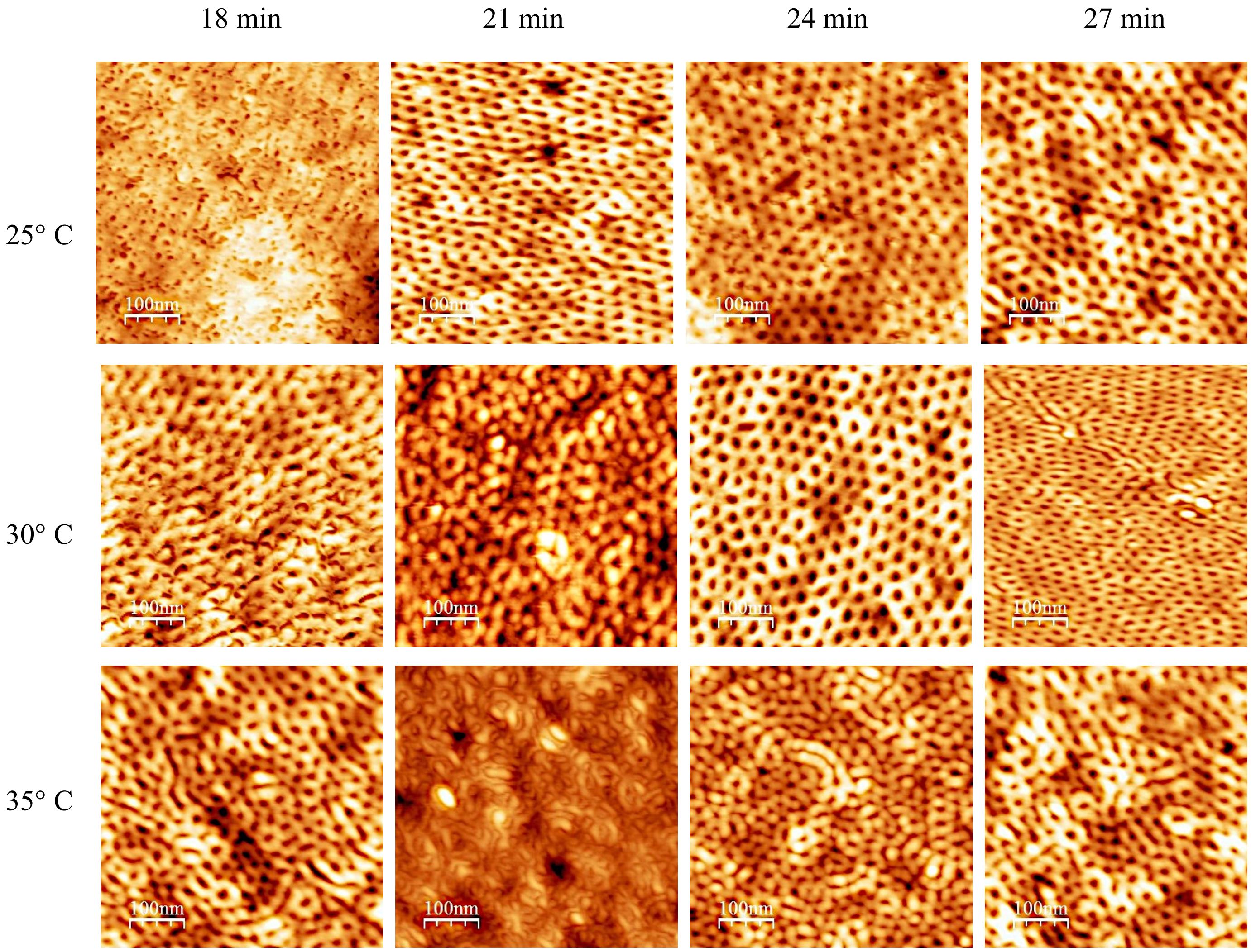

Figure 4.10 *Representative AFM images of PS – b – P4VP that has been ethanol reconstructed. All scale bars are 100nm.*

The AFM height images in Figure 4.10 support what was observed in the SEM characterisation, excluding the 18 minute, 25°C anneal. This AFM image revealed mixed morphologies and the perpendicular aligned P4VP cores seen in the SEM were not imaged using AFM, confirming that these conditions are not optimal. This shows that although features were seen in the SEM analysis, this was not the case for across the wafer as AFM revealed little adequate phase separation. For 21–27 minutes at 25°C the desired microphase separation showing perpendicular oriented cylinders was observed. For 30°C at 18 and 21 minute intervals, AFM analysis does not show clear core features. This could be due to the polymer material becoming damaged during imaging or the tip being contaminated with polymer material during imaging.

This again highlights the importance of doing both AFM and SEM analysis on BCP films to get a clear representation of the surface. Figure 4.11 shows representative AFM analysis for anneals carried out at 25°C, 30°C, 35°C at 30–39 minute intervals.

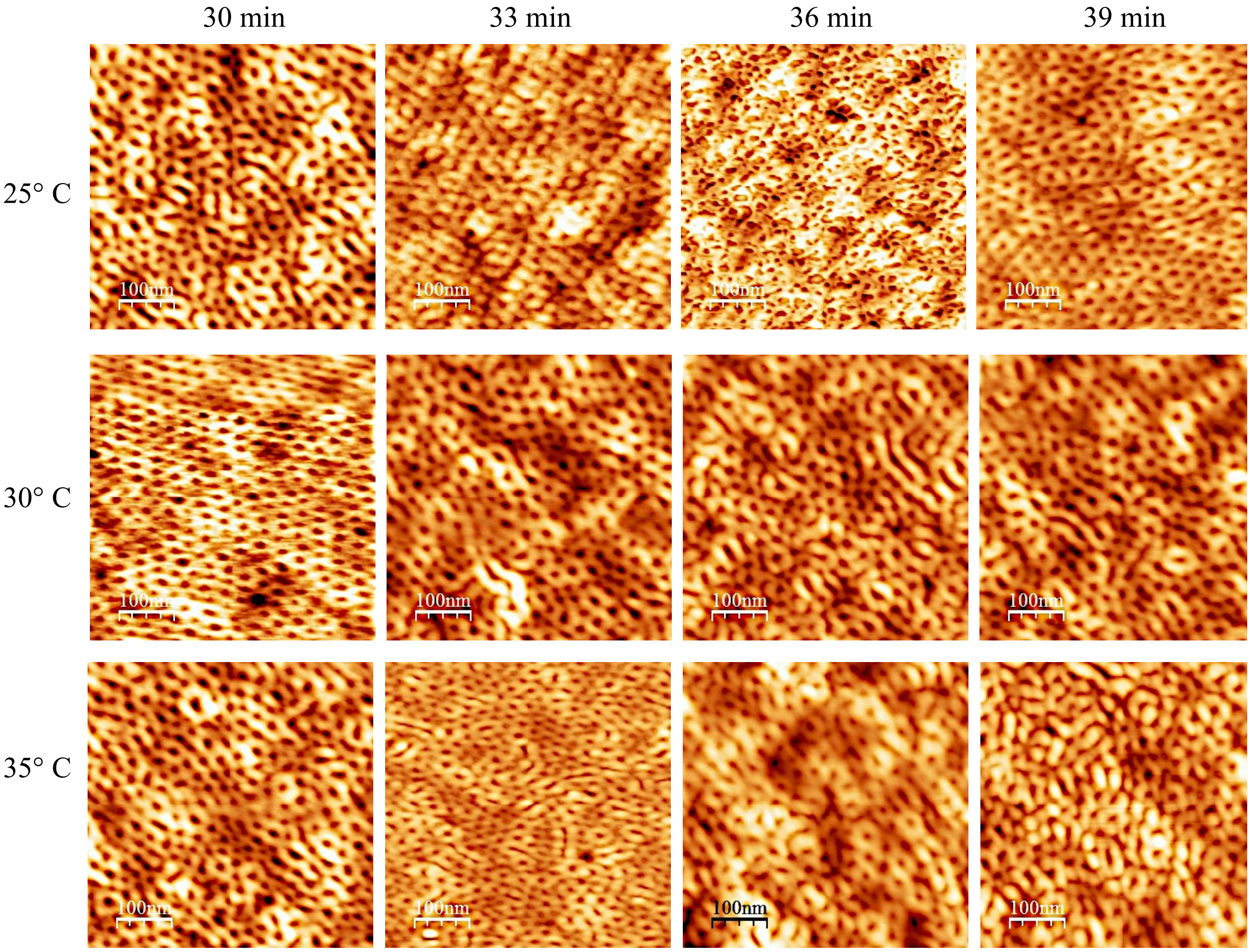

Figure 4.11 *Representative AFM images of PS-b-P4VP films that have been ethanol reconstructed. All scale bars are 100nm.*

For the films annealed at 25°C for 30, 33, 36, 39 minutes the AFM height images revealed what was observed in the SEM characterisation. The films displayed mixed morphologies with both perpendicular and parallel aligned features. For films annealed at 30°C for 33, 36, 39 minute intervals, the films appear to have better cylindrical morphologies that the 25°C counterparts, however parallel aligned cylinders represented as rod-like structures are seen, which correlate to the SEM characterisation. For 35°C at 30, 33, 36, 39 minute intervals similar structures are seen with a mix of morphologies. The AFM characterisation confirms what the SEM analysis determined; the anneal carried out at 30°C for 30 min had the optimal ordering and morphology. This cemented the results from the SEM analysis and confirmed annealing over 30 minutes was not optimal. WSxM solution software showed that the 30°C for 30 min anneal features had an average pitch of 25.5nm ± 2.4nm and an average diameter of 21.3nm ± 3nm, see Figure 4.12. These dimensions corroborate to the feature size of self-assembled of PS – *b* – P4VP reported in the literature. [46] The Z scale shown in Figure 4.12 b) is not a clear representation of the film thickness. The pores are too small for the tip to image inside, therefore the height appears smaller in AFM characterisation. The BCP film was measured with ellipsometry and was shown to be 21nm in thickness.

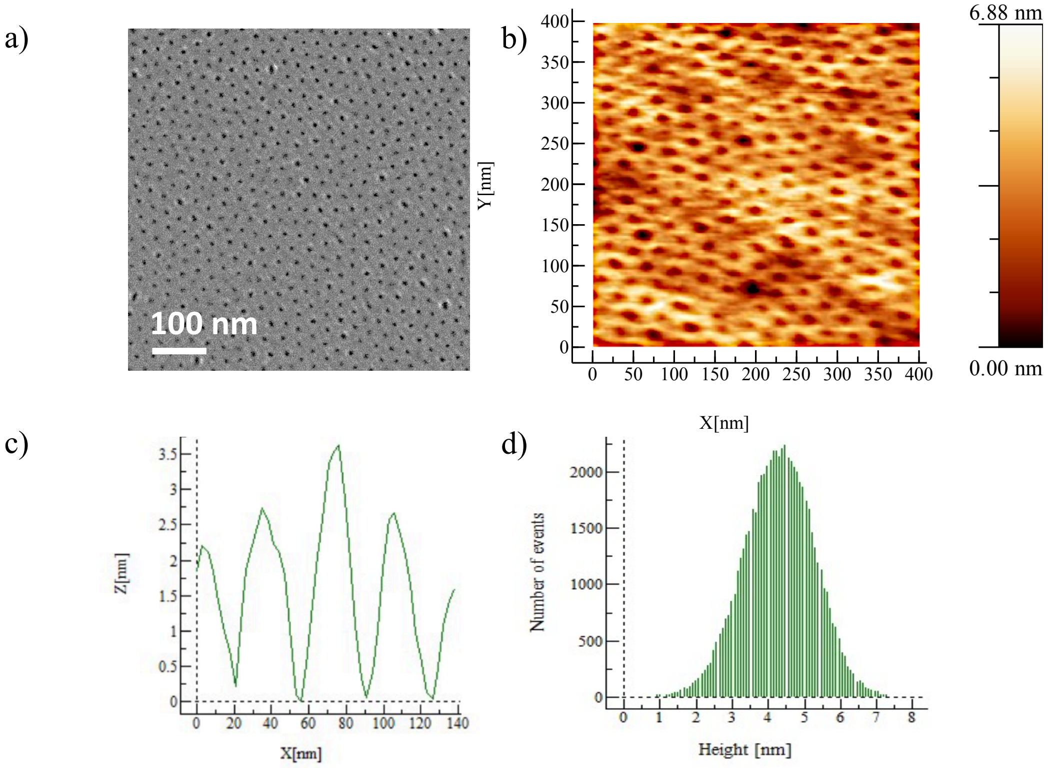

Figure 4.12 *a) SEM image of PS-b-P4VP film that has been annealed at 30℃ for 30 min. b) Representative AFM image of PS-b-P4VP film that has been annealed at 30℃ for 30 min. c) Cross-section profile of the film showing a pitch of 25.5nm ± 2.4nm and an average diameter of 21.3nm ± 3nm. d) AFM height histogram.*

This chamber which was set-up and optimised to produce microphased BCP films is comparable to the few chambers reported in the literature. The work carried out by Gotrik et al. and Park et al. show using controllable systems such as this to create highly order BCP films without defects is desired.[42, 123] Gotrik's work highlights the importance of using both solvent and temperature to create highly ordered films. In their research, the importance of solvent removal from the BCP films is also emphasised. From this work, it is believed our chamber can be further optimised by increasing the speed of the quench step. This could be further controlled by implementing a reflectometer to perform *in situ* film thickness measurements.

4.3 Conclusion

In this chapter, initial work that involved the set-up and optimisation of a state-of-the-art solvothermal annealing chamber has been presented. The objective to overcome the dewetting limitations associated with static annealing and develop a highly controllable process has been achieved. The results presented demonstrated the effective reproducibility of BCP films without polymer dewetting. A wide range of dynamic solvothermal annealing conditions have been investigated with 30°C for 30 minute anneal presenting desirable patterns with features of an average pitch of 25.5nm ± 2.4nm and an average diameter of 21.3nm ± 3nm. Bulk condensation was avoided by heating the substrate slightly higher than the solvent saturation temperature ($T_{\text{sub}} \approx T_{\text{sat}} + 1\text{K}$) and the saturation for this anneal was calculated to be $S = 0.96$.

It must be noted that the annealing conditions must be improved on, since well-ordered hexagonal arrays generated by static annealing have not be obtainable thus far using the chamber. However, it is believed this will be easily achieved with further optimisation of the quench protocol and implementing a reflectometer to perform *in situ* film thickness measurements. This would provide better control for the removal of the solvent from the film, which has been highlighted to be important in enhancing the BCP ordering.

4.4 Future Work

The aim to implement a highly controllable BCP process to generate reproducible BCP templates has been achieved in the chapter. The next step is to use these templates to pattern transfer into the silicon substrate. PS – *b* – P4VP must be converted into a hard mask material using an iron nitrate inclusion processes. This enables selective inclusion of the iron nitrate material into the P4VP cores. This can then be converted to iron oxide, a hard mask material which is etch resistant to a silicon dry etch. Ultimately the process will enable the fabrication of silicon nanopillar arrays. These investigations are discussed in chapter seven.

Chapter Five

5 Selective etching of block copolymers using plasma

5.1 Introduction

As new patterning techniques begin to emerge, the ease of integrating these new methods into the nanofabrication industry is essential to consider. This is one of the strongest advantages of BCP self-assembly; the tools needed to prepare such are already implemented in industrial processes lines. Although BCP are valuable for creating a nanopattern, the polymer materials normally don't have the etch contrast to be used as a mask alone. Several methods to transform BCP templates to hard marks have been investigated. As mentioned previously, ethanol activated BCPs can be transformed into hardmask materials through a metal salt inclusion process.[46, 47, 128]

For PS – *b* – P4VP hard mask fabrication is commonly done by selective 'activation' of the P4VP block.[127, 129] This is predominantly achieved by an 'ethanol reconstruction', which involves immersing the samples in ethanol to selectively swell the P4VP cores.[112, 130] The limitation associated with the method is that there is a lack of control over the material being removed; not to mention the exact mechanism of the process is still under debate, as previously mentioned. Moreover, it is well known that wet chemistry processes are undesirable in industry for a number of reasons; the process requires large volumes of etchants which need to be repeatedly replaced leading to high costs and large generation of waste. Using a dry etch such as a plasma process is much more favoured due to its controllability and speed. The process generates less waste leading to an overall reduction in costs. The process can also be a combination of physical and chemical etching leading to better selectively.[131-133]

By removing one block in this way as an alternative to the salt inclusion, the pattern can be back filled to create a hard mask, which can be used for pattern transfer.[44] By using this method the drawbacks with the 'ethanol reconstruction' process can be overcome. Therefore, the motivation of this study was to determine a plasma etch which was selective for the removal of P4VP from a PS – *b* – P4VP BCP film to leave a PS matrix, which in turn, could be ultimately back filled for future patterning. It must be noted also that the interaction of this BCP film with dry etch processes is of interest, as this material in particular, will potentially become part of the nanofabrication industry. Limited plasma etching of PS – *b* – P4VP has been investigated to the best of my knowledge. The reason for this is that both PS and P4VP are very similar in molecular structure, the only difference between the two polymers is the nitrogen present in the pyridine ring of P4VP, see Figure 5.1. Hence, obtaining a plasma etch process selective to P4VP is difficult as the PS will be etched also.

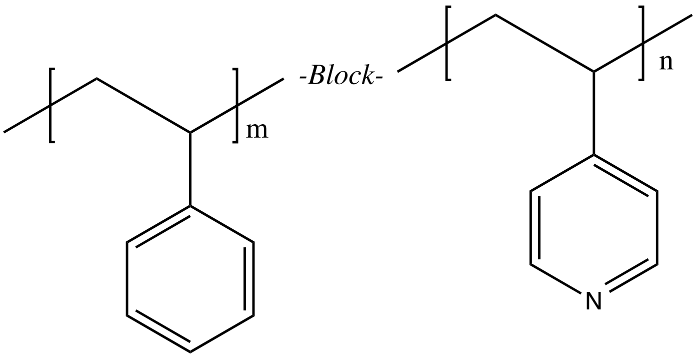

Figure 5.1 *Molecular structure of PS – b – P4VP where m represents the repeating unit for PS and n represents the repeating unit for P4VP. The only difference between both blocks being the nitrogen in the aromatic ring.*

5.2 Results and Discussion

Before moving to BCPs, each block must be investigated individually. This was done using homopolymers which are polymers consisting of the same monomer. A library of P4VP and PS homopolymer films was prepared and etched using oxygen, argon and nitrogen plasmas to determine the etch rate under these different conditions. The etch rate for each polymer was obtained by calculating the removal of material in 30 seconds using ellipsometry. Film thickness did not exceed 40nm for this study as BCP films will not exceed this value when used in nanopatterning applications. BCPs films greater than this will result in multilayers and pattern transfer would be impossible. In each set of experiments, plasma etch processes were performed in triplicate using 3 different coupons. After each process the etch rate of the material was obtained by determining the film thickness and the selectivity of the plasma was calculated using the following equation (5.1)

$$\text{Selectivity for material 1} = \frac{Etch\ rate\ material\ 1}{Etch\ rate\ material\ 2} \tag{5.1}$$

The overall results shown below are taken from the average of the three repeats. The parameters for the oxygen plasma study are listed in Table 5.1.

***Table 5.1** Plasma parameters used for each experiment.*

Plasma No.	Gas Flow (sccms)	Pressure (mT)	Power (W)	Time (s)
Oxygen-1	50	100	50	30
Oxygen-2	50	100	100	30
Oxygen-3	50	100	150	30

Figure 5.2 shows the ellipsometry results for PS and P4VP and Table 5.2 shows selectivity of each plasma for the removal of P4VP over PS. Oxygen is a chemical etch which results in a highly oxidative process where free radicals drive the removal of material.[134] Oxygen plasmas are routinely used to remove polymer material from silicon.[131, 135] For this reason, it is not unusual that all three plasma conditions had high etch rates, with ~15nm or more of the material being removed within the 30 second treatment. This corroborates to similar work carried out by Vesel et al. who studied a library of polymer materials in oxygen plasmas.[135, 136]

The aim to selectively removed P4VP over PS using this gas was not achieved. Each plasma has low selectivity (<1) for the removal of P4VP. The optimal selectivity would be greater than 5 as this would remove enough of the P4VP to allow for an inclusion process for pattern transfer. Moreover, Oxygen showed a selectivity for removing PS, as each plasma exhibited a selectivity greater that 1.5. Perhaps the reason for this is that polystyrene can readily oxidised in oxygen plasmas, where pyridine in known to be an unreactive molecule.

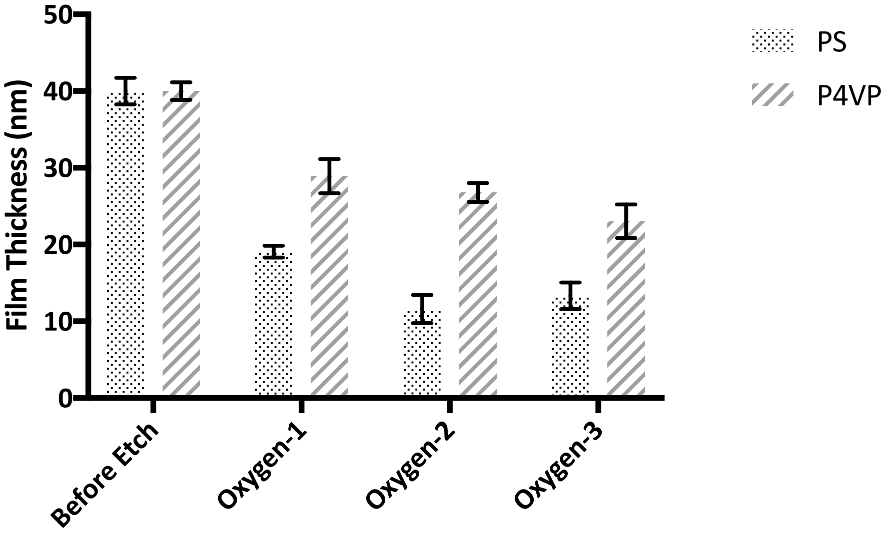

Figure 5 .2 *Oxygen plasma etch studies carried out on homopolymers PS and P4VP.*

Table 5.2 *Selectivity of oxygen plasmas to remove P4VP over PS.*

Plasma No.	***Selectivity for P4VP***	***Selectivity for PS***
Oxygen-1	0.53	1.89
Oxygen-2	0.47	2.15
Oxygen-3	0.64	1.57

Consequently, further investigations using oxygen gas for a selective etch were not carried out. It was then decided to investigate the use of argon as the etch gas. Argon is a physical etch, where ions will bombard the polymer surface to remove material; however, no radicals are formed within this plasma, therefore no chemical etch will occur.[137] It was thought that since the oxygen chemical etch was too aggressive and removed a lot of material, a physical etch might be suited to selectively remove P4VP. The parameters for the argon plasma study are listed in Table 5.3

***Table 5.3** Plasma parameters used for each experiment.*

Plasma No.	Gas Flow (sccms)	Pressure (mT)	Power (W)	Time (s)
Argon-1	50	100	50	30
Argon-2	50	100	100	30
Argon-3	50	100	150	30

Figure 5.3 shows the ellipsometry results for PS and P4VP and Table 5.4 shows selectivity of each plasma had to remove P4VP over PS. Since argon is a purely physical etch the selectively observed in this plasma is due to one material being suppler than the other.

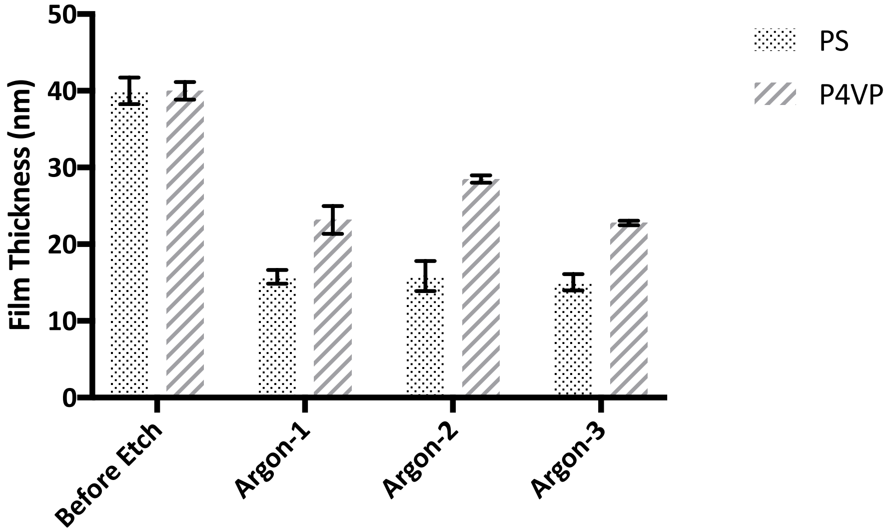

***Figure 5.3** Argon etch studies carried out on homopolymers PS and P4VP.*

***Table 5.4** Selectivity of argon plasmas to remove P4VP over PS.*

Plasma No.	*Selectivity for P4VP*	*Selectivity for PS*
Argon-1	0.69	1.44
Argon-2	0.48	2.10
Argon-3	0.69	1.45

The selectivity calculated and the ability for argon plasmas to removed P4VP over PS was very poor, with all values below 1. Again, this plasma exhibited the ability to removed PS more readily than P4VP with all selectivity values being greater than 1.4. Due to this poor selectivity for the removal of P4VP, argon plasmas were not investigated further.

The final gas to be investigated was nitrogen. Nitrogen is a less aggressive plasma than oxygen. The plasma will predominantly contain ions and radicals which perform surface functionalisation as well as etching of material. During treatment, the formation of free radicals can also induce the insertion of nitrogen-containing species, as seen by the work carried out by Wagner et al.[138] It was thought this less aggressive chemical etch could be the right conditions to obtain selectivity between the two homopolymers. The parameters for the nitrogen plasma study are listed in Table 5.5.

Table 5.5 *Plasma parameters used for each experiment.*

Plasma No.	Gas Flow (sccms)	Pressure (mT)	Power (W)	Time (s)
Nitrogen-1	50	100	50	30
Nitrogen-2	50	100	100	30
Nitrogen-3	50	100	150	30
Nitrogen-4	50	100	200	30
Nitrogen-5	50	100	100	40
Nitrogen-6	50	100	100	50

Figure 5.4 shows the ellipsometry results for PS and P4VP and Table 5.6 shows selectivity to remove P4VP over PS. Surprisingly, each nitrogen plasma investigated gave improved selectivity for removing P4VP over PS in contrast to the previous oxygen and argon plasma. Plasma 2 and 3 were the best conditions giving a selectively of 2.20 and 2.10, respectively.

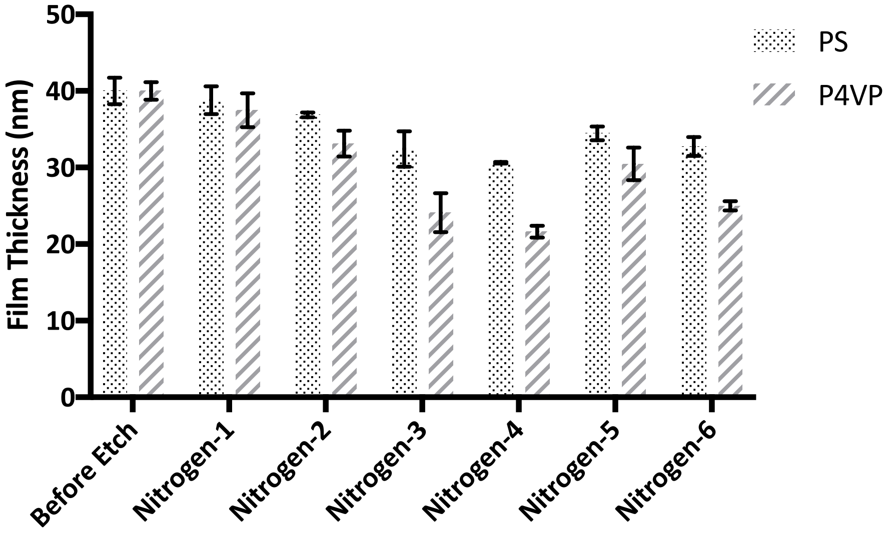

Figure 5.4 *Nitrogen etch studies carried out on homopolymers PS and P4VP.*

Table 5.6 *Selectivity of argon plasmas to remove P4VP over PS.*

Plasma No.	***Selectivity for P4VP***	***Selectivity for PS***
Nitrogen-1	2.09	0.48
Nitrogen-2	2.20	0.45
Nitrogen-3	2.10	0.48
Nitrogen-4	1.96	0.51
Nitrogen-5	1.72	0.58
Nitrogen-6	2.07	0.48

This was unexpected as both nitrogen plasma and pyridine are known to be very unreactive. These plasma processes were repeated many times and across two different plasma tools. The results concluded that nitrogen plasmas had selectivity for removing P4VP over PS across different tools. It must be noted that this selectivity is low and not the optimal of >5. However, this plasma process can be further improved on with plasma diagnostics techniques.

5.2.1 P2VP Nitrogen etch studies

The key question to answer is why nitrogen plasmas have selectivity for P4VP over PS. Since PS and P4VP only differ in structure by the nitrogen in the aromatic ring, it was hypothesised that the nitrogen plasma was reacting with the lone pair of electrons at the nitrogen in the pyridine ring, causing it to break down more easily than the benzene ring of the PS. To investigate this hypothesis further, poly(2-vinylpyridine) (P2VP) was investigated. This molecule is similar to P4VP, however the nitrogen in the aromatic ring has moved position, see Figure 5.5. By moving the nitrogen to this position, the lone pair of the nitrogen in the aromatic ring becomes more sterically hindered, and in theory, should not interact with the plasma as readily as P4VP. P2VP was then investigated with various nitrogen plasma conditions, see Table 5.7.

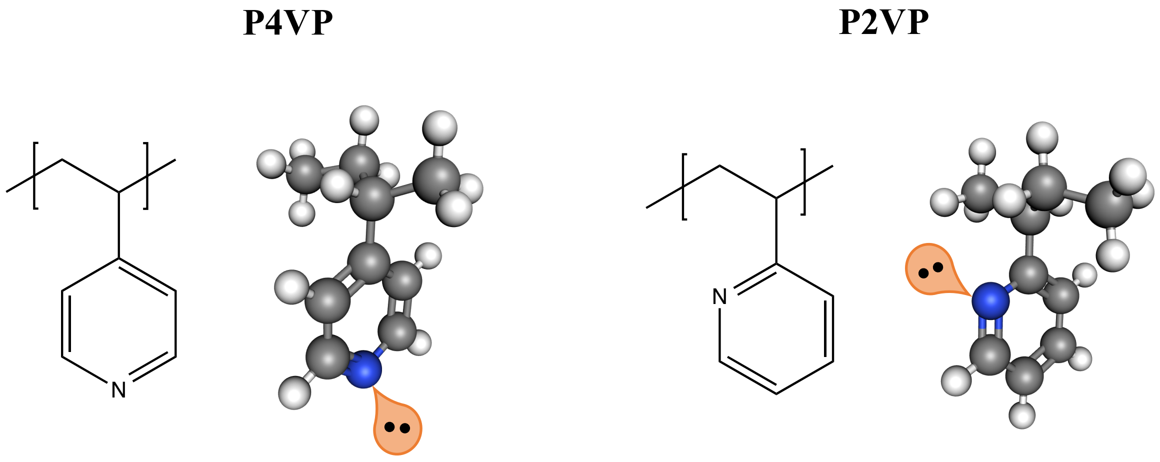

Figure 5.5 Chemical structure of P4VP and P2VP showing the position of the nitrogen in the aromatic ring.

Table 5.7 *Plasma parameters used for each experiment.*

Plasma No.	Gas Flow (sccms)	Pressure (mT)	Power (W)	Time (s)
Nitrogen-1	50	100	50	30
Nitrogen-2	50	100	100	30
Nitrogen-3	50	100	150	30
Nitrogen-4	50	100	200	30

Figure 5.6 shows the ellipsometry results for P2VP after nitrogen plasmas. Table 5.8 shows the selectivity calculated for the nitrogen plasmas to removed P2VP over PS. As expected, the results show little selectivity with all values being under 1. This result brings us a step closer to understanding why nitrogen has selectivity for removing P4VP over PS and perhaps the position of the nitrogen in the aromatic ring plays an important role in etch selectivity.

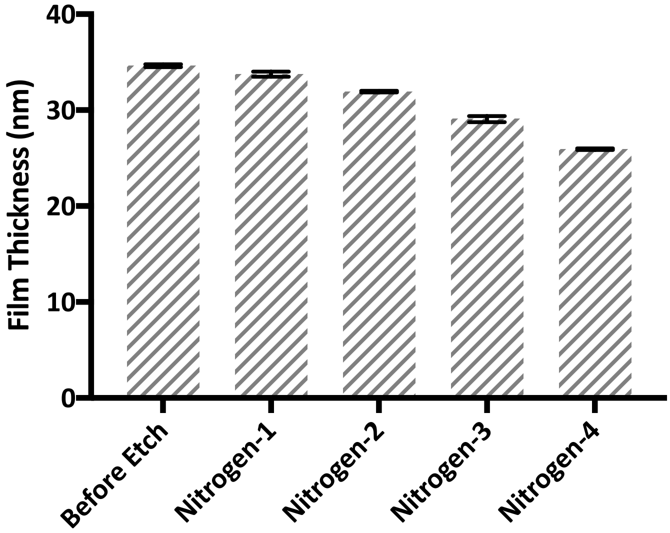

Figure 5.6. *Ellipsometry results for P2VP before and after nitrogen etch.*

Table 5.8 *Selectivity of nitrogen plasmas to remove P2VP over PS.*

Plasma No	***Selectivity for P4VP over PS***
Nitrogen-1	0.36
Nitrogen-2	0.54
Nitrogen-3	0.59
Nitrogen-4	0.91

To clarify the mechanism behind the etching of P2VP in nitrogen plasmas, x-ray photoelectron spectroscopy (XPS) alongside *in situ* plasma etching was carried out. The plasma chamber attached to the XPS tool uses forming gas instead of pure nitrogen. This is a mixture of nitrogen and hydrogen (< 5.7%), which is used to passivate trace oxygen within the plasma chamber. To determine if this plasma chamber was comparable to the plasma chamber used in the etch studies, both systems were calibrated with optical emission spectroscopy.

The region from 280 – 400 nm is associated with molecular nitrogen and indicated that the plasma contained predominantly neutral and some N_2^+ ions, which was expected. This confirmed both plasma contained similar reactive species and were comparable in etch characteristics, see Figure 5.7.

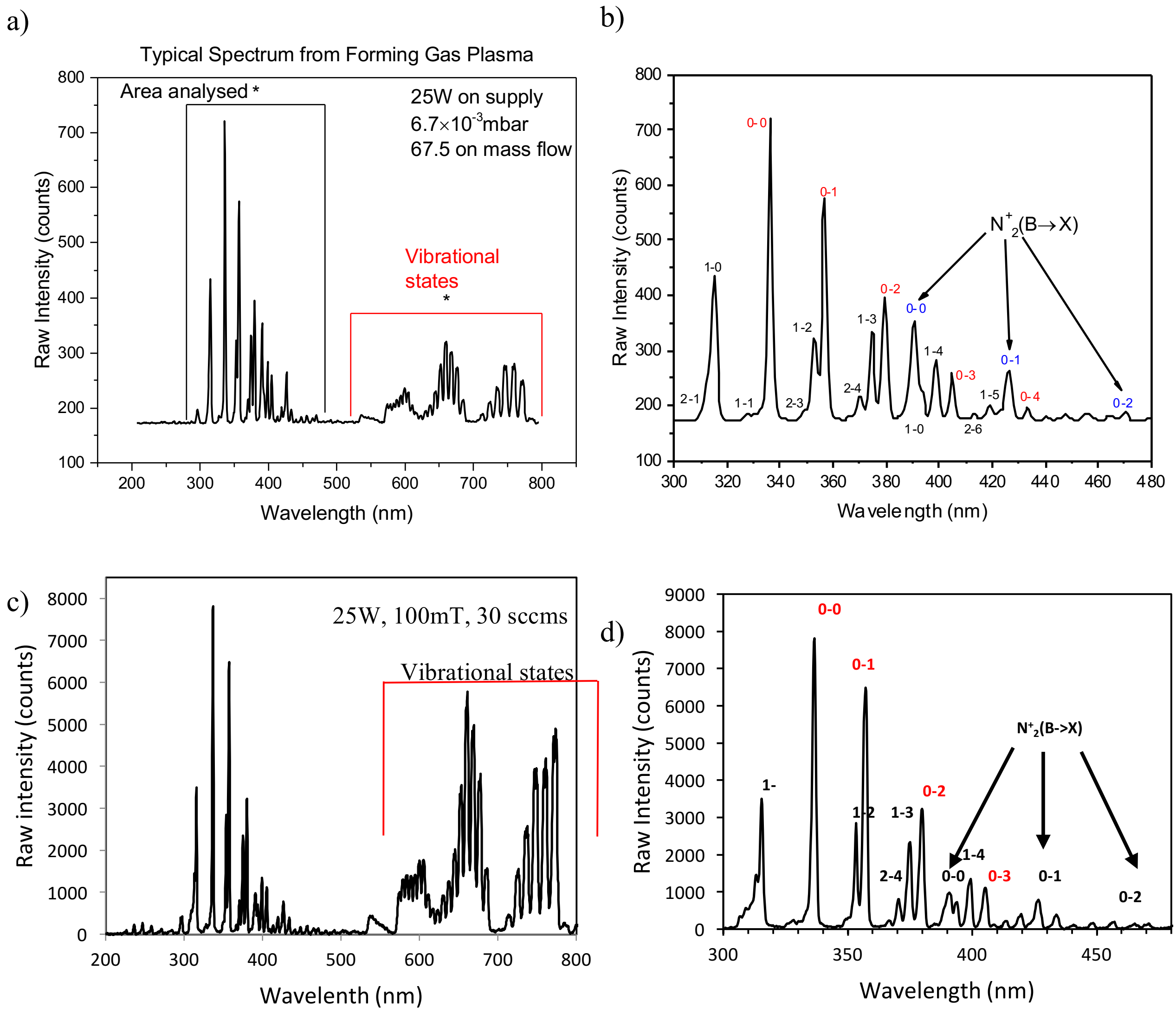

Figure 5.7 *a) OES spectra of forming gas plasma at in the XPS in situ plasma tool. b) The same OES spectra without the vibrational states. c) OES spectra of* N_2 *plasma at 100W, 100mT and 30sccms in the Oxford plasma tool. d) The same OES spectra without the vibrational states.*

Using the survey spectra of P2VP and P4VP before and after an *in situ* nitrogen plasma etching, the relative elemental concentrations of carbon, nitrogen, oxygen and silicon within the samples was calculated, see Figure 5.8. These values were calculated using the integrated areas of atomic sensitivity factors for the C 1s, N 1s, O 1s and Si 2p core level peaks.

The main effect of the forming gas plasma has on the polymer samples is the removal of carbon. From the chemical composition percentage acquired from the survey spectra it is clear from the carbon content that P4VP is being etched more rapidly when compared to P2VP. The results show P2VP only reducing by 4% after a 30 second forming gas plasma treatment, whereas the P4VP carbon percentage drops by 17% after a 30 second nitrogen plasma treatment. However, we also see an increase in nitrogen and oxygen signals.

It would seem that some of the nitrogen from the plasma may be becoming incorporated into both films. This correlates to Wagner et al. who experienced similar results when performing nitrogen radio frequency (RF) plasmas on polyethylene.[138] In their work, the addition of nitrogen was apparent after plasma treatment upon XPS characterisation. The increase in oxygen seen in Figure 5.8 a) may be explained by residual oxygen contamination within the chamber. This is not ideal, but it is not unusual to have small oxygen contamination in a research laboratory set-up, hence, why the passivating forming gas is used.

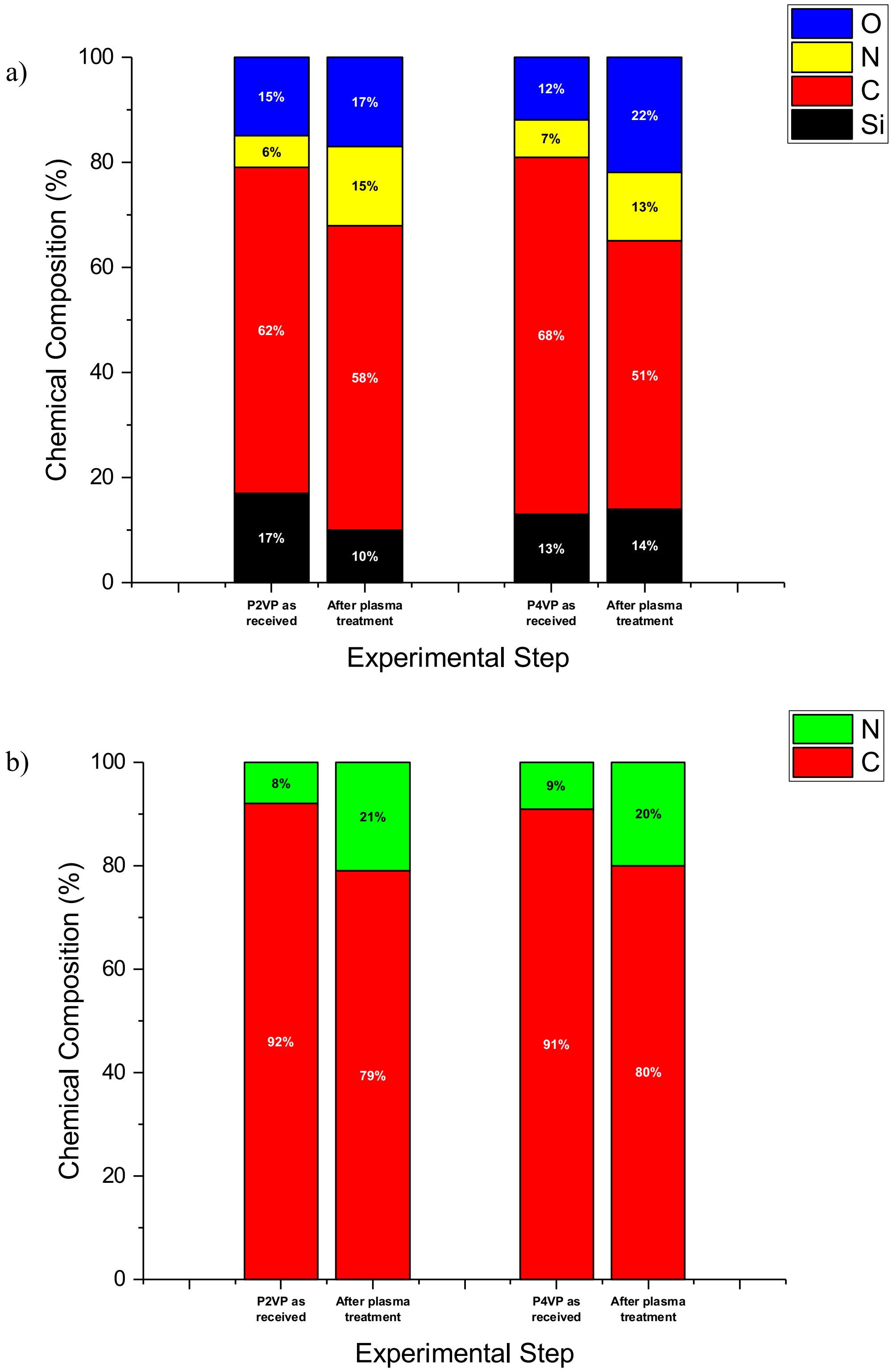

***Figure 5.8** a) Chemical composition of P2VP and P4VP before and after treatment with nitrogen plasma showing oxygen, nitrogen, carbon and silicon ratios. b) Chemical composition of P2VP and P4VP before and after treatment with nitrogen plasma showing nitrogen and carbon ratios.*

Assuming that all the nitrogen and carbon signals obtained from the XPS within the samples is solely from the PVP, it can be seen that both the P2VP and P4VP are identical in terms of carbon:nitrogen (C:N) ratio in their received state, see Figure 5.8 b). After plasma treatment, it appears that although the ratio changes, indicating nitrogen incorporation, both samples again maintain the same ratio. However, from the carbon signals in Figure 5.8 a) that P4VP appears to etch more than P2VP. So, from both the overall chemical composition calculation and the C:N ratio we can postulate that the etch mechanism is similar in both samples, but the etch is more effective for the P4VP sample.

To investigate the chemical interactions at these interfaces, narrow energy window scans were taken at C 1s, N 1s and O 1s regions for samples prior and post plasma treatment and are displayed in Figure 5.9. It should be noted that these spectra are presented as raw data (without any normalisation) to allow direct comparison of the samples.

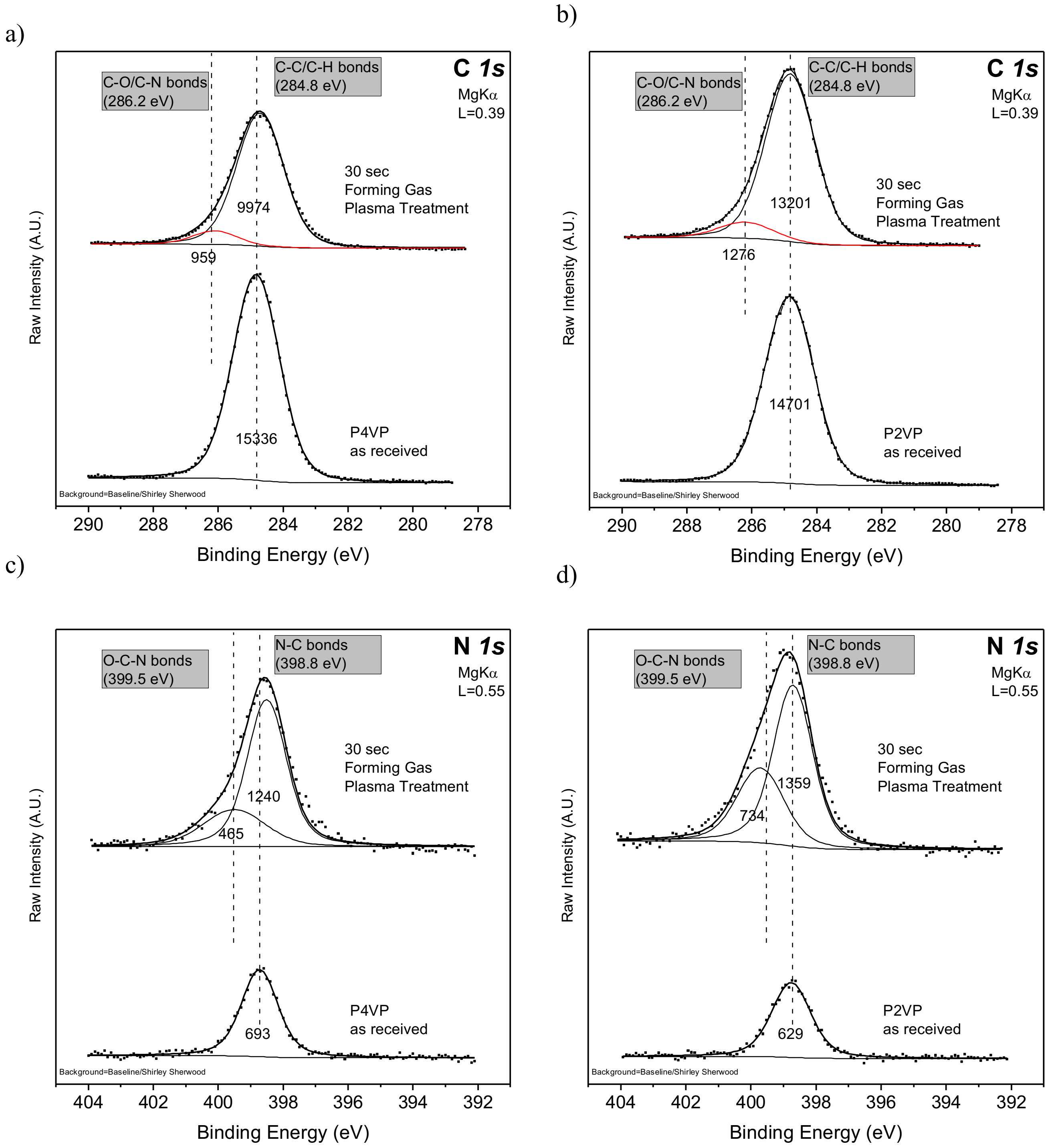

Figure 5.9 *a) and b) C1s spectra for P4VP and P2VP as received and after plasma treatment, c) and d) N 1s spectra for P2VP and P4VP before and after plasma treatment.*

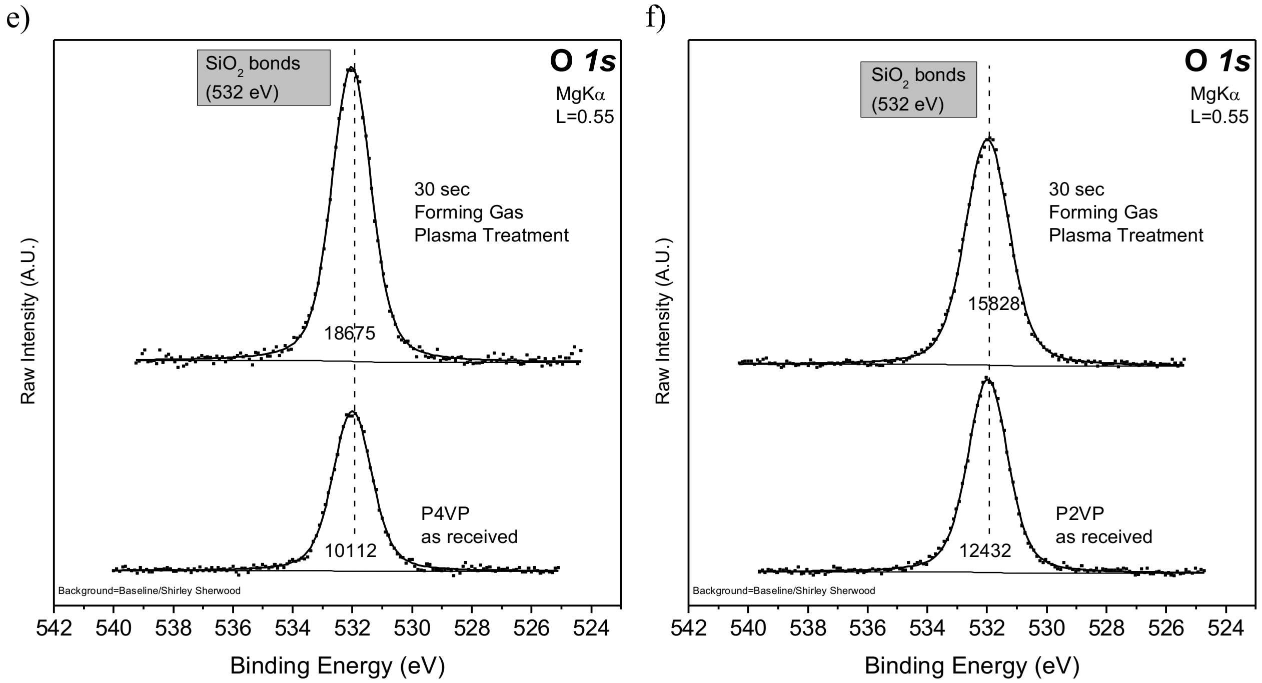

***Figure 5.9 e)** and f) O 1s spectra for P2VP and P4VP before and after plasma treatment.*

The key findings from the C 1s spectra were that the overall peak area for P4VP is reduced, shown in Figure 5.9 a). Although P2VP shows a reduction also, 35% of the P4VP was etched, whereas 11% of P2VP was removed. The peak found in the post etch spectra for both samples at 286.2 eV indicates carbon binding to nitrogen and/or oxygen. As the electronegativity of O and N is higher than that of C, the presence of a carbon-oxygen bond would result in an increase in the binding energy of the associated C atoms. It is impossible to differentiate between C-O or C-N bonds with conventional XPS, as the electronegativity values of N and O are so similar, and the resolution on conventional XPS cannot resolve the peaks.

Moving to the N1s spectra, the post etch spectra show multiple peaks representing that nitrogen is now bonded to more than one chemical species. The peak at 399.5 eV is most definitely attributed to an oxygen species. The reason for this is that there is no other species it could be bonded to as 1) there are no additional elements in the system and 2) the electronegativity of O is high, therefore the additional peak at the higher binding energy in the N1s must be attributed to O incorporation.

With this result, along with the peak seen in the C 1s, it can be concluded that there are traces amounts of oxygen within the plasma chamber which is bonding to nitrogen in P4VP and P2VP post plasma etch. Again, it is not unusual for trace amounts of oxygen to be present in a plasma chamber in a research laboratory set-up. This result reflects the work of Sanchis et al. In their research, polyurethane films were exposed to radio frequency (RF) low-pressure nitrogen plasmas. XPS spectra revealed an increase in oxygen after plasma treatment due to trace amounts of oxygen being present in the plasma tool during the etch process.[139]

This presence of oxygen was then confirmed with the O 1s spectra shown in e) and f). The increase in intensity post etch indicates oxygen in the plasma but can also be indicative of uncovering of the SiO_2 substrate which would be expected post etch. This would also explain why the intensity is higher in e) rather than f) as more materials is being removed in e) uncovering more of the SiO_2 interface.

It was hypothesized that the position of the nitrogen in the pyridine ring played an important role in etch mechanism, moreover, that the etching of poly(vinyl-pyridine) materials begins at the most chemically active region of the nitrogen in the pyridine ring. P4VP and P2VP are seen to be identical before and after plasma treatment shown in the chemical composition obtained by XPS (Figure 5.9 (b)), from both the overall chemical composition calculation and the C:N ratio it can be postulated that the PVP etch mechanism is similar in both samples, but the etch is more effective for the P4VP sample. Since the only difference between these molecules is the position of the nitrogen in the aromatic ring, it can be concluded that the reason why P4VP is etched more rapidly is due to the nitrogen in the pyridine ring being positioned where it is not sterically hindered by other groups within the polymer chain and can interact with the plasma easily. The position of the nitrogen in P2VP is not as readily available as it is sterically hindered within the molecule, see Figure 5.5. From this it can be concluded that the nitrogen position in the pyridine results in the molecule breaking down more rapidly than the corresponding PS molecule, leading to etch selectivity in nitrogen plasmas.

5.2.2 Selective Etch of BCP using nitrogen plasma

It has been demonstrated that nitrogen plasma has a selectivity for removing P4VP over PS. This was carried out using homopolymers, it must now be demonstrated using the microphased BCP film, an industrially relevant material that will possible be incorporated into semiconductor manufacturing. Therefore, two samples of PS – b – P4VP were annealed to produce microphased BCP films with PVP core diameter of 21.3nm and a pitch of 25.5nm. Post annealing, one sample was etched with a nitrogen plasma etch at 30sccms, 100W, 100mt for 30s, in the Oxford Instrument plasma tool and the other sample was reconstructed/activated with ethanol. FESEM micrographs of each sample are shown in Figure 5.10.

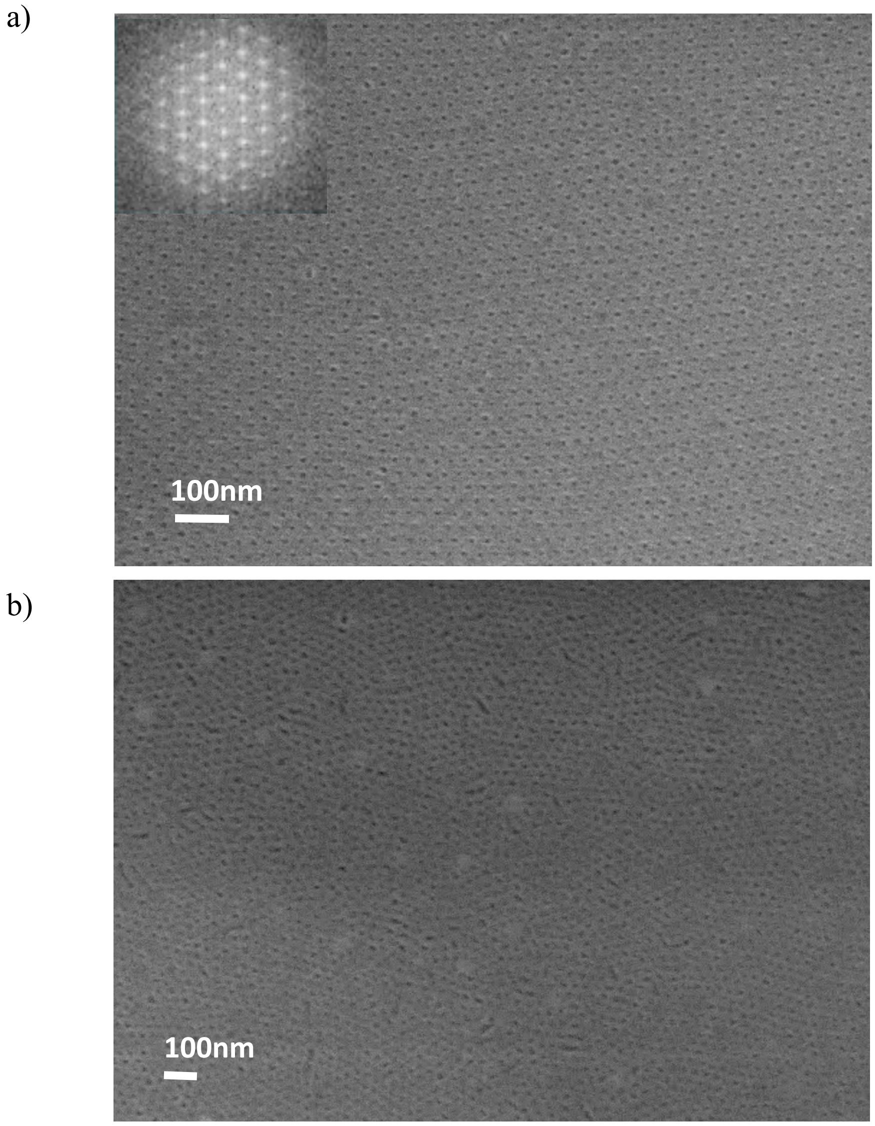

Figure 5.10 *SEM micrographs of PS – b – P4VP films that have been a) ethanol reconstructed and b) have been etched with nitrogen plasma.*

From the SEM images shown in Figure 5.10, it is clear that the nitrogen plasma has selectively removed the P4VP cores. To the best of our knowledge, this is the first demonstration of nitrogen plasmas to have a selective effect on $PS - b - P4VP$ thin film.

5.3 Conclusion

Our results demonstrate the development of a selective plasma etch process for the removal of P4VP cores from $PS - b - P4VP$ nanopatterned film. Results have shown that a nitrogen reactive ion etch (RIE) plasma has selectivity for P4VP of 2.2:1. The work presented suggested that the position of the nitrogen in the aromatic ring plays a key role in this selectivity, which was investigated further using *in situ* plasma etching and XPS spectrometry measurements. Results confirmed the quick removal of P4VP by a nitrogen plasma when compared to the sterically hindered P2VP, concluding that the position of the nitrogen in the pyridine molecule is related to etch mechanism in nitrogen plasmas. XPS data revealed the incorporation of nitrogen and oxygen into the polymer film during the etch process.

5.4 Future Work

Further optimisation of the nitrogen etch must be carried out to reach the goal selectivity of >5. Using plasma diagnostics, specifically optical emission spectrometry (OES) and mass spectrometry could aid the improvement of selectivity and will be subject to further investigation. It is evident in the SEM characterisation in Figure 5.10 b) that the nitrogen etch is removing the cores, however TEM and/or AFM characterisation would give valuable insight into how the polymer has been removed inside the core.

Chapter Six

6 Surface engineering of polymer brush layers in order to control BCP orientation

6.1 Introduction

As mentioned in chapter

one, controlling the wettability, surface energy and functionality of the substrate surface prior to spin-coating a BCP is extremely important to control the BCP orientation. Typically, BCP orientation is controlled by brush layers, usually consisting of homopolymers or random copolymers, which are end-terminated with a hydroxyl group to ensure grafting to the silicon substrate. A brush layer will either be preferential to one block, or neutral to both blocks. Choosing a preferential brush layer will drive lamellae and cylinders to orient parallel to the surface. While choosing a neutral brush layer will drive lamellae and cylinders to orient perpendicular to the surface, see Figure 6.1.

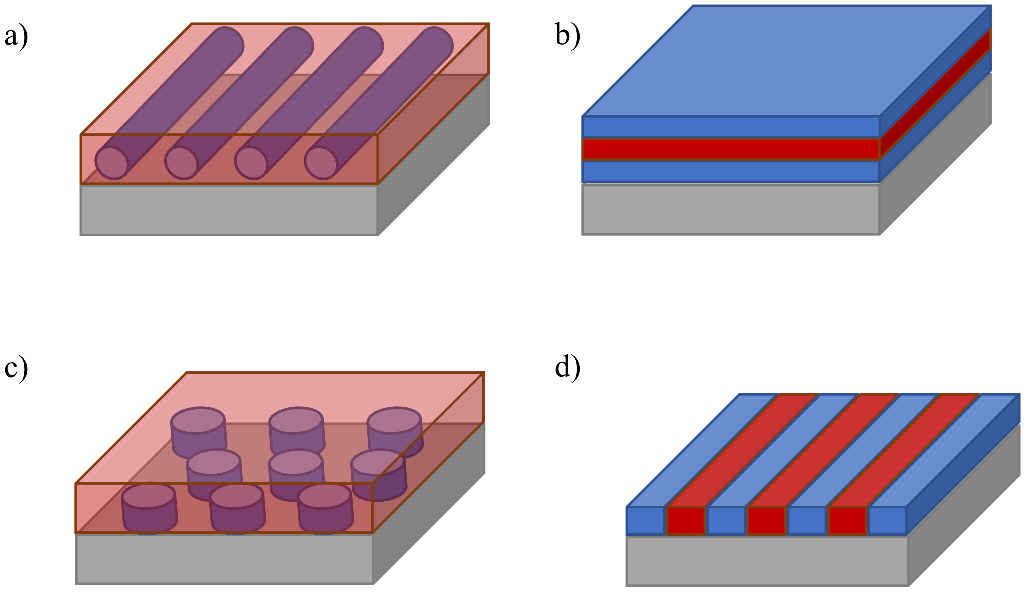

Figure 6.1 *a) Parallel aligned cylinders, b) Parallel aligned lamellae. Preferential wetting brush layers will result in these BCP morphologies. c) Perpendicular aligned cylinders, d) Perpendicular aligned lamellae. Neutral wetting brush layers will result in these BCP morphologies.*

Oria et al. have previously demonstrated that treating PS brush layers with oxygen plasma modifies the surface to the extent that the PS is converted from a preferential brush layer to a neutral brush layer. [140] In their study, they investigated lamellae forming PS – *b* – PMMA, which aligned to the surface in various orientations depending on the chemical character of the PS brush layer under the BCP. Motivated by this work, the effect of treating PS with oxygen plasmas on our cylindrical forming BCP systems PS – *b* – PMMA and our highly controllable plasma conditions was investigated. In this chapter, PS – *b* – PMMA was chosen to be investigated, as it has added to the library of materials studied. PS – *b* – PMMA is the most highly researched BCP for applications in IC manufacturing, therefore understanding this material is of importance for future work. PS is a preferential brush layer, by treating this with an oxygen plasma and changing the surface chemistry, the aim is to convert the preferential brush layer into a neutral brush layer. This would result in BCP orientation changing from parallel to perpendicular cylinders, See Figure 6.2.

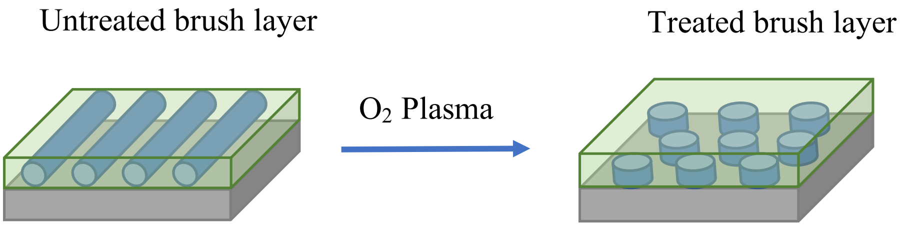

Figure 6.2 *Schematic outlining the aim of this work to convert PS from a preferential brush layer to a neutral brush layer, resulting in control of PS – b – PMMA orientation.*

Achieving this result would be of benefit as BCPs patterns with different orientation could be generated using the same brush layer, thus generating a shorter process. Guiding patterns fabricated by plasma treatment could control which direction for the BCP to align to the substrate.

6.2 Results and Discussion

An initial set of plasma experiments were carried out to see the effect of oxygen plasma on the PS brush layer. PS thin film samples were prepared as described in the experimental section. The design of experiments chose a wide range of plasma parameters, by investigating these plasma conditions the key parameters were identified which needed to be controlled during the plasma treatment.

The parameters of the plasma needed investigating were:

1. Power, measured in watts (W).
2. Pressure, measured in millitorr (mT).
3. Time, measured in seconds (s).
4. Gas flow, measured in standard cubic centimetres per minutes (sccms).

Conditions chosen are stated below, see Table 6.1. Each experiment was done in duplicate and a centre-point was recorded at the start, middle and end of experiments. A centre-point is a process run using mid-range values for all parameters. This is important to record any hysteresis that may occur within the plasma chamber during experiments.

***Table 6.1** Plasma parameters used for each experiment.*

Sample	Power (W)	Pressure (mT)	Time (s)	Flow (sccms)
Centre Points	125	35	13	30
Exp 1	50	20	5	10
Exp 2	200	20	5	50
Exp 3	50	50	5	30
Exp 4	200	50	5	10
Exp 5	50	20	20	50
Exp 6	200	20	20	10
Exp 7	50	50	20	10
Exp 8	200	50	20	50

The results presented in Table 6.2 show the water contact angle (WCA) and surface energy results from the initial plasma experiments. All surface energy values in this report are calculated using the OWRK method by measuring the contact angle of two liquids, water and diiodomethane as stated in chapter two. All values are statistically relevant. Looking at the results on a whole, the key finding from this set of experiments, was that plasma pressure and gas flow do not seem to play an important role in the change of wettability and surface energy. Two extremes of pressure and flow were used in experiment 1 and experiment 3 keeping power and time low. The change in wettability and surface energy were modified the least using these conditions. Power and time seem to be the main driving factors attributed to the change in surface chemistry. high power and long time were used in experiment 6, where the highest surface modification was measured. The wettability was reduced from 96° down to ~10°, see Figure 6.3. The wettability has a direct effect on surface energy, as discussed in the chapter two. Here we see a change from 44 mJ/m^2 to a range between 70-81 mJ/m^2.

Table 6.2 *Water contact angle and surface energy results from initial plasma experiments.*

Sample	WCA (degrees)	Surface Energy (mJ/m^2)
PS Before Treatment	96 ± 2	45
Centre Points	9 ± 2	76
Exp 1	24 ± 2	72
Exp 2	10 ± 1	78
Exp 3	16 ± 1	74
Exp 4	10 ± 1	78
Exp 5	9 ± 1	78
Exp 6	8 ± 1	81
Exp 7	14 ± 1	76
Exp 8	10 ± 1	81

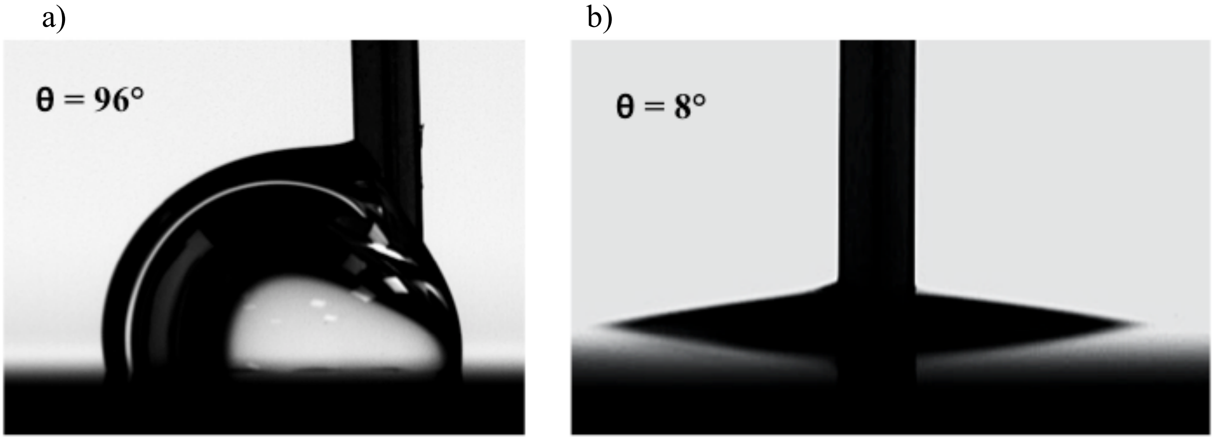

Figure 6.3 *a) PS water contact angle before plasma treatment showing a contact angle of 96°, b) PS water contact angle after plasma treatment (Exp 6) showing a contact angle of 8°.*

The key question of finding is - what is causing this significant change in wettability and surface energy? This change in contact angle after plasma treatment is similar to what has been described in the literature. Murakami et al. reported a change in contact angle from 92° to 7° after plasma treatment.[141] XPS characterisation of these films revealed the formation of hydroxyl, carbonyl and carboxyl groups on the surface post plasma treatment.[142] They concluded the change in contact angle was attributed to the addition of the oxygen-containing polar functional groups during plasma treatment.

This initial set of experiments was investigated further, this time honing in on the parameters of the plasma and using ellipsometry measurements to record the removal of PS material in each etch. A change in wettability is largely attributed to two effects:

1. A result of a change of surface chemistry
2. A change surface roughness

Both effects are possible during the plasma treatment. From the literature, we expect the change in surface chemistry is a result of the addition of oxygen groups on the surface. However, roughness must be determined also. AFM was carried out to record the roughness values of the PS surface before and after plasma treatment. Another aim of this experiment was to further control the wettability and thus the surface energy of the brush layer. From the initial experiment, gas flow was shown to have little effect on wettability therefore the flow was kept constant at 30sccms. The process parameters are shown in Table 6.3.

Table 6.3 *Plasma parameters used for each experiment.*

Sample	Power (W)	Pressure (mT)	Time (s)
Centre point	160	60	18
Exp 1	40	20	30
Exp 2	280	20	5
Exp 3	40	100	5
Exp 4	280	100	30

Table 6.4 shows the WCA, surface energy and ellipsometry results for each plasma experiment. It is important to note that thickness of the PS film is a lot thicker than expected for BCP brush layers, typically brush layers are below 7nm. As it was not known how much polymer material would be etched away during each treatment, thick films were prepared to make sure there was still PS left on the surface to be

measured for WCA and surface energy. For the thickness values, limited material was etched during plasma treatment (on average 11%) with experiment 4 being an exception (76% of the material being etched). This was expected, as this experiment had high power and high time, and therefore a lot of material was etched during the process. The wettability and surface energy were seen to be radically modified again. However, the aim to further control the surface energy wasn't achieved. A range of 76-80 mJ/m^2 was achieved in this case. To determine if the surface was becoming rougher during the plasma process, AFM characterisation was carried out.

Table 6.4 *Dynamic water contact angle and surface energy results.*

Sample	WCA (degrees)	Surface Energy (mJ/m^2)	Film Thickness (nm)
PS Before Treatment	93 ± 2	45	168 ± 1
Exp 1	8 ± 1	78	160 ± 1
Exp 2	9 ± 1	79	154 ± 1
Exp 3	9± 1	76	157 ± 1
Exp 4	8 ± 1	78	42 ± 1
Centre Points	7 ± 1	80	129 ± 1

Roughness can be described as closely spaced irregularities on the surface and the value depends on a scale measurement. There are two measurements of importance, the roughness average (R_a) and the root mean square (RMS) roughness. R_a is an arithmetic mean of the absolute values of height of a surface profile. However, R_a makes no distinction between peaks and valleys, making R_a irrelevant for the work present herein, as we expect both peaks and valleys to be present on the surface. RMS roughness is a function that takes the square of the measures. Similar to R_a, although the mean squared of the absolute values of a surface is calculated. RMS is more sensitive to peaks and valleys than R_a due to the squaring of the amplitude in its calculation. For this reason, RMS values are calculated and presented in this chapter.[113]

Table 6.5 *RMS roughness values obtained for each sample using AFM.*

Sample	RMS Roughness
PS	0.34nm
CP1	1.12nm
Exp 1	0.71nm
Exp 2	0.53nm
Exp 3	0.39nm
Exp 4	7.49nm

From the RMS roughness analysis shown in Table 6.5, it is evident that the roughness is not having an impact on the surface energy, as the roughness is predominantly under 2nm. Experiment 4 has high roughness, as expected, due to the high-power plasma conditions used for the sample, which results in more material being etched away. However, the surface energy calculated for this sample is the same as other experiments carried out. Figure 6.4 shows representative AFM height images in 2D and 3D format of a) PS before treatment b) center-point1 c) experiment 1 d) experiment 2 e) experiment 3 f) experiment 4.

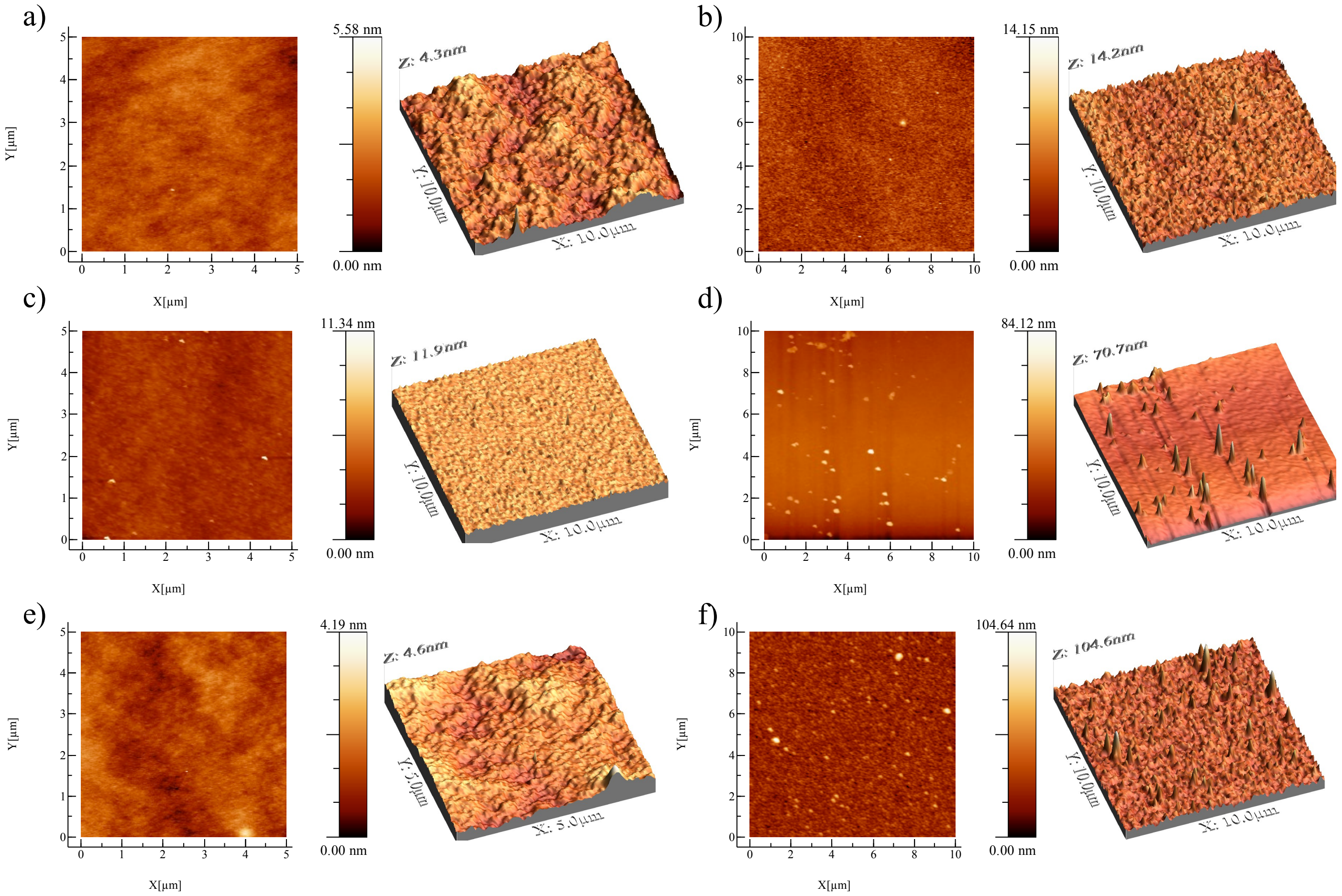

Figure 6.4 *Representative AFM height images in 2D and 3D format of a) PS before treatment b) center-point1 c) experiment 1 d) experiment 2 e) experiment 3 f) experiment 4.*

Larsson et al. performed similar experiments on PS using oxygen plasmas. Their AFM roughness analysis showed an increase of RMS roughness after plasma treatment from 1.3nm to 3.8nm. The roughness was shown to increase as the intensity of the plasma was increased. [143] Equally, Vesel et al. showed a linear increase in surface roughness as plasma treatment time increased. [144] From the roughness analysis results presented above, it was suspected that the notable change in wettability and surface energy are attributed to a change in surface chemistry caused during the plasma treatment and not due to topographic characteristics of the surface. The aim to control the change in surface energy, still needs to be achieved. To see if this was possible, another set of experiments was carried out, this time using the two plasma extremes.

The first plasma process with low time and low power, the second plasma with high time and high power. Each experiment was carried out in triplicate and the mean results are presented. The gas flow was kept constant as in the previous set of experiments at 30 sccms oxygen and 1.5 sccms argon. Pressure was adjusted so the plasma could strike for each experiment. The conditions of the plasma are noted in Table 6.6.

Table 6.6 *Plasma parameters used for each experiment.*

Sample	Power (W)	Pressure (mT)	Time (s)
Exp1	40	120	1
Exp 2	300	20	30

The film thickness, water contact angle and surface energy results are presented in Table 6.7. For the experiments at low time and low power less than 1% of PS was removed by the plasma treatment. For the experiments at high time and high power, 64% of material was etched. This was expected for the plasma parameters used. Moreover, the key finding in this set of experiments was that the wettability and therefore surface energy was controlled further. For experiment 1 at the low power conditions, where a manually timed 1s plasma treatment was used, the surface energy recorded was 65 mJ/m^2.

Table 6.7 *Ellipsometry, dynamic water contact angle and surface energy results.*

Sample	WCA (degrees)	Surface Energy (mJ/m^2)	Thickness (nm)
PS no treatment	93 ± 1	45	176 ± 1
Low	35 ± 1	65	175 ± 1
High	7 ±1	80	64 ± 1

6.2.1 SIMS Analysis

The roughness analysis carried out confirmed that the change in wettability is attributed to changes in surface functionality, not topographic changes. To obtain further information about the change in surface chemistry occurring during the plasma treatment, SIMS spectra were collected to determine the elemental composition of the surfaces post plasma treatment. From Figure 6.5 it can be clearly seen that the films treated with oxygen plasma contained more oxygen species than PS with no plasma treatment. The SIMS spectra show significant increases to the peaks representing O^-, OH^-, CH_3O^- and O_2^-. These oxygen species correlate to the functional groups detected by XPS in other studies. Dupont-Gillain et al. measured an increase of alcohol/ether, aldehyde/ketone, ester/carboxylic acid and finally carbonate groups post oxygen plasma treatment on PS substrates.[145] It must be noted that there was a considerable amount of oxygen measured in the untreated PS sample. This is possibly due to the PS film oxidising in atmosphere before measuring SIMS, as sample are not stored in a vacuum prior to measurement. This presence of oxygen in untreated samples was also seen in XPS characterisation carried out in the work by Murakami et al.[141] It must be noted that SIMS is a qualitative technique and not quantitative. To obtain a more quantitative analysis of the surfaces preliminary Fourier transform infrared spectroscopy (FTIR) analysis was carried out.

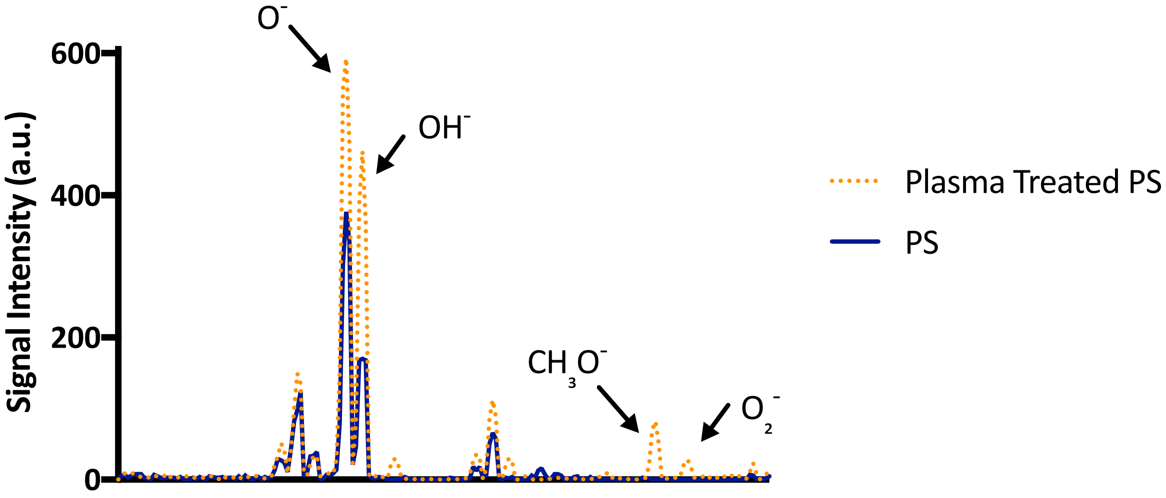

Figure 6.5 SIMS analysis of polystyrene and plasma treated polystyrene.

6.2.2 ATR Analysis

ATR analysis was carried out to obtain a quantitative view of the functional groups present on the surface. PS before and after an oxygen plasma treated was measured and the results are displayed in Figure 6.6 The broad peak seen at 3500 cm^{-1} shown in the oxygen plasma treated film is attributed to addition hydroxyl groups on the surface post oxygen plasma. However, this peak is very weak and therefore does not confirm in the surface is becoming saturated with oxygen-containing groups during the plasma process. Further surface analysis with higher resolution, such as XPS is needed to obtain a clearer understanding of surface functionality.

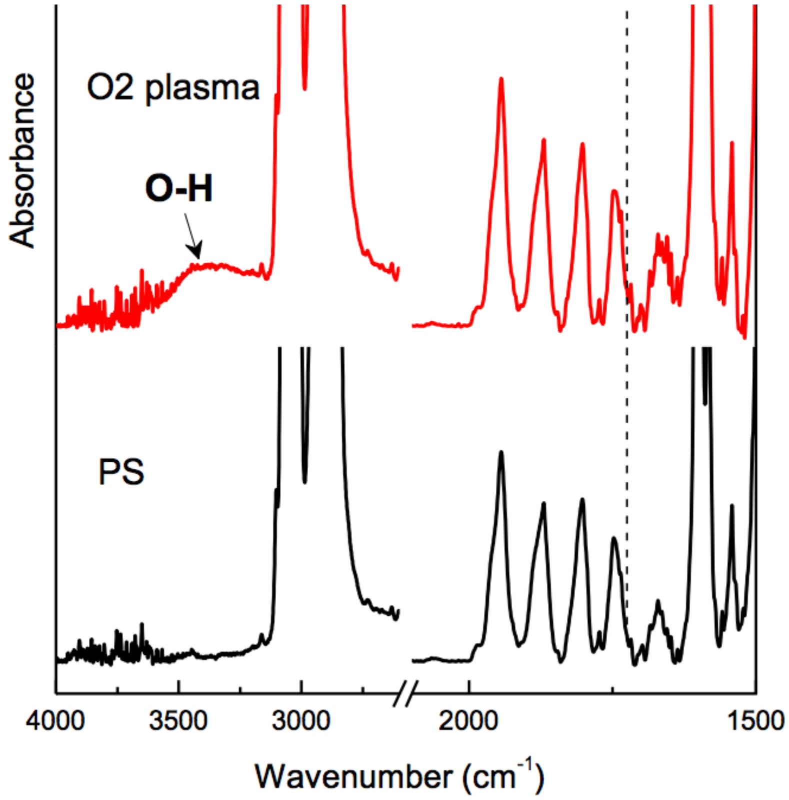

__Figure 6.6__ ATRR analysis of PS before and after oxygen plasma treatment.

For all experiments discussed thus far, the timing of the plasma process was controlled manually. Due to this, it was suspected the varying surface energy results between repeats was due to the sample getting a fraction of a second longer processing time. To control this more accurately, a plasma timing protocol was put in place.

Additionally, this result in Table 6.7 showed that the PS brush layer is modified by the plasma treatment in a very fast time. If we want to control the surface energy even further, less that 1s processing time was explored.

For this purpose, a plasma control unit which can now control plasma on/off states to the millisecond was installed in the Oxford Instruments Plasmalab tool. This new set-up has allowed for a pulsed plasma phase. The difference between this pulsed plasma and the normal plasma which has been used thus far, is that a pulsed plasma reaches a stable phase much faster than the normal plasma. Normal plasmas consist of a preliminary phase which is normally 2-5s long where the plasma is reaching a stable phase. This pulsed plasma reaches this stable phase in milliseconds. Since this pulsed plasma reaches this plasma 'stable phase' more rapidly than the normal plasma, it was expected that the pulsed plasma would be a more reactive plasma than the normal. For this reason, a shorter time was used, see Table 5.8. Each experiment was carried out in triplicate. The parameters for each plasma are noted in Table 5.8.

Table 6.8 *Plasma parameters used for each experiment.*

Exp No.	**Time**	**Power**	**Pressure (mJ/m^2)**	**Gas**
1 **(Normal Plasma)**	0.64	40W	120mT	O_2 30sccms
2 **(Pulsed Plasma)**	0.06	40W	120mT	O_2 30sccms

The results presented in Table 6.9 show the ellipsometry, wettability and surface energy results calculated for each sample. The wettability and surface energy results were not as expected. In both cases the wettability did not significantly reduce as seen in previous experiments, and for the pulsed plasma, the water contact angle seemed to increase slightly. Likewise, the surface energy did not increase as seen previously, but decreased. The normal plasma produced a surface energy of 13.24 mJ/m^2 and the pulsed plasma produced a surface energy of 28.34 mJ/m^2.

Table 6.9 *Ellipsometry, dynamic water contact angle and surface energy results.*

Sample	WCA (degrees)	Surface Energy	Thickness (nm)
PS (no treatment)	93 ± 1	45	171 ± 1
Low	100 ± 1	13	170 ± 1
High	105 ± 1	28	170 ± 1

To understand this trend in change in surface energy, plasma experiments to date were plotted together. The results are shown in Figure 6.7. From the results presented above it is clear that a change in wettability occurs during the oxygen plasma treatment, although this change only occurs once the PS brush layer has been exposed to plasma for more than 1 second. Moreover, the change in surface energy occurs instantaneously. However, the surface energy does not seem to increase linearly as plasma exposure increases, as first thought. The surface energy has been shown to reduce in the initial plasma exposure, before increasing and reaching a maximum of 80 mJ/m^2.

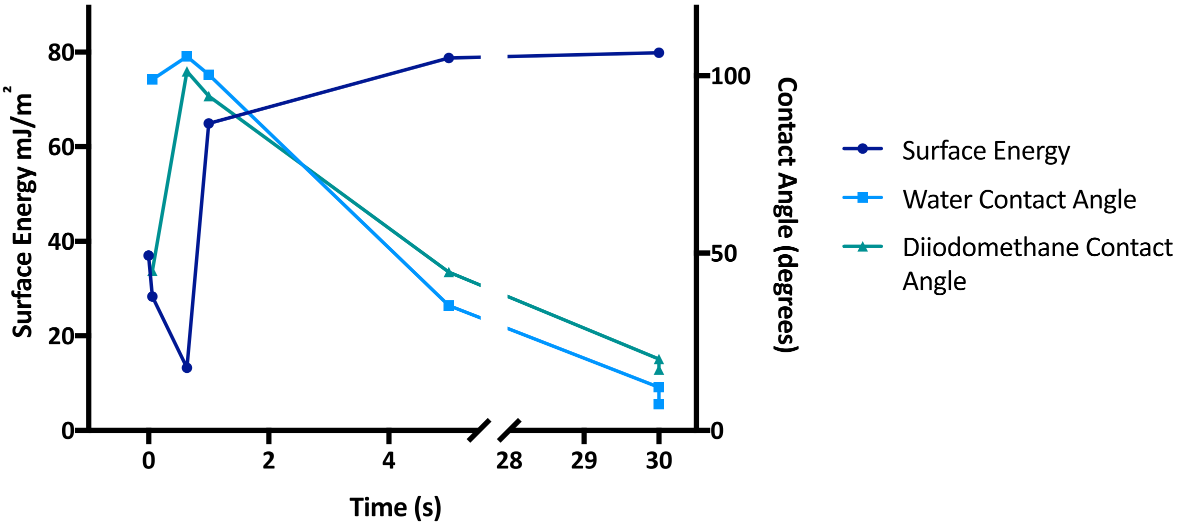

Figure 6.7 *Surface energy, water contact angle and diiodomethane contact angle change as plasma processing time is increased.*

This result shows that the plasma modification of PS is much more complex than first considered and that further surface chemistry analysis must be carried out to fully understand what is happening to the surface. Examining the literature, this change in water contact angle is said to be attributed to the addition of oxygen species to the polymer surface, characterised by XPS.[141, 143, 144, 146, 147]

It is hypothesised that in the first few seconds of plasma treatment, the change in surface energy and wettability is attributed to change in surface topography only. As time increases and the change in surface energy and wettability continues, this is possibly a result of both surface chemistry and surface topography. However, detailed XPS analysis would need to be carried out to determine this.

6.2.3 PS – *b* – PMMA annealing on modified brush layers

To get an understanding of how the plasma modified brush layer affects BCP orientation, PS – *b* – PMMA was annealed on three different brush layers - PS untreated, PS plasma treated and PS – *r* – PMMA a random copolymer (RCP). The RCP brush layer is widely used to orient cylindrical PS – *b* – PMMA perpendicular to the surface. [148, 149] PS is a preferential brush layer; therefore, it would be expected that the BCP would orient parallel to the surface. BCP were annealed on each brush layer and imaged with AFM to determine BCP orientations, see Figure 6.8. For the plasma treated brush layer, a short plasma treatment of 5s with 40W and 100mT was used. This was shown in previous experiments (Exp 3) to have a large effect on WCA and surface energy while not affecting surface roughness. For BCP annealing smooth brush layers are crucial. For this reason, this plasma process was chosen.

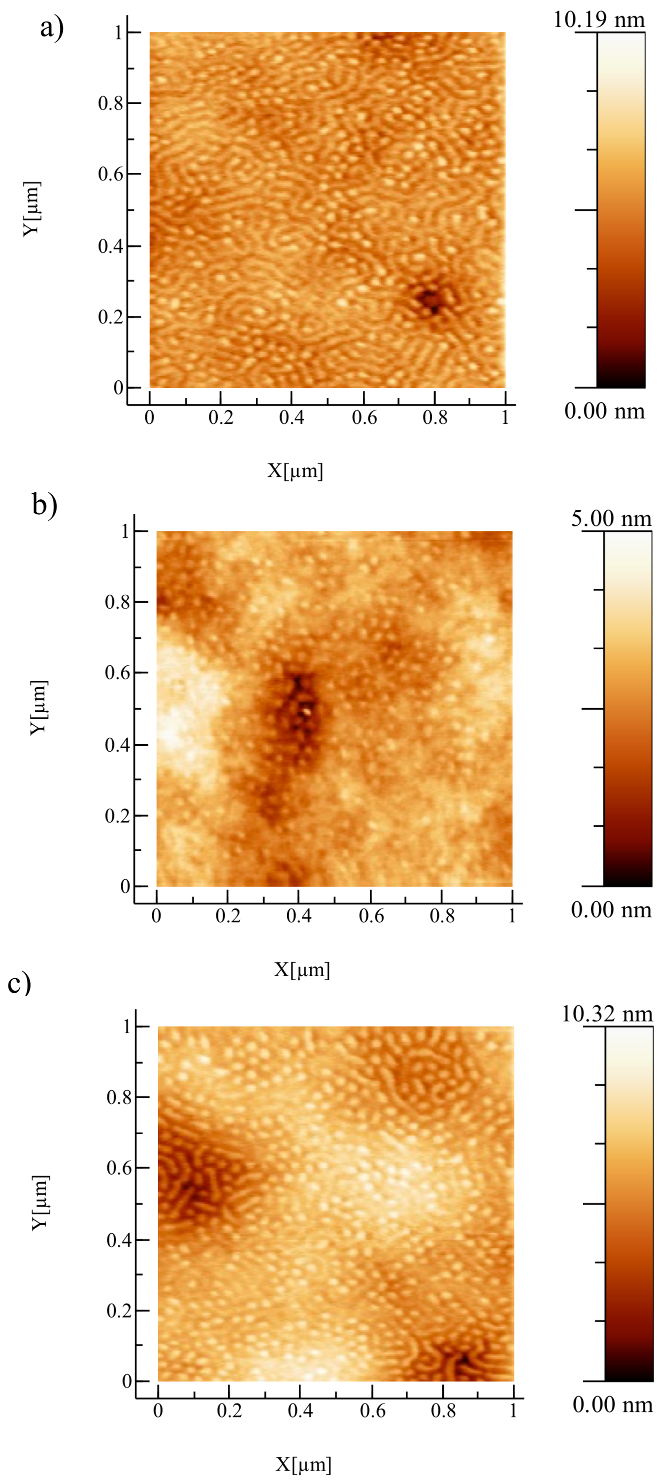

Figure 6.8 *Representative AFM height images of cylindrical forming PS – b – PMMA on a) untreated PS brush, b) plasma treated PS brush and c) random copolymer brush.*

From the AFM height images, it is clear that each brush layer produced a microphase separation BCP thin film. The PS brush layer in Figure 6.8 a) shows a mixture of parallel and perpendicular orientated cylinders, which is expected for this brush layer.

For plasma treated PS brush layer, the microphase separation appears to be improved with perpendicular cylinders clearly visible. Figure 6.8 c) shows the RCP brush layer anneal, again clear microphase separation is seen, however this brush layer is considered the ‘gold standard’ for perpendicular orientation of PS – *b* – PMMA. For this reason, better phase separation was expected, however perpendicular cylinders can be clearly see with a small number of parallel cylinders. This result corresponds to the work by Oria et al., where they achieved various BCP alignment using plasma treated PS brush layers.[140] Although the phase separation shown in each image is not optimal and must be further improved, this result is valuable for future work, as plasma treated brush layers are seen to influence BCP orientation when compared to the untreated PS brush layer.

6.3 Conclusion

The objective of the experiments described in this chapter was to modify a PS brush layer with oxygen plasma. The aim being to convert PS from a preferential brush layer to a neutral brush layer. By doing this, the orientation of BCP could potentially be controlled using plasma. In this chapter, a thorough investigation into oxygen plasma treatment of PS thin films has been carried out. Changes in wettability, surface energy and film thickness post plasma treatment have been recorded. Results show that treating PS brush layers with oxygen plasmas significantly changes the surface wettability and energy. Initial BCP annealing on plasma treated films have been carried out and results show that plasma treated PS brush layer influence PS – *b* – PMMA orientation.

6.4 Future Work

It is hypothesised that these changes in the surface could be attributed to oxidation during plasma treatment, however more surface analysis must be carried out to confirm this. ATR has been carried out to date, but results need to be investigated further using XPS to gain a full understanding of the surface chemistry. The most important question to answer is if the plasma treated brush layers are causing a change in BCP orientation. BCP anneals using these plasma-modified brush layers have been carried out but further BCP annealing with improved annealing conditions must be performed. This will give a better understanding in the effect plasma modified brush layer has on BCP orientation. This will be subject of future work.

Chapter Seven

7 Fabrication of silicon nanopillars through pattern transfer of PS – *b* – P4VP BCP template

7.1 Introduction

As mentioned in chapter one, nanostructured surfaces have been of interest of late due to valuable properties. Particularly, nanopillar surfaces have been shown to have antibacterial properties as well as drug delivery applications. [57, 73, 150, 151] Previous chapters have described detailed studies to prepared cylindrical BCP templates on silicon surfaces. These BCP templates can be pattern transferred into silicon to create silicon nanopillar arrays.[127] This chapter will describe the fabrication of silicon nanopillars and the study of the antibacterial effect of these surfaces. Moreover, once silicon nanopillars are fabricated, replica molding techniques can be used to prepare polymer replicas. Creating polymer replicas of such surfaces has numerous advantages. The unique properties of the polymer material can be exploited to control the nanostructured surface.

Before the fabrication and molding of silicon nanopillars was carried out, optimisation of molding protocols and handling of materials was optimised. This was done using a test material - nanostructured cicada wings. Nanostructured cicada wings have attracted attention recently due to their antibacterial properties, as described in chapter one.[57, 58, 150] The surface of the wings contain arrays of closely packed nanopillars, see Figure 7.1.

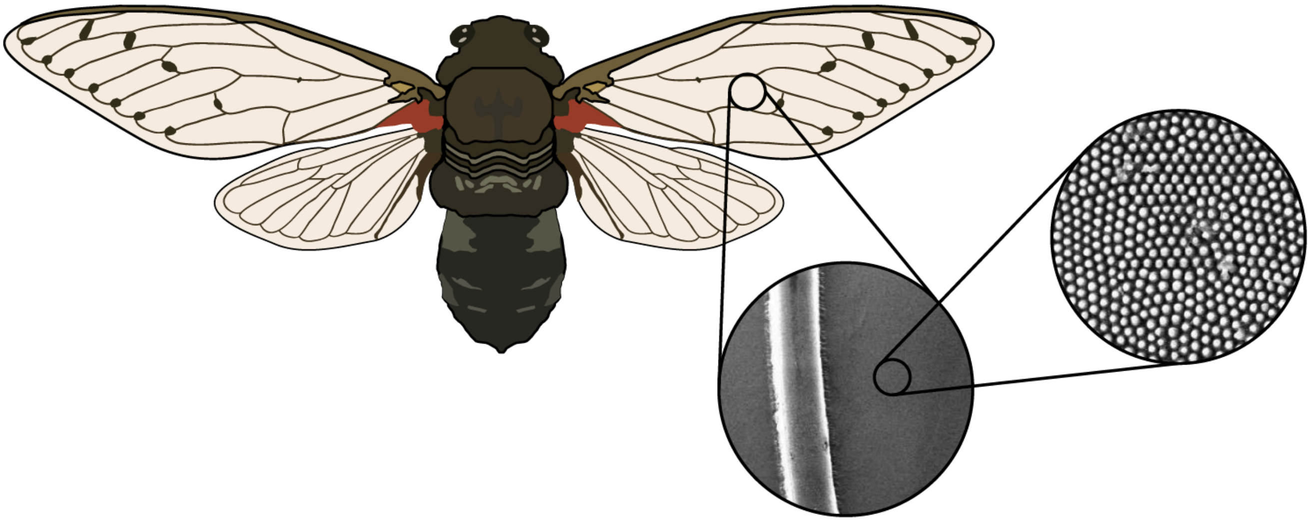

Figure 7.1 *Schematic of a cicada showing a SEM image of the nanopillar structures of the surface of the wings.*

This natural surface has already been characterised in the literature and within the research group.[59] Using a surface which is known to be uniformly nanopatterned will make it straightforward to determine if molding techniques are working adequately. Moreover, the features on cicada wings are slightly bigger (~250nm in height and ~160nm in diameter) than what we expect to produce using BCPs, using features at this scale will be less difficult, and techniques can be optimised before moving to sub-100nm replica molding.

As described in chapter one, replica molding is a technique which can be used to harness the unique properties of materials to create identical replicas. Using replica molding to reproduce bioinspired materials has been described in the literature, with gecko and shark skin replication reported.[152, 153] Hong et al. have fabricated nanopillar surfaces on silicon and glass using cicada wings. In their process, the wing was molded using hot embossing for form a polyvinyl chloride (PVC) secondary mold. This was in turn used as a UV- nanoimprint lithography template for the final nanostructured surfaces.[154] More recently, Xie et al. have replicated cicada wings using an electroplating process. In their work, the wings were coated in a conductive nickel layer by electroplating which was used to form a nickel secondary mold. This secondary mold was then used to create polystyrene replicas by melt injection of the secondary mold.[155]

The molding techniques used for these natural materials can also be transferred to silicon surfaces. Zhang et al. have reported a library of polymer nanopillars surfaces fabricated by replica molding of silicon masters. In their work, PDMS was used to fabricate a secondary mold by temperature curing. This was then molded using an epoxy resin to form identical replicas.[156]

The objective of this work was to fabricate polymer nanopillar arrays through replica molding of silicon masters, using cicada wings as a test substrate to optimise protocols. The replica process is described in Figure 7.2.

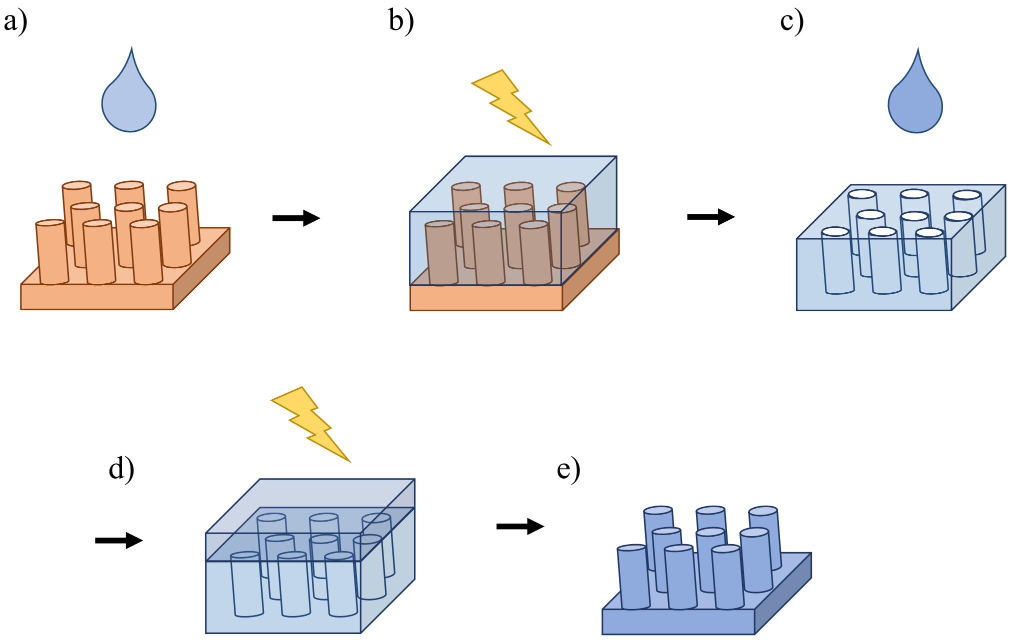

Figure 7.2 *Schematic representation of replica molding of cicada wings. a) the cicada wing is cast with PPGDA b) UV curing of PPGDA c) the primary mold is removed from the cicada wing. d) the primary mold is cast with PEGDA. e) the secondary mold is removed from the primary mold.*

Poly (propylene glycol) diacrylate (PPGDA) and poly (ethylene glycol) diacrylate PPGDA were chosen as molding materials for several reasons. Before UV-based photo polymerisation, the polymers are liquid which can be easily poured onto surfaces of interest. They are widely used for their high flexibility and reactivity. Furthermore, the fabrication process can be done at room temperature, without the use of solvent and with low energy consumption which makes them attractive for industry.[157-159]

Photoinitiated polymerisation of PPGDA and PEGDA enables crosslinking of the acrylate groups to form polymer networks, See Figure 7.3.

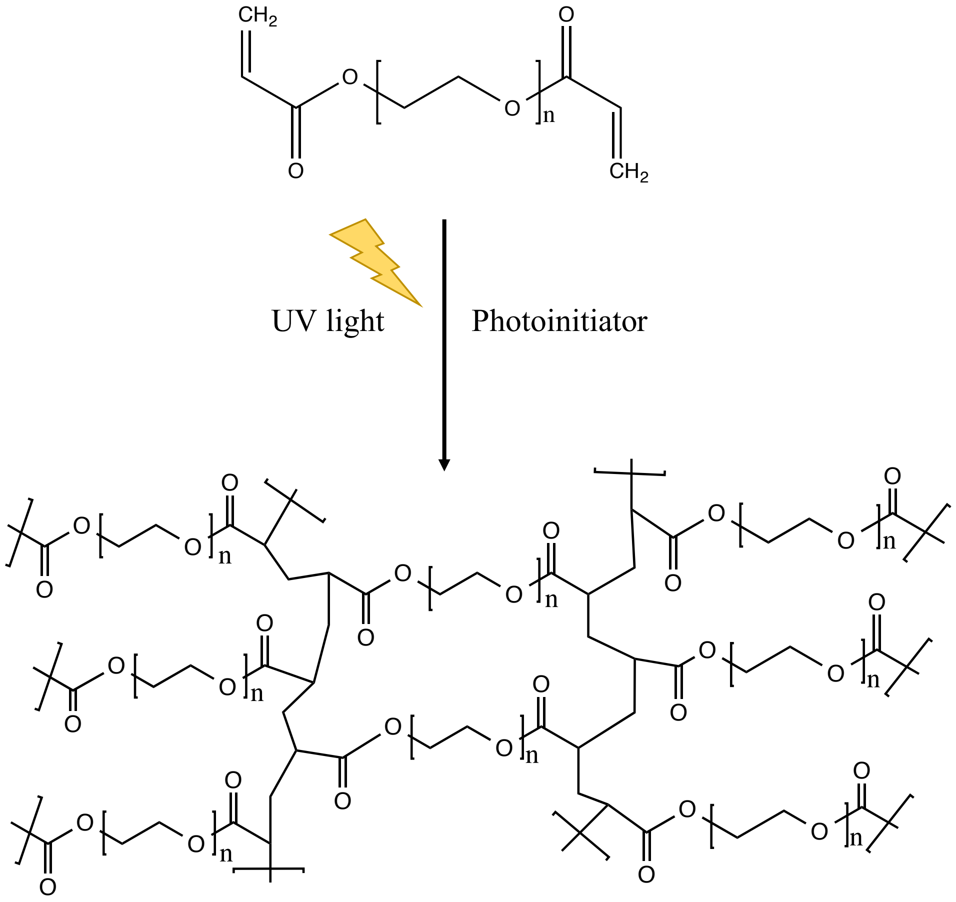

Figure 7.3 *Photoinitiated polymerization of PEGDA by UV curing resulting in a polymer network.*

The absorption wavelength of the photoinitiator corresponds to the wavelength of UV light which results in the generation of radical which start the crosslinking process. Monomers bind with one another to form a polymer network, resulting in a solid structure.[157] This process must be carried out in oxygen free environments due to oxygen inhibiting the cross-linking of the monomer. [160]

Moreover, PEGDA is well known for its ability to incorporate water into the polymer matrix to create gels with unique properties, such as swelling.[161, 162] A gel can be described as a three-dimensional cross-linked polymer network that does not dissolve in water, but can retain the liquid in a swollen state. Microstructured PEGDA gels have been shown to possess this property.[163] For these reasons, it was thought that the preparation of nanostructured PEGDA gels using cicada wings would result in a nanopillar surface that, when swollen, the size of the nanopillars could be adjusted and controlled, see Figure 7.4.

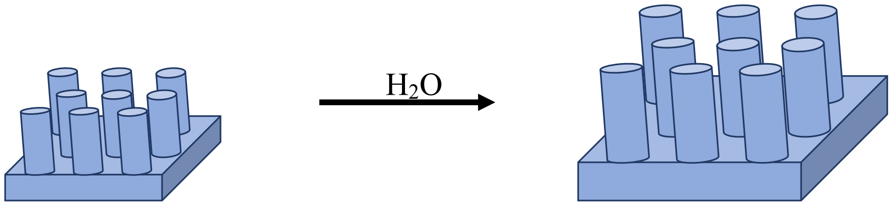

Figure 7.4 *Swelling of nanostructured gel by H_2O leading to increase in nanostructure size.*

To study this, nanopillar molds were prepared using PEGDA neat, PEGDA 20% H_2O and PEGDA 40% H_2O. To study the small changes in structure when swollen, molds would need to be characterised using AFM in both air and aqueous environments. By doing this, the change in nanopillar size during swelling could be easily noted. It is also important to characterise the polymer molds in aqueous environment, not only to see a significant change in the nanostructure, but for antibacterial testing, the samples are examined in aqueous environments. Therefore, investigating PEGDA nanopillars in such environment to confirm if the structures remain unchanged and stand upright was of interest. As PEGDA become swollen, the structure becomes soft and flexible, which could inhibit the antibacterial effect.

The gels were prepared using the cicada wing as a master and molded with PPGDA to create a primary mold. This primary mold was then used to create a secondary mold with PEGDA. PPGDA was chosen as the primary mold material as it has similar curing properties to PEGDA. Using different materials for primary molds and secondary molds creates easy separation of the primary mold and secondary mold.

The *Megapomponia Intermedia* cicada wing was chosen to be replica molded as this species has shown to have a high antibacterial effect when compare to other species.[59] Figure 7.5 a) shows a photograph of the insect b) the wing removed ready for molding, c) primary mold, and d) secondary mold.

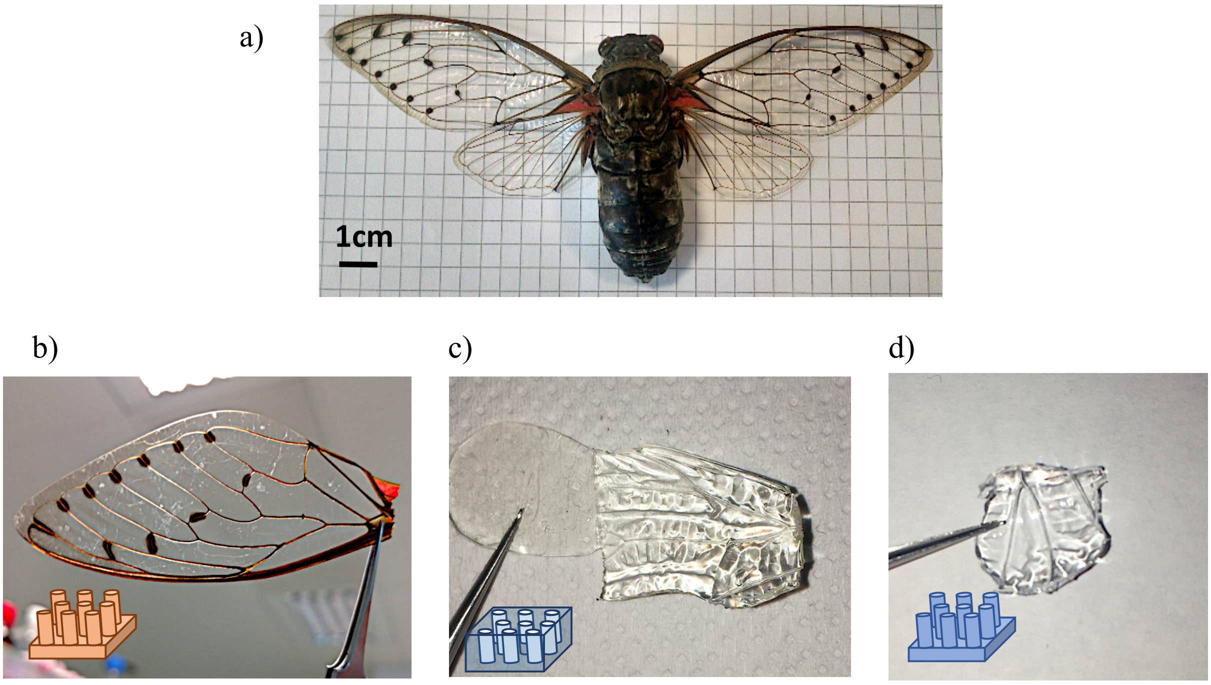

***Figure** 7.5 a) Photograph of Megapomponia Intermedia cicada. b) Cicada wing that has been removed from the insect for replica molding. c) Primary mold of cicada wing d) Secondary mold. The inset show a cartoon representation of the surface and relate to the schematic in Figure 7.2.*

7.2 Results and Discussion

Before molding was carried out, SEM characterisation of the cicada wings was performed. This was to determine that the wings were nanostructured, not damaged in places, and suitable to use as a master in the replica molding process. Figure 7.6 shows representative SEM images of cicada wings.

a)

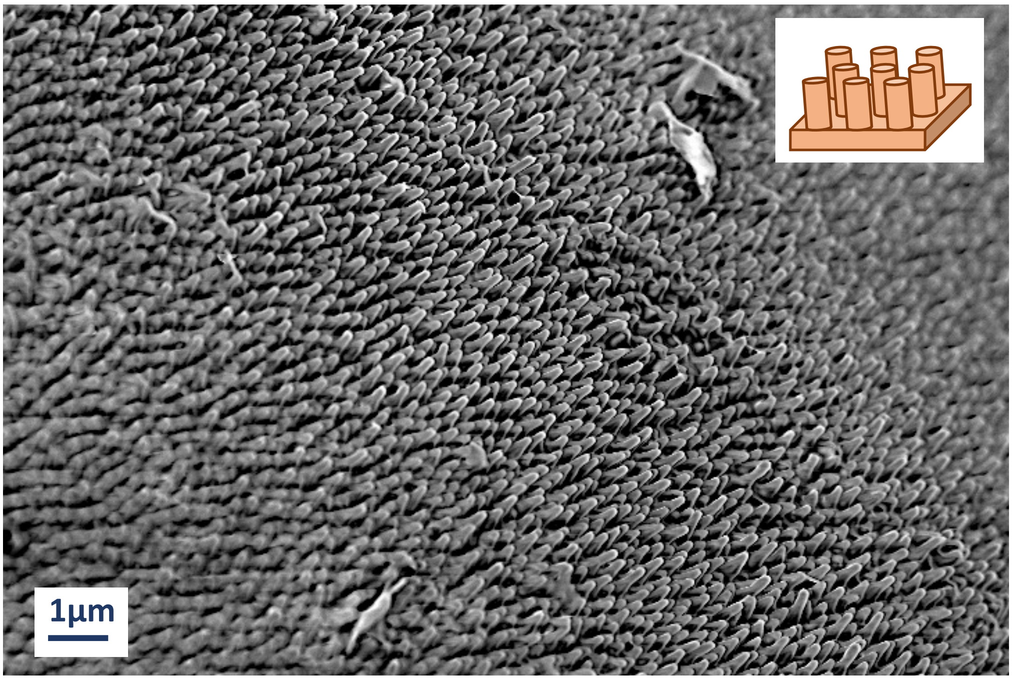

b)

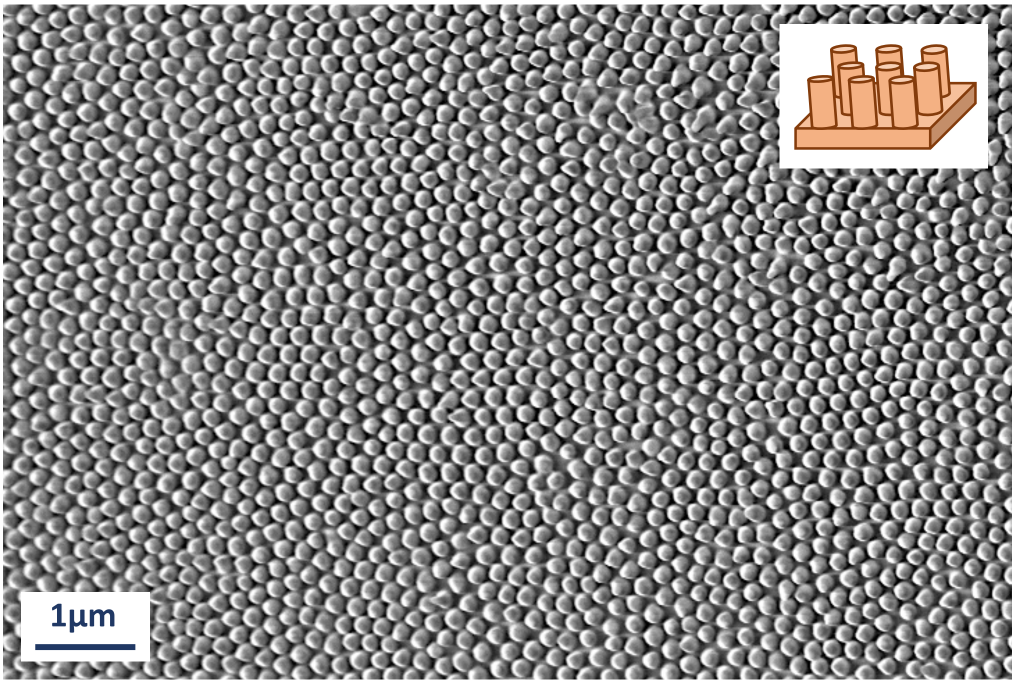

c)

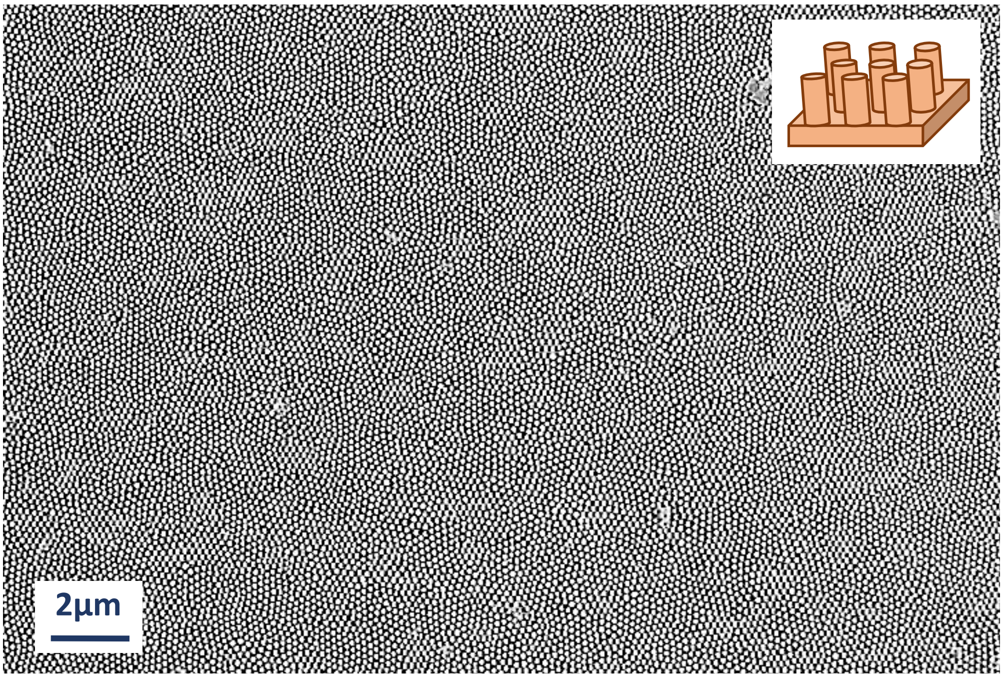

Figure 7.6 *SEM images of cicada wings showing arrays of nanopillar structures. a) shows tilt image of cicada nanopillars. b) and c) shown top down SEM image of cicada nanopillars. The inset shows a cartoon representation of the surface.*

The SEM images in Figure 7.6 show the nanopillar structures without any large-scale damage. The images were analysed using Image J software.[164] Particle analysis of the images, using the Feret Diameter measurement and nearest neighbour tool, confirmed the pillars had a diameter of 185nm ± 19nm and a pitch of 165nm ± 8nm. This compares to what was reported by Kelleher et al.[59] Figure 7.6 a) shows a tilt SEM image where the nanopillar structures can be clearly seen. Figure 7.6 b) and c) show top down SEM images of the cicada wing. Across the sample the nanopillars were seen to be ordered with little damage.

PPGDA primary molds were prepared employing the protocol outlined in the methods section. Figure 7.7 (a) shows a SEM image of a primary mold. To determine if primary molds could be reused, a mold was used three times to prepare secondary molds and then imaged to investigate damage, shown in Figure 7.7 (b)

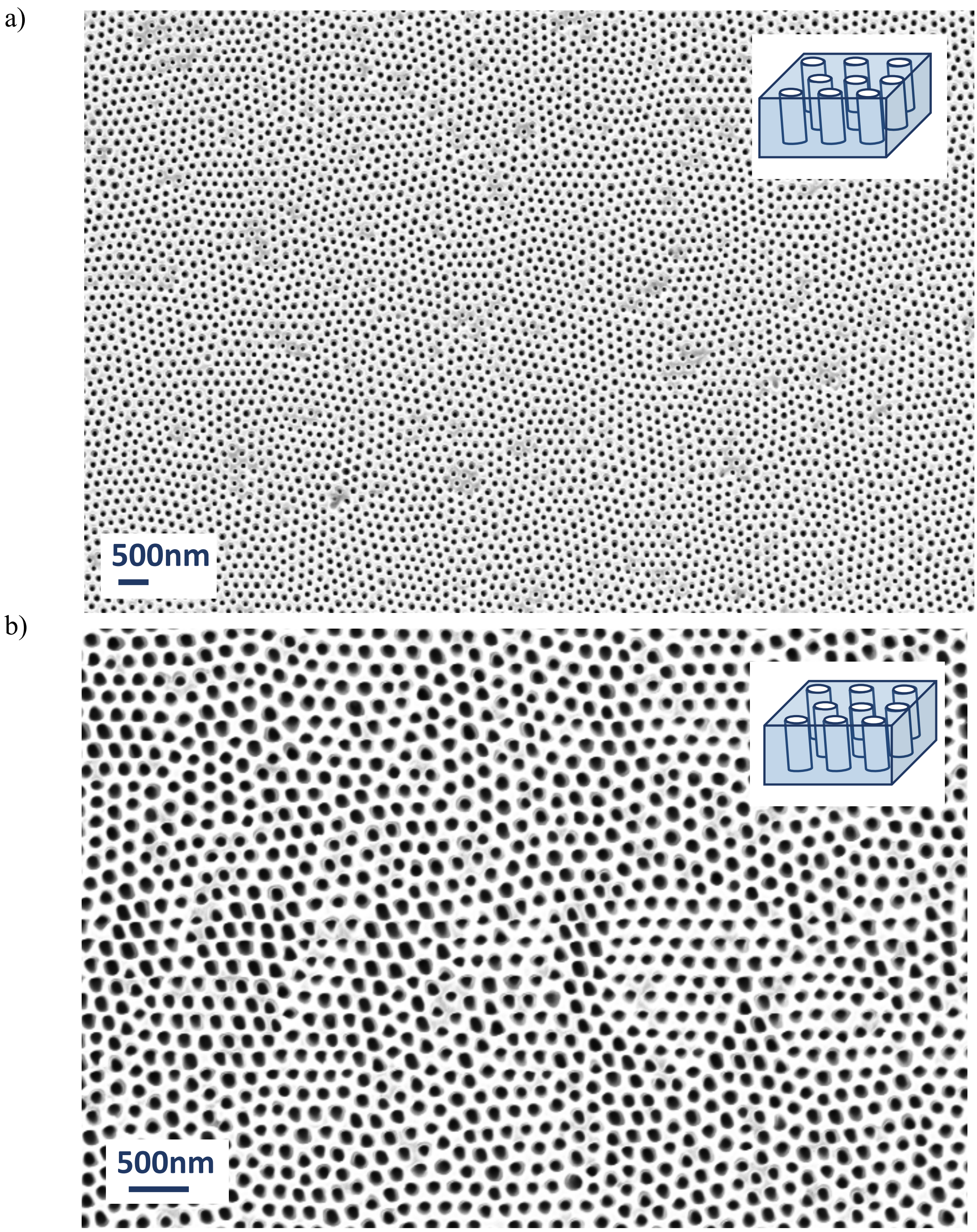

***Figure** 7.7 PPGDA primary molds fabricated using cicada wings a) unused primary mold b) used primary mold. The inset shows a cartoon representation of the surface.*

The SEM characterisation showed what was expected, namely widespread nanopores formed through molding of the cicada wings. Using Image J, the diameter of the pores was measured to be 152nm ± 27nm. The re-used primary mold shown in Figure 7.7 b) was comparable to the unused primary mold. After this finding, primary molds were considered reusable for up to three secondary molds. Once primary mold fabrication was confirmed through the above SEM, PEGDA neat, PEGDA 20% H_2O and PEGDA 40% H_2O molds were fabricated.

SEM characterisation was used to determine if molding was successful. Samples were coated with 10nm of gold before imaging. This made imaging easier, as creating a conductive layer of metal on the sample surface inhibits charging. The gold also provided protection of the polymer material from becoming thermally degraded by the electron beam. The images were analysed by Image J software, to determine nanopillar diameter and pitch. PEGDA neat produced pillars with a diameter of 149nm ± 41nm with a pitch of 152nm ± 19nm, PEGDA 20% H_2O produced a diameter of 160nm ± 27nm with a pitch of 161nm ± 12nm, and PEGDA 40% H_2O produced 158nm ± 48nm diameter pillars with a pitch of 169nm ± 11nm. SEM images are representative over large areas. Molds showed adequate replication of cicada wing masters with nanopillar arrays observed across samples, see Figure 7.8.

a)

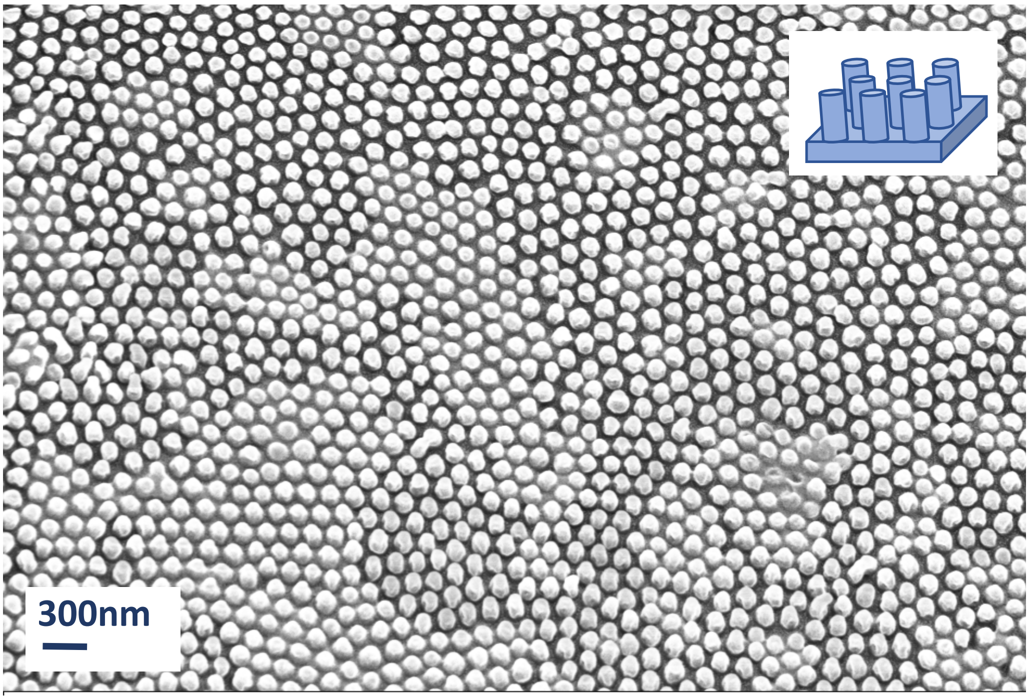

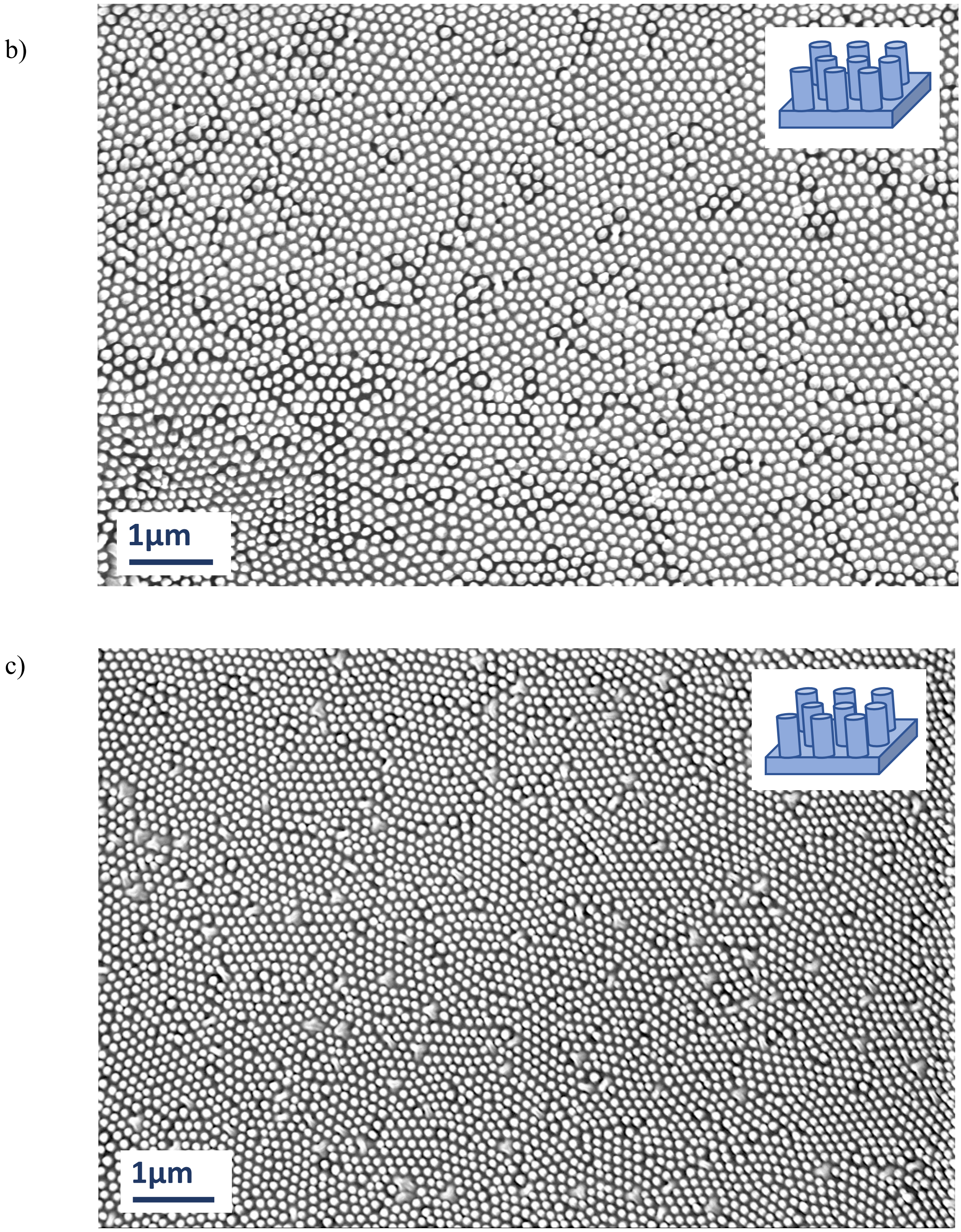

Figure 7.8 *SEM images of a) PEGDA neat secondary mold, b) PEGDA 20% H_2O secondary mold and c) PEGDA 40% H_2O secondary mold. The inset shows a cartoon representation of the surface.*

This SEM analysis has allowed the determination of diameter and pitch. However, to determine accurate height, AFM characterisation was carried out. AFM characterisation is shown in Figure 7.9. Samples were imaged in tapping mode with silicon probes with a force constant of 40 N/m and a resonant frequency of 300 kHz.

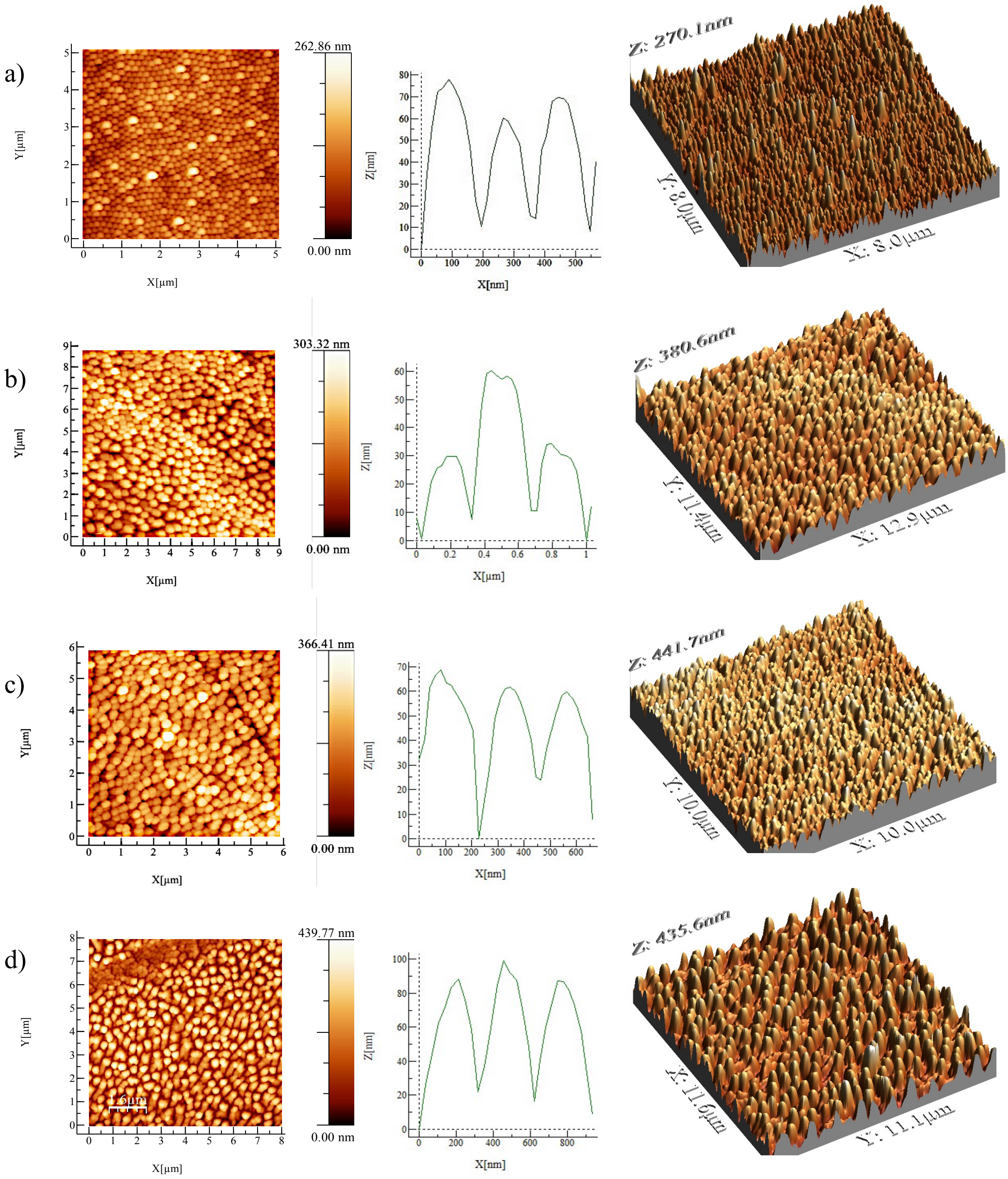

***Figure 7.9** a) AFM characterisation of cicada wing masters b) PEGDA neat mold, c) PEGDA 20% H_2O and d) PEGDA 40% H_2O. All AFM images are representative of large areas.*

For height calculations, a minimum of three different images were taken with AFM and the average height was calculated using the histogram height distribution function in the WxSM software. Figure 7.9 a) shows AFM characterisation of the cicada wing master. The height average height measured was 220nm with a diameter about 180nm, which was in line with what was calculated from the SEM images. Figure 7.9 b) shows AFM characterisation of the PEGDA neat polymer mold. The average height measured was 180nm. Figure 7.9 c) shows AFM of PEGDA 20% H_2O, with an average height measuring 191nm. Figure 7.9 d) shows AFM of PEGDA 40% H_2O with an average height of 181 measured. The diameter of the pillars shown in each height profile of the polymer molds appear larger than what was recorded from the FESEM images.

It is important to consider the physical limits of AFM. Due to the curvature of the AFM probe, measurement in the X and Y directions are not completely accurate. Therefore, the diameter shown here may not be a clear representation of the mold. For this reason, the diameters calculated from the SEM images were taken as an accurate representation. For comparison of sizes, the diameter, height and pitch have been listed in Table 7.1

Table 7.1 *Comparison of feature sizes between cicada wings and molds*

Measurement	**Cicada Wing**	**PEGDA Mold**	**PEGDA 20% H_2O Mold**	**PEGDA 40% H_2O Mold**
Diameter in nm (SEM)	185 ± 19	149 ± 41	160 ± 27	158 ± 48
Height in nm (AFM)	220	180	191	181
Pitch in nm (AFM)	165 ± 8	152 ± 19	161 ± 12	169 ± 11

The key information here is that the molds are shown to have features in the same scale as the cicada wings, confirming that the replica molding process has been successful.

To investigate the change in feature size when in a swollen state, liquid AFM was carried out. This allows for the polymer to be imaged in an aqueous environment, in this case, water. Before liquid AFM was performed, it was important to consider how the polymer molds were expected to swell in an aqueous environment. The Flory-Rehner equation describes mixing of polymers in solutions to create gels. In a hydrophilic polymer network system like PEG, water can act as a plasticiser. Therefore, the swelling process of the gel can be described as the free energy of mixing (ΔG_{mix}) from the polymer and the solution interaction, and the elastic free energy ($\Delta G_{elastic}$) from the crosslinked network, described in equation (7.1). [165]

$$\Delta G_{system} = \Delta G_{mix} + \Delta G_{elastic} \qquad (7.1)$$

When swelling is initiated, $\Delta G_{mix} << 0$, $\Delta G_{elastic} > 0$, giving $\Delta G_{mix} + \Delta G_{elastic} < 0$, so swelling is favoured and the solvent diffuses into the polymer network. During the swelling process, ΔG_{mix} and $\Delta G_{elastic}$ both increase until an equilibrium is reached, giving $\Delta G_{system} = \Delta G_{mix} + \Delta G_{elastic} = 0$. When this occurs, the driving force for swelling is eliminated and swelling ceases.[166] In order to estimate the change in size in each gel (polymer mold), the swelling ratio of unpatterned PEGDA gels was determined. The swelling ratio is a function of the mass of the gel swollen ($M_{swollen}$) and the mass of the gel dry (M_{dry}) and can be calculated using the following equation (7.2).

$$\text{Swelling Ratio} = \frac{\text{Mswollen} - \text{Mdry}}{\text{Mswollen}} \text{ X } 100 \qquad (7.2)$$

Unpatterned PEGDA, PEGDA 20% H_2O and PEGDA 40% H_2O gels were prepared. M_{dry} was recorded after polymer curing. To determine when the polymer reached the maximum swollen state, the gel was then placed in water and $M_{swollen}$ was recorded by removing the gel from the water, blotting dry with kim wipes and weighing at 30 minute intervals. The swelling ratio was then calculated. Results are displayed in Figure 7.10.

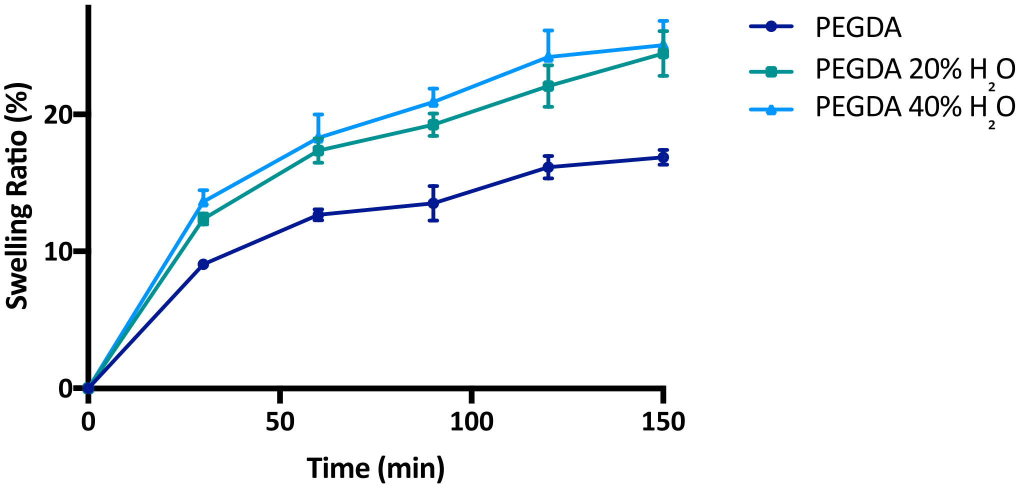

Figure 7.10 *Swelling ratio of PEGDA, PEGDA 20% H_2O and PEGDA 40% H_2O gels over 150mins.*

From the swelling experiments represented in Figure 7.10, it can be clearly seen that the gels swell and incorporate water into the polymer matrix. After 150 minutes the swelling starts to stabilise. The PEGDA gel swelled 16% over the 150 minutes. PEGDA 20% H_2O and PEG 40% H_2O gel had similar swelling characteristics with PEGDA 20% H_2O swelling ratio being 24% after 150 minutes and PEGDA 40% H_2O only being slightly higher at 25%. It is clear from this result that at 120 minutes the gels begin to reach a swollen state, after which no significant swelling is observed. These swelling ratios correlate to what was reported by Kelleher et al. In their work, using PEGDA neat, PEG 5% H_2O and PEGDA 10% H_2O, they calculated swelling ratios of 28.3%, 22.7% and 18.1%, respectively. [163]

To ensure the patterned gels were in a swollen state before liquid AFM was carried out, the samples were immersed in water for 150 minutes before imaging. The physical challenges of characterising gels with AFM in liquid must be considered. As the gel becomes swollen, the polymer sample will become soft and supple. For this reason, AFM probes with low force constants (0.5 N/m) were used to prevent damage of the surface during scanning. Probes with low force constants are flexible, allowing for movement in liquid.

Initial liquid AFM was performed in collaboration with NASA Ames Research Center using a Bruker Multimode tool equipped with a Veeco flow cell, described in chapter one. The process proved very difficult as the O-ring on the flow cell led to sample damage and leaking. Limited sample imaging could be performed using this set-up. Due to this, liquid AFM was then attempted using an Asylum research MFP-3D AFM. This is an open system, that does not require a flow cell for imaging. Therefore, using this set-up, the breakage associated with the O-ring could be avoided. The samples were imaged using this tool, however, the samples surface became damaged by the probe even when using very light tapping conditions. Another attribute observed was that the polymer nanopillars began to move during imaging in the liquid, resulting in unclear images. It was these factors that hindered image resolution during liquid imaging.

Figure 7.11 shows representative AFM height images of PEGDA gels in a water environment. The height profile of air AFM and liquid AFM were overlaid and shown in Figure 7.11 (right)

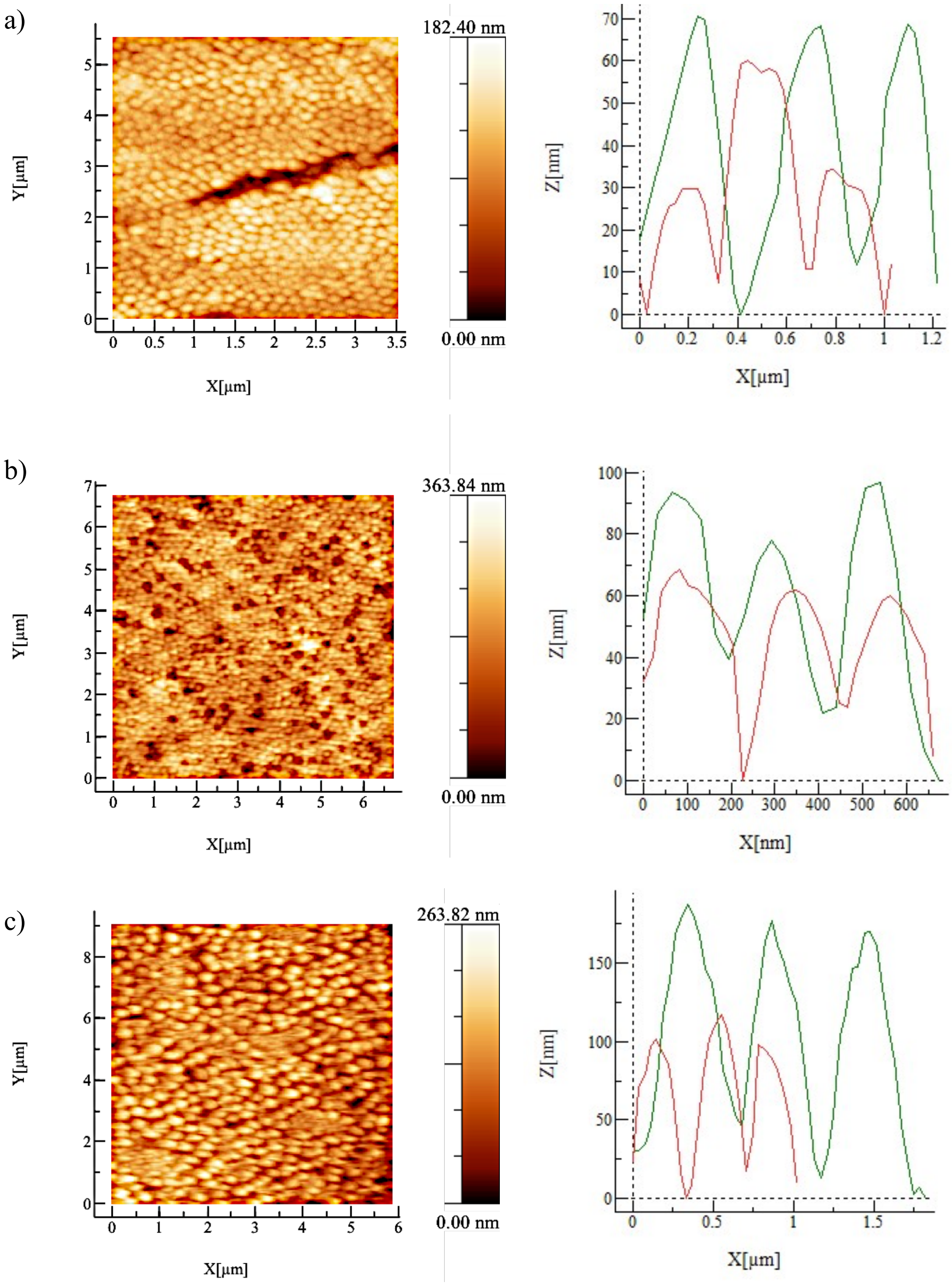

Figure 7.11 *Liquid AFM height images of a) PEGDA b) PEG 20%* H_2O *and c) PEG 40%* H_2O*. with each height profile of air AFM (red) and liquid AFM (green).*

For accurate height calculations, a minimum of three different images were taken with AFM and the average height was calculated using the histogram height distribution function in the WxSM software. The height profiles shown in Figure 7.11 illustrate the influence the swelling has on the nanopillar dimensions. Table 7.2 show a comparison of the height recorded in air AFM and liquid AFM. Each nanostructured gel has increased in height. The PEGDA mold has increased by 50nm to a height of 230nm, resulting in a 28% increase. Likewise, PEGDA 20% H_2O mold has increased to 285nm, showing a 49% increase in height. The PEGDA 40% H_2O mold shows the most significant change in structure with pillars increasing from 181nm to 390nm, showing a 115% increase in height. This finding is noteworthy, as it has been demonstrated that the nanopillar height and diameter can be controlled by exploiting the properties of gel and liquid.

Table 7.2 *Comparison of nanopillar height recorded by air AFM and liquid AFM.*

Measurement	**PEGDA Mold**	**PEGDA 20% H_2O Mold**	**PEGDA 40% H_2O Mold**
Height (Air AFM)	180nm	191nm	181nm
Height (Liquid AFM)	230nm	285nm	390nm

These changes in feature size correlate to what was reported by Kelleher et al. Their work used blends of PEGDA and 8-arm PEG acrylate to fabricate micropatterned trench structures for application is cell adhesion. They reported significant changes in features size after upon swelling of the polymer blend.[167] Knowing how these pillars react in aqueous environment will be beneficial for further studies where such materials need to be used aqueous environments, such as bacterial testing.

Once molding protocols have been optimised using the test substrate, molding of silicon nanostructures was be carried out. The silicon nanopillars were fabricated using a microphase BCP as a template. Although BCPs are valuable for creating a nanopattern on silicon substrates, they are of limited use for nanofabrication in their original state, due to the lack of etch contrast. The blocks must be converted into on-chip hard masks, that will allow the features generated by the BCP to be transferred onto the substrate material. Discussed at length in chapter one is numerous methods to achieve this. In this work, the selective inclusion of iron nitrate into the P4VP cores, in a cylindrical forming PS – *b* – P4VP, will be investigated. The aim was to prepare an iron oxide nanodot array, which could be used as a hard mask to fabricate a silicon nanopillar array. These nanopillars would then be replica molded, using the process optimised previously, to prepare polymer nanopillars. The polymer nanopillars could then be tested for antibacterial activity. The process steps needed to be completed in this chapter are outlined in Figure 7.12.

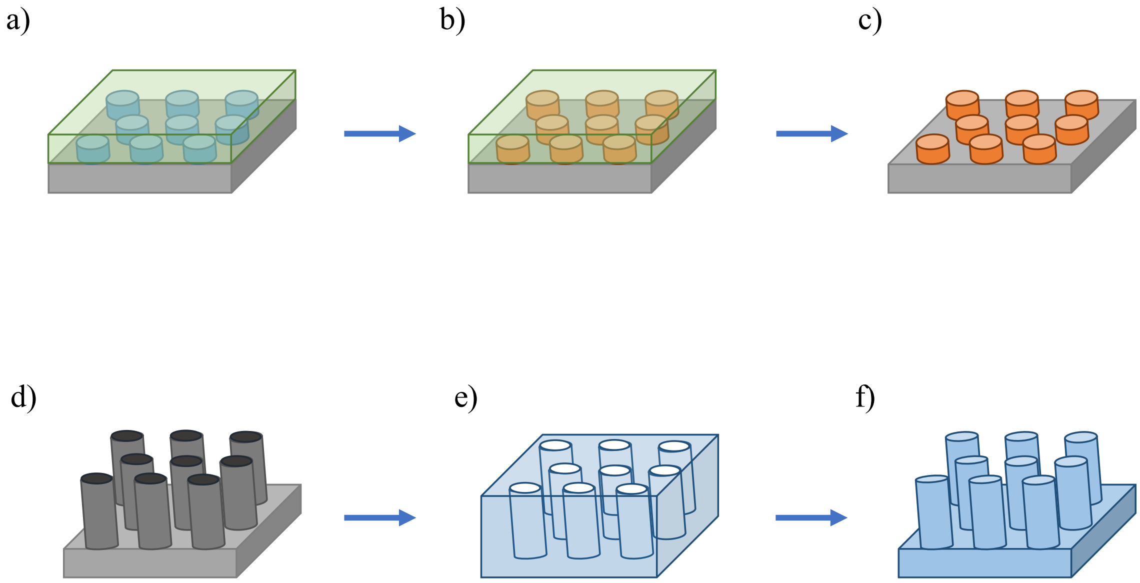

***Figure** 7.12 Schematic representation of process to be carried out to prepare polymer nanopillar array. a) Prepare microphased PS – b – P4VP, b) iron nitrate inclusion, c) UV/*O_3 *treatment to generate iron oxide nanodots (hard mask material), d) dry etch process to generate silicon nanopillars, e) preparation of primary mold using silicon master, f) preparation of secondary mold to generate polymer nanopillar array.*

The process began by solvent annealing PS – *b* – P4VP to produce perpendicular orientated cylinders. This was done using the solvothermal annealing chamber optimised in chapter four. In the interim, the solvothermal annealing chamber was further upgraded by a fellow PhD student to allow for improved films. The main upgrades included the following:

1. And *in situ* reflectometer installation to allow film thickness measurements to be captured during the annealing process
2. Use of a thermoelectric module embedded within the annealing stage for precise temperature control that allows both stage heating and cooling. This eliminated issues associated with radiant heating of the annealing stage.
3. Sensors calibrated to within 0.1 ºC for each temperature probe.

These upgrades led to the solvent temperature and substrate temperature to be highly controlled during annealing, leading to high S values. Implementing a rapid quench step, which could be monitored using the *in situ* reflectometer improved hexagonal ordering. The BCP films were characterised with SEM, results are shown in Figure 7.13. PS – *b* – P4VP thin film was reconstructed with ethanol before imaging.

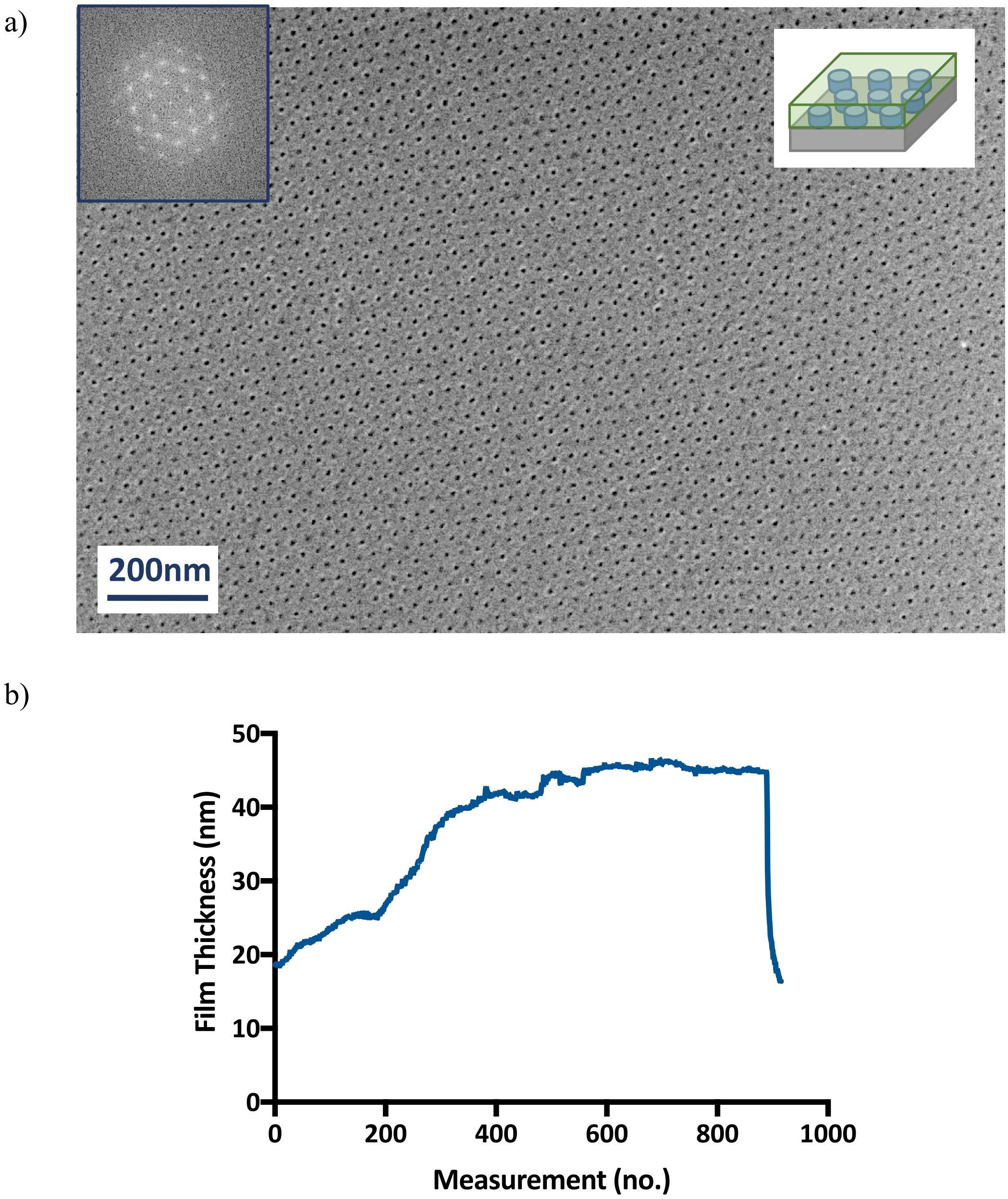

***Figure 7.13** a) SEM images of PS – b – P4VP film which was solvent annealed in the upgraded solvothermal annealing chamber. The inset shows a cartoon representation of the surface. b) Film thickness measurements taken using the in situ reflectometer.*

The SEM image showed a BCP film was fabricated containing hexagonal ordering of the P4VP cores, with little to no defects seen across the samples. Image J analysis of the SEM image, by converting to binary and the Feret Diameter measurement, confirmed the pores had a diameter of 18nm ± 2nm and a pitch of 21nm ± 1nm. Figure 7.13 b) shows the *in situ* reflectometer measurements of the BCP thin film; measurements were taken every 2 seconds during the 30 minute anneal. The results show a starting film thickness of 18nm, which increases to 45nm during the anneal, before returning to 18nm at the nitrogen purge step. This shows a film swelling of 250%, allowing for adequate microphase separation before the film was purged with nitrogen gas. S value calculated were 0.98. AFM characterisation was carried out also and is shown in Figure 7.14.

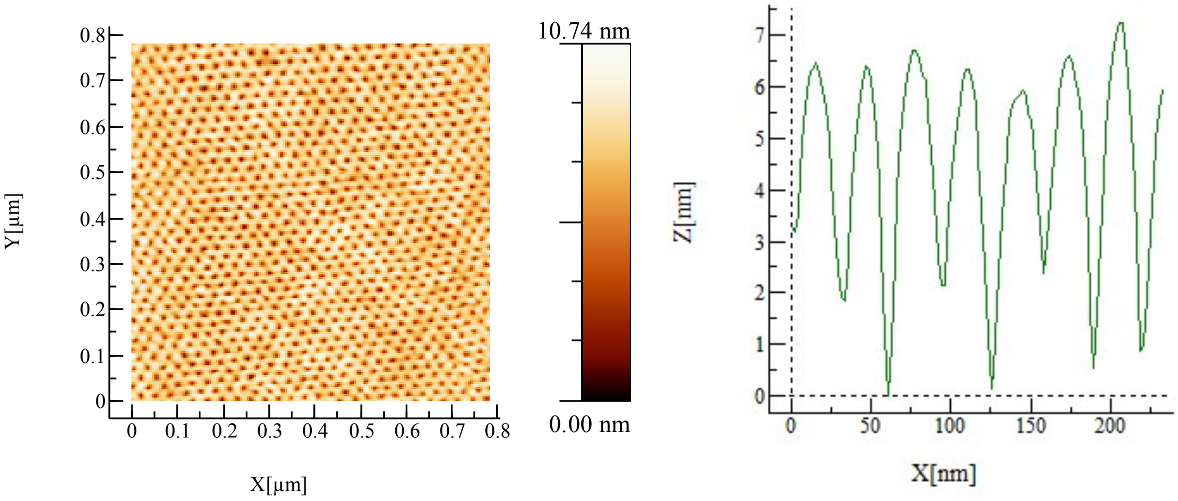

Figure 7.14 *AFM height image and profile of ethanol reconstructed PS- b – P4VP.*

The AFM characterisation confirmed what was observed in the SEM analysis. The PS – *b* – P4VP film showed excellent hexagonal ordering with no defects. The profile analysis showed pores of equal pitch and diameter, similar to what was recorded with the SEM analysis. The Z scale measured with AFM appears smaller than what was recorded using the reflectometer. This is due to the physical limits of the AFM probe. The tip will not reach the bottom of the pore to get an accurate measurement. This is due to the pore size being so small, hence the Z scale is smaller in AFM than the reflectometer measurement.

Once characterisation confirmed that the BCP patterns were suitable for pattern transfer, the inclusion process was carried out. Transforming these surface patterns to a hard mark material was achieved by an iron nitrate inclusion step. The inclusion method is described in detail in chapter three. This process allowed the P4VP cores to be selectively infused by the iron nitrate salt. Once inclusion was performed, the films were treated with UV/O_3 for 3 hrs. This converted the nitrate to an oxide and to degrade the polystyrene matrix, generating an iron oxide nanodot array. The iron oxide nanodots were then characterised with SEM and AFM to confirm hard mask formation. Results are shown in Figure 7.15.

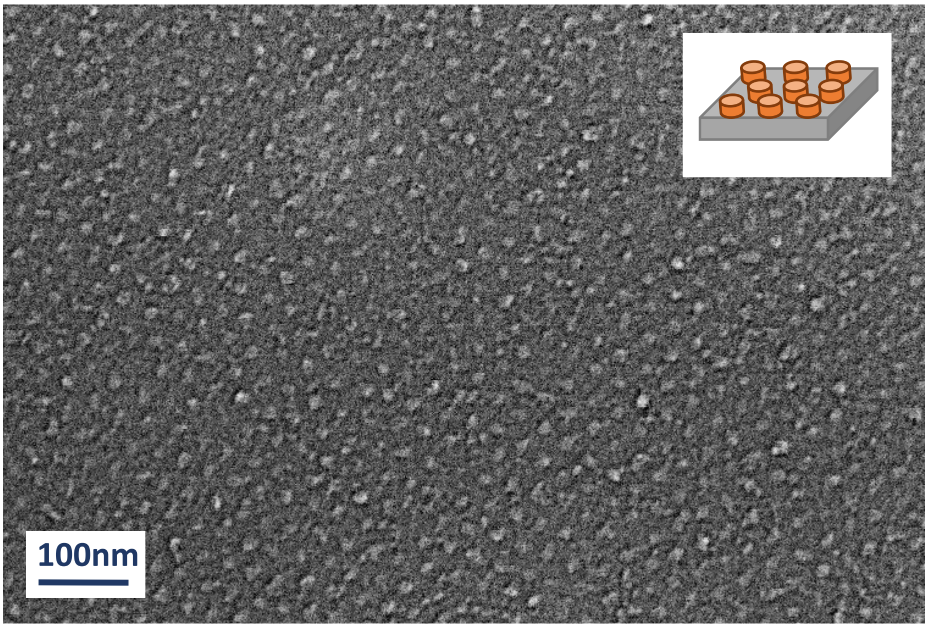

Figure 7.15 *SEM images of iron oxide nanodot array fabricated by an inclusion process to PS – b – P4VP film. The inset shows a cartoon representation of the surface.*

The SEM analysis confirmed that the BCP pattern had been converted into a nanodot array. It must be noted that to confirm oxide formation, XPS analysis would need to be carried out. Since this inclusion process and UV/O_3 treatment is routinely done in the literature to prepare iron oxide,[46] we can assume that the oxide has been formed. AFM characterisation was performed on the hard mask array to determine nanodot feature size, see Figure 7.16.

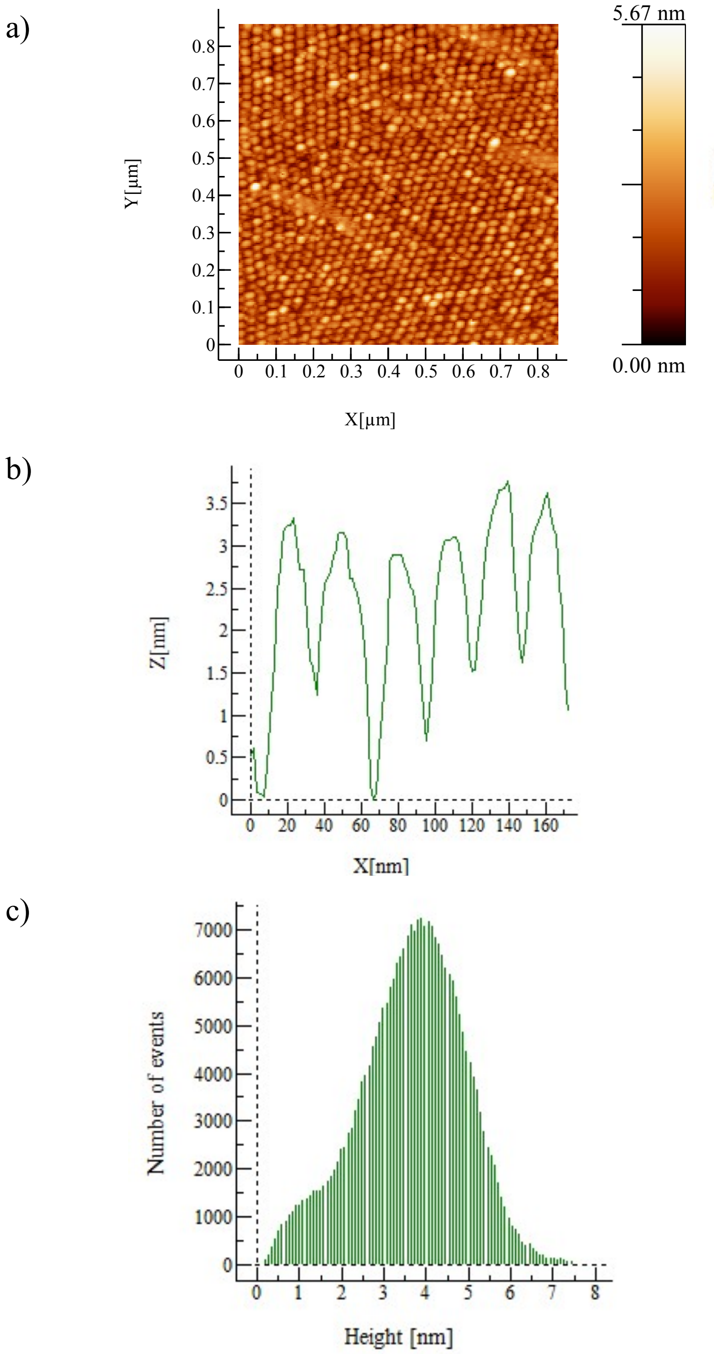

Figure 7.16 *AFM characterisation of iron oxide nanodot array. a) height image of iron oxide nanodot array, b) profile showing heights between 2.5 and 3.8nm with a pitch of 21nm, and c) histogram showing the range of nanodot height across the imaged region.*

The AFM analysis confirmed that the iron oxide nanodot arrays had similar feature size as the BCP template. This was expected, and confirmed that the inclusion process was successful. It was also shown that the nanodots have an average height of 4nm.

These dimensions corroborate to the feature size of iron oxide nanodots prepared by PS – *b* – P4VP inclusion reported in the literature.[46] A comparison of the BCP template and iron oxide nanodots array is shown in Table 7.3

Table 7.3 *Comparison of BCP template and iron oxide nanodot array*

Measurement	**P4VP core**	**Iron Oxide Nanodots**
Height	18nm (measured by reflectometer)	4nm (measured by AFM)
Diameter	18nm ± 2nm	22nm ± 5nm
Pitch	21nm ± 1nm	25nm ± 3nm

The next step in the process was etching of the samples to form silicon nanopillars. This was carried out by Tyndall National Laboratory. The samples underwent a silicon etch using C_4F_8 and SF_6 gases. Sample 1 was etched for 30s while sample 2 was etched for 1 min. The aim was to generate two surfaces with different height nanopillars, ranging between 50-100nm. Once the samples were received back from Tyndall after undergoing etch processing, SEM analysis was carried out to determine nanopillar size, Figure 7.17 shown SEM characterisation for samples 1.

a)

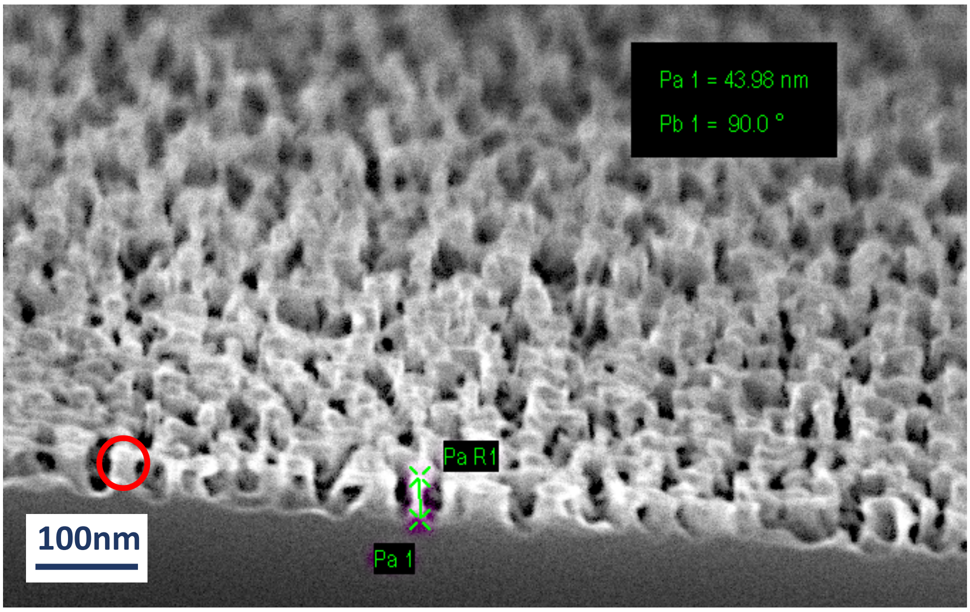
Pa 1 = 43.98 nm
Pb 1 = 90.0 °
Pa R1
Pa 1
100nm

b)

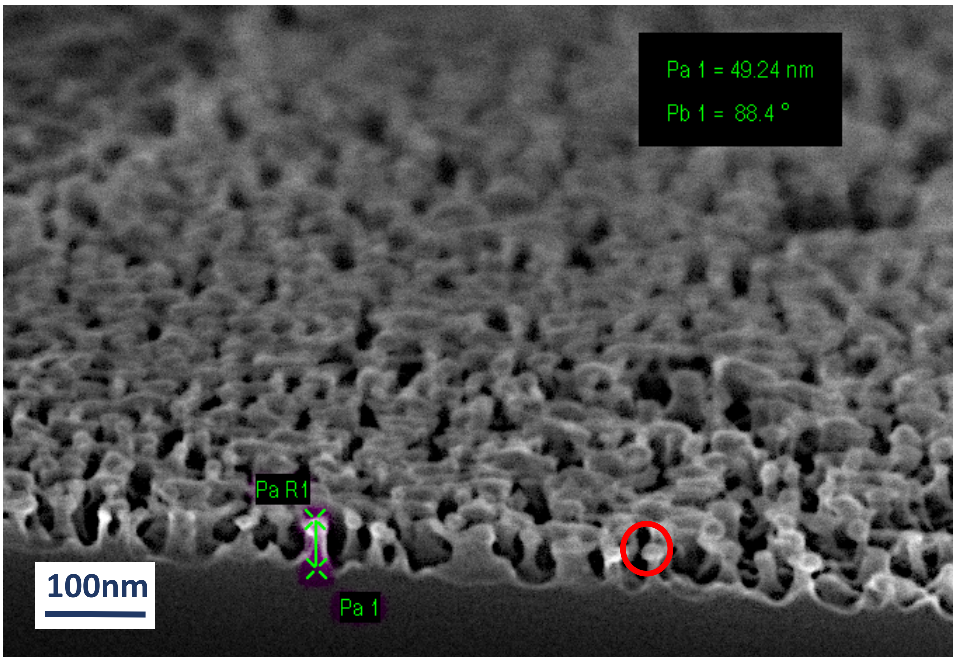
Pa 1 = 49.24 nm
Pb 1 = 88.4 °
Pa R1
Pa 1
100nm

c)

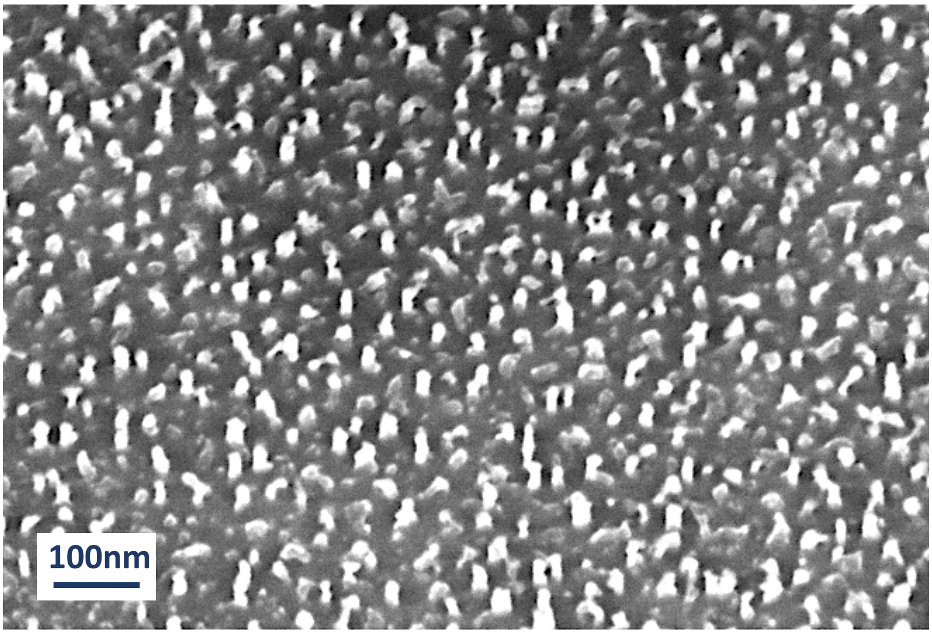

Figure 7.17 FESEM characterisation of etched iron oxide nanodots (sample 1). Tilt FESEM images taken at the sample edge are shown in a) and b) Iron oxide caps are marked with red circles. c) shown a FESEM image taken from the centre sample. The substrate was snap cleaved along the centre to get a clear representation of the nanopillars.

The SEM characterisation, displayed in Figure 7.17, confirmed the nanopillar formation for sample 1. The sample surface was not as expected. Figure 7.17a) and b) show the sample contains nanopillars around ~50nm, however the pillars look over-etched and with isotropic properties, meaning the silicon was not etched vertically to create straight pillars. The iron oxide nanodot cap on the top of the pillars can be clearly seen in a) and b) (marked with red circle) which indicated strong etch resistance of this hard mask material. Figure 7.17c) shows the that the surface is not uniform, the nanopillars are sparse and they are not in hexagonal arrays. Samples 2 SEM characterisation is shown in Figure 7.18.

a)

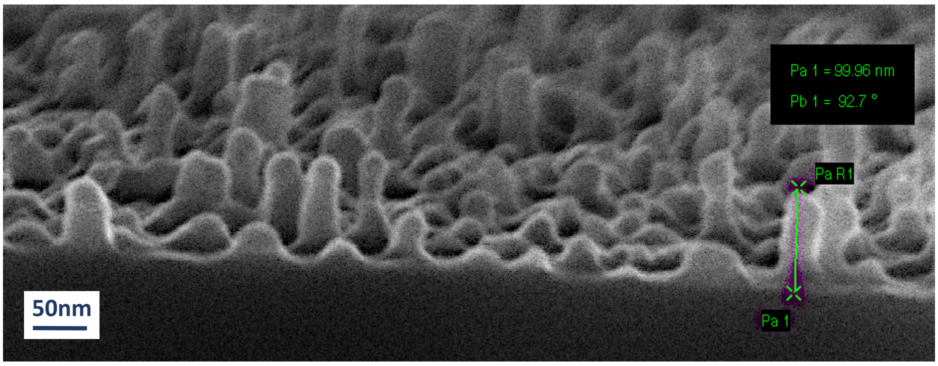

b)

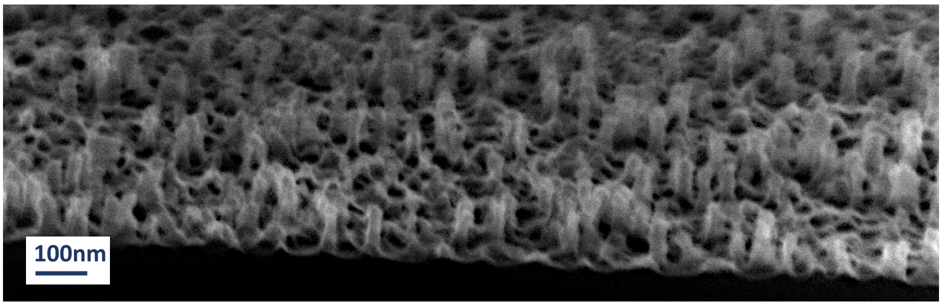

c)

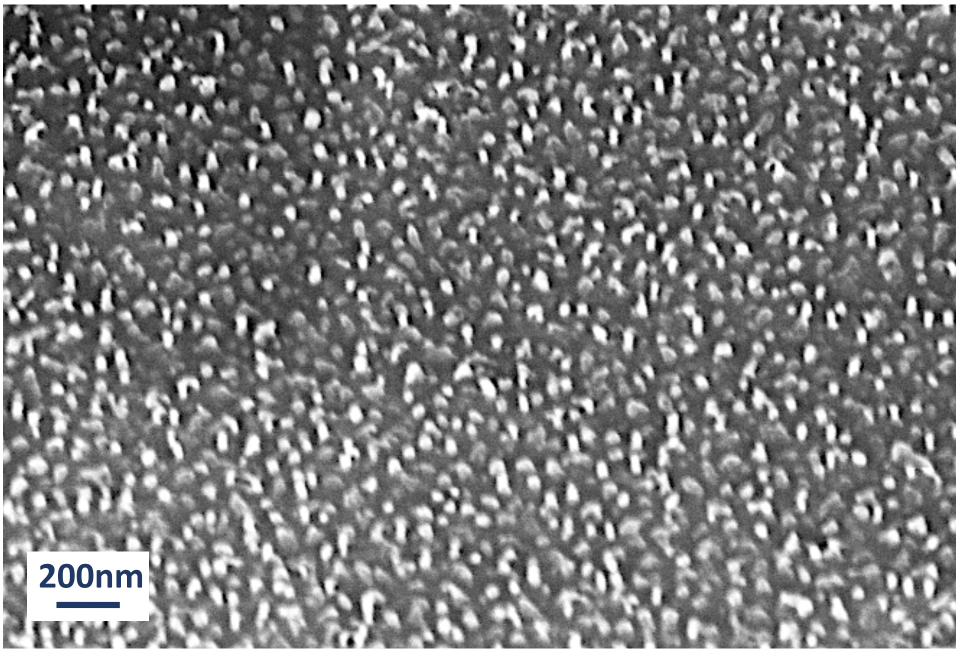

d)

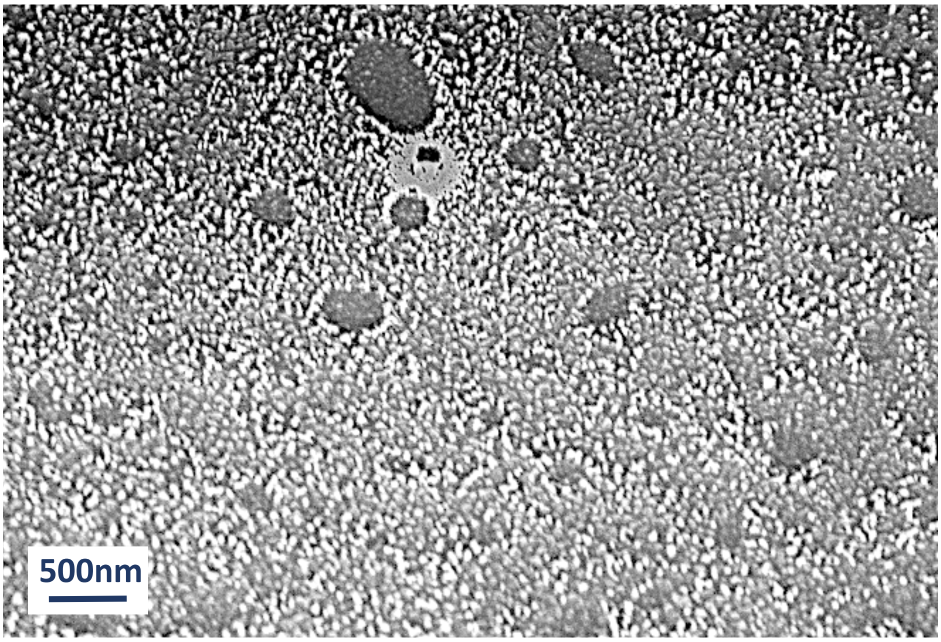

Figure 7.18 *SEM characterisation of iron oxide nanodots etched (sample 2). Tilt FESEM images taken at the sample edge are shown in a) and b). c) and d) show a FESEM image taken from the centre sample. The sample was snap cleaved along the centre to get a clear representation of the nanopillars.*

The SEM characterisation (Figure 7.18) showed the nanopillar formation for sample 2. Similar to sample 1, the surface is not as expected. Figure 7.18 a) and b) show the sample contains nanopillars around ~100nm, however the pillars again look over etched and there is a range of different height features, with some pillars being less than 20nm. Figure 7.18 c) shows that the surface is not uniform, the nanopillars are sparse and they are not in hexagonal arrays. Figure 7.18 d) shows a large-scale image with circular features observed on the surface. These features display no nanopillar structures and were observed across sample 1 and sample 2. Although not seen in the samples prior to etching, it is thought these features were a result of thickness variations in the BCP template, as seen previously. Figure 7.19 shows the thickness variations observed through SEM, which was discussed in chapter four. Since the inclusion process relies on the BCP template, variations in the BCP film would lead to variations in iron oxide formation. This is possibly the reason for the variations in nanopillar size observed across sample 1 and sample 2.

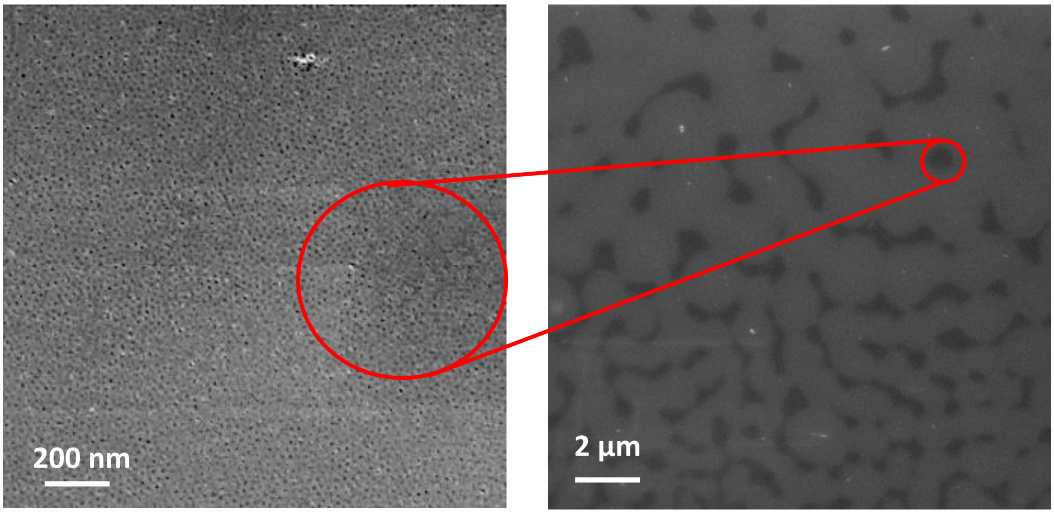

***Figure** 7.19 SEM Micrographs of PS – b – P4VP. a) and b) are the same sample imaged at different scales the difference in colour observed (marked by the red circle) is due to the difference in film thickness across the wafer that occurs during spin coating, not dewetting, as these areas are also patterned as seen in the SEM analysis.*

The surfaces prepared are not optimal as uniform nanopillars have not been fabricated. However, the substrate can still be used as a master to prepare polymer replicas. Replica molding of silicon features has been reported previously. Both Zhang and Chandra have reported sub-micron replica molding of silicon nanopillars using PDMS as a primary mold and photointiated curing of monomer for secondary mold.[156] However, little research of replica molding of sub-100nm features has been reported and therefore, the process must be investigated and optimised. Since the features are smaller than those found on cicada wings, the surface area is increased, therefore removal of polymer molds from the master can be problematic. To limit this effect, the silicon masters were deposited with trichloro (1H,1H,2H,2H-perfluoro-octyl) silane before polymer molding began. This made removal of the primary mold simple.

Using the protocols optimised in previously, molding of the silicon nanopillars (sample 1 and sample 2) was carried out. The silanisation of the silicon master made PPGDA primary mold removal straightforward. Figure 7.20 shows photographs of a) silicon master, b) primary mold, c) secondary mold.

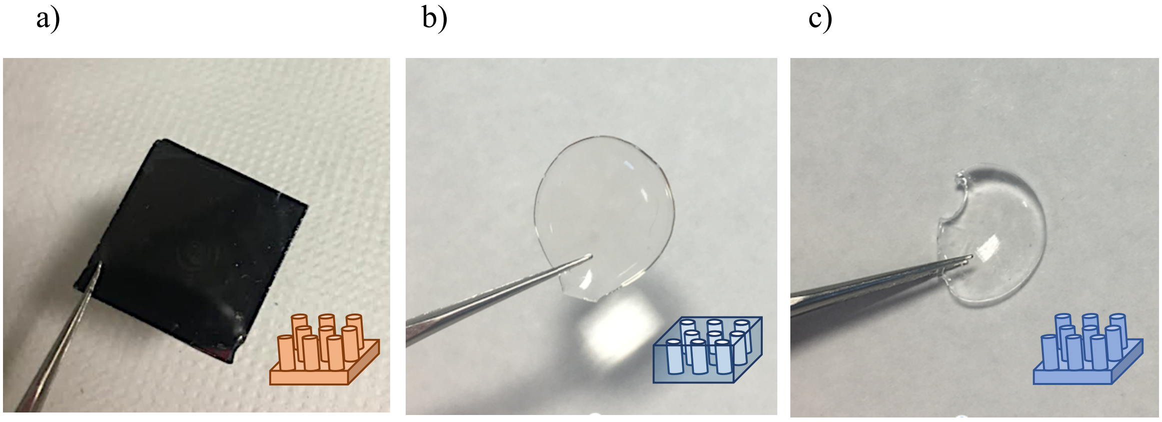

Figure 7.20 *Photographs of a) Silicon wafer that has been etched, b) primary mold, c) secondary mold. The inset shows a cartoon representation of the surface.*

To see if the replica molding was successful, secondary molds were characterised. SEM characterisation of the polymer surfaces presented previously was carried out by performing a gold deposition prior to imaging. This not only prevents charging of the material, but also provided protection for the polymer material from becoming thermally degraded by the electron beam. However, gold coating of these polymer samples was not possible due to the size of the features. Since the samples are sub-100nm, deposition was shown to cover the surface features and a SEM image showing accurate representation could not be obtained. Non-coated samples were shown be degraded by the electron beam even when imaged at low eV. For these reasons, AFM was used to characterise polymer replicas. Representative images are shown in Figure 7.21. Silicon AFM probes were used with a force constant of 40N/m and a resonance frequency of 300kHz in tapping mode.

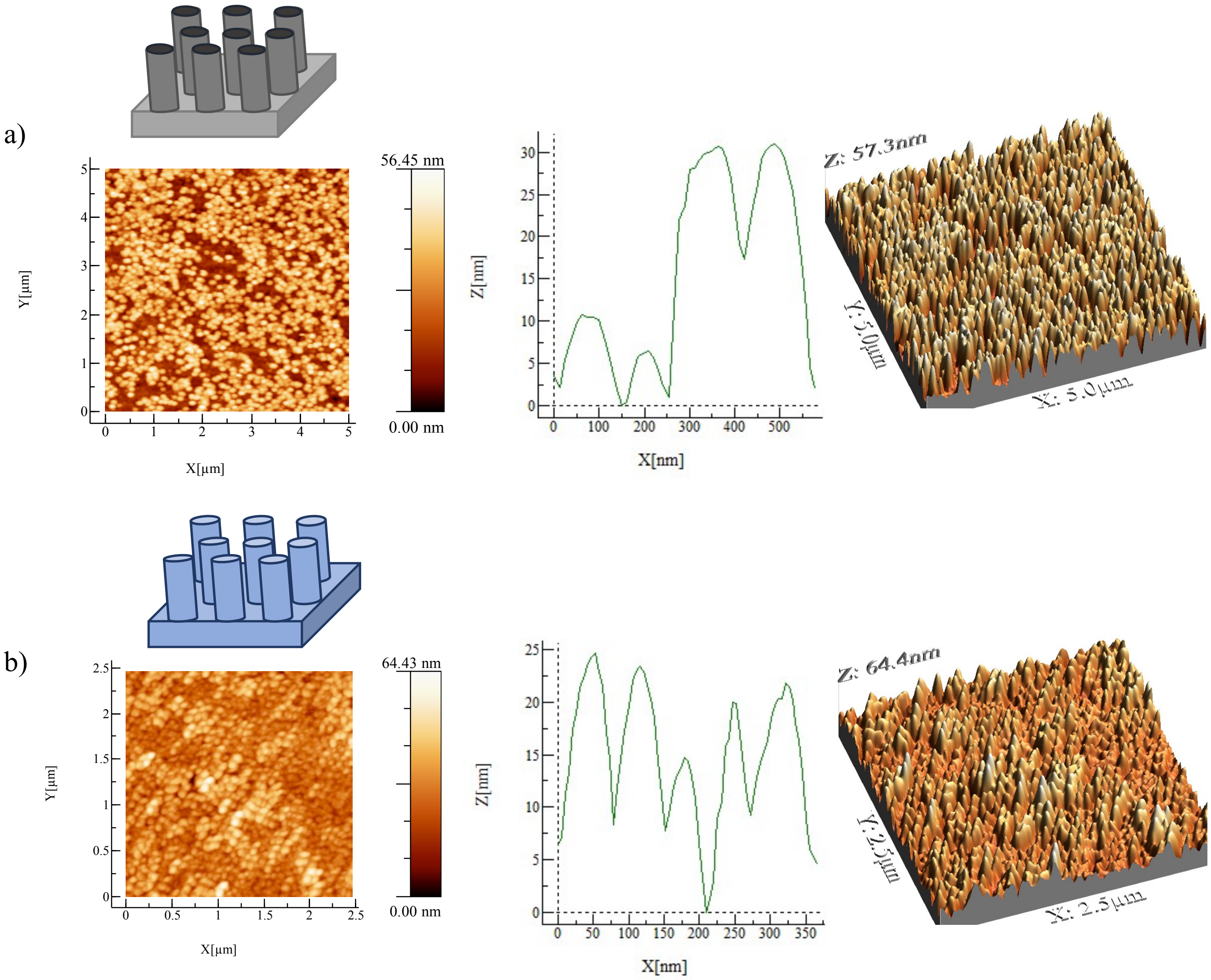

Figure 7.21 *a) AFM height image, profile and 3D image for silicon master sample 1. b) AFM height image, profile and 3D images for sample 1 PEGDA secondary mold.*

From the AFM characterisation, it can clearly be seen that the replica molding was successful. Figure 7.21 a) and b) shows the master and the PEGDA secondary mold for sample one. The difference in height, previously seen in the SEM images was seen here also. The AFM characterisation for sample 2 is shown below.

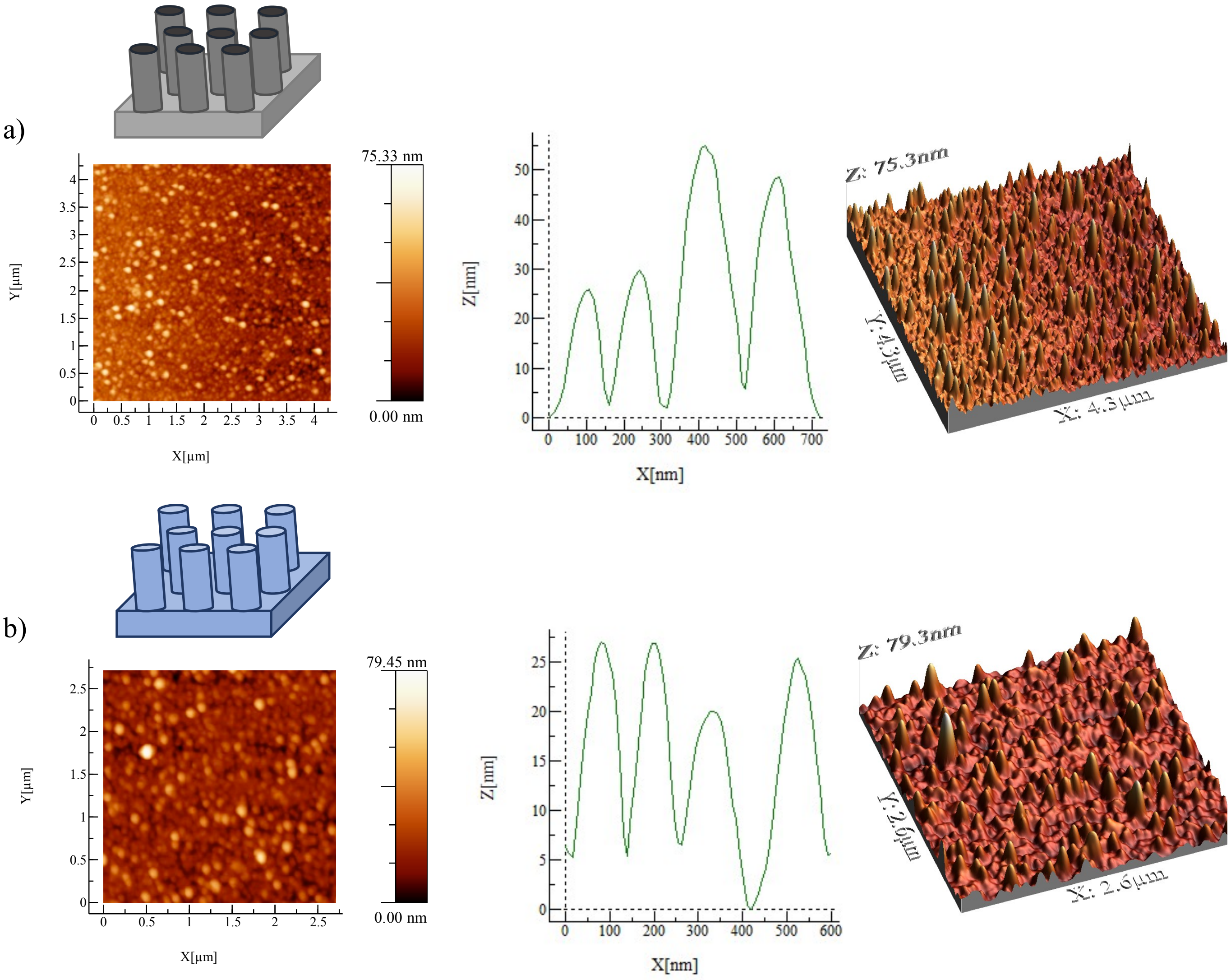

Figure 7.22 *a) AFM height image, profile and 3D image for silicon master sample 2. b) AFM height image, profile and 3D image for sample 2 PEGDA secondary mold.*

Figure 7.22 shows the master and PEGDA secondary mold for sample two. Again, the replica molding was successful as nanostructures of similar feature size were observed in the secondary mold.

For comparison Table 7.4 shows the average height calculated for each sample. The height measured by AFM is lower than what was reported using SEM. However, AFM is a more accurate representation of height as an average was taken over a minimum of three images.

Table 7.4 *Average height measurements for silicon nanopillars and PEGDA replicas*

Measurement	**Silicon nanopillars (sample 1)**	**PEGDA Replica (samples 1)**	**Silicon nanopillars (sample 2)**	**PEGDA Replica (samples 2)**
Height	29nm	28nm	54nm	51nm

Since AFM characterisation confirmed replica molding was successful, antibacterial activity could be investigated. These polymer molds were tested for antibacterial activity by collaborators in Technische Universitat (TU) Dresden. Following the protocol described in chapter three, polymer samples were adhered to a sterile petri dish and an *E. coli* SM2029 cell solution suspended in the dish; prepared as described in the method section. Samples were incubated at 30°C for 30 mins before undergoing washing steps. This was to ensure a standard coverage was obtained allowing for solid cell counting. The samples were tested in triplicate and compared to unpatterned PEGDA. Confocal fluorescence microscopy was used to investigate cell death on sample surfaces. The *E. coli* SM2029 cell is modified with green fluorescent protein (GFP) and fluoresces green. Propidium iodide was used to stain cells to investigate cell death or damage. This intercalating agent, which binds to DNA, cannot cross membranes of live cells, differentiating living, and dead or damaged cells. Figure 7.23 shows the results obtained by confocal fluorescence spectrometry.

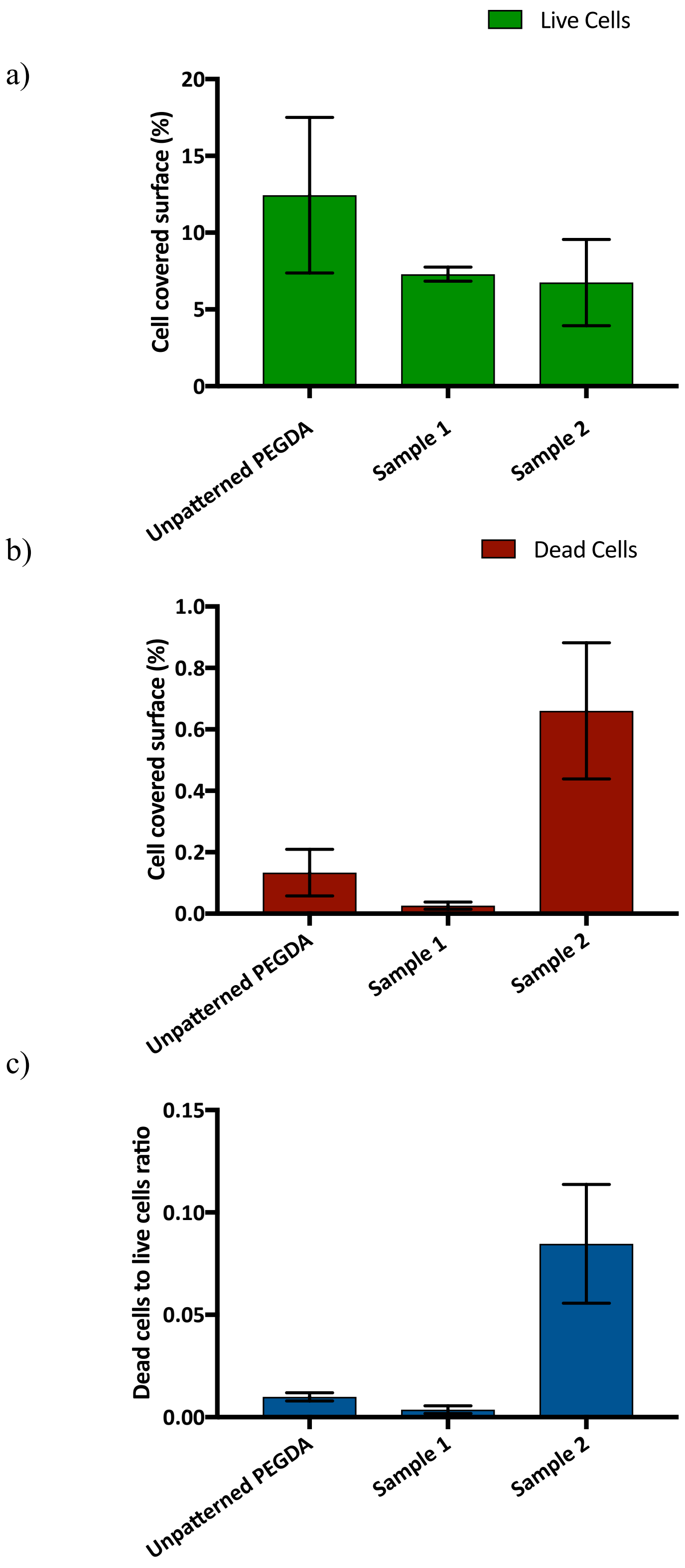

Figure 7.23 *a) Surface coverage of GFP expressing cells (live) after 30min contact. b) Surface coverage of propidium iodide stained cells (dead). c) Ratio of GFP: propidium iodide signals after dead/live cell staining.*

Figure 7.23 a) shows the surface coverage of GFP expressing cells (live cells). Both sample 1 and 2 had similar surface coverage of 7.2% and 6.7%, respectively. The unpatterned PEGDA had almost double the coverage with 12.4%. Figure 7.23 b) show the surface coverage of propidium iodide stained cells (dead cells). Here, sample 2 shows the highest number of dead cells with 0.6%. Samples 1 shows smaller percentage of dead cells than the unpatterned control at 0.02%, which was unusual. The ratio of dead to live cells for each sample is represented in Figure 7.23 c). Comparing these results to the work of Kelleher et al. who reported significant antibacterial activity on cicada wings when tested with *Psedomonas Fluoresens* bacterial cells,[59] the bacterial effect observed here is not as significant. In their bacterial testing, they observed much greater cell coverage within the 30 minute treatment; 20% cell surface coverage was observed with 4.5% being dead cells. Resulting in a dead to live cell ratio of 0.22, almost double than what is observed here.

Ivanova et al. investigated the bacterial activity of nanostructured black silicon and *Diplacodes Bipuntata* dragonfly wing. Although their surface treatment time was longer than what is reported here (3 hours), they reported significant activity on both surfaces. They determined the number of cells killed rather than expressing the ratio of dead to live cells. Both black silicon and the wings had comparable activity with a killing rate of ~450,000 cells min^{-1} cm^2. [168] This is twice the effect recorded on the surfaces describes herein. It is expected that the antibacterial effect is lessened on this surface due to poor coverage and uniformity of the nanostructures.

Nevertheless, it is clear from the bacterial testing that sample 2 showed the greatest antibacterial effect, when compared to unpatterned PEGDA and sample 1. Surprisingly, sample 1 activity was less than the unpatterned PEG. This could be a result of a number of factors:

1. The molds prepared are not fabricated from optimal masters, as previously mentioned. The molds contained areas that are not patterned and areas with collapsed pillars.
2. The height of the pillars on this mold do not exceed ~60nm, confirmed through the AFM characterisation.

There is a clear difference in the height of the samples and their antibacterial activity. This suggests that pillars with a range of heights, as seen in sample 1, are not appropriate for antibacterial surfaces. Figure 7.23 c) shows the ratio of dead to live cells for sample 2 is 26 times higher than sample 1. Again, this mold is not perfect as it contains areas which are unpatterned. The increase in antibacterial effect for sample 2 suggests that the height of the pillars seen in this sample contributes to increased cell death, since the only difference between sample 1 and sample 2 is the height of the pillars. Moreover, the height of these pillars could be controlled using the swelling properties of PEGDA and water, as demonstrated with the cicada wing PEGDA molds.

The consensus is that the mechanism responsible for cell death at the nanostructured surface is mechanical in nature. A clear understanding of the underlying mechanism is yet to be conclusively determined, with a number of proposed mechanisms being reported.[169-171] The complexity of microbial cells and the multitude of cell-surface interaction taking place has left this still under debate. It has been proposed that simple cell puncture by the nanopillars leads to cell death.[58] More recent advance show cell stretching across the nanostructured surface leads to cell rupture.[172, 173] However, more research is needed to obtain a conclusive understanding of the antibacterial effect nanopillars exhibit.

7.3 Conclusion

In this chapter, the successful replication of nanostructured cicada wings has been carried out by means of replica molding. Nanostructured gels of PEGDA, PEGDA 20% H_2O and PEGDA 40% H_2O have been prepared and characterised with SEM and AFM. The polymer structures showed excellent replica molding with nanopillar arrays seen across samples. Gels have the ability to swell and incorporate water into the matrix. To investigate how this swelling property would affect the nanostructured surface, liquid AFM was performed on the nanostructured gels. Height profiles were compared to the height of the air AFM. Results showed each gel underwent swelling and this influenced nanopillar dimensions, with PEGDA 40% H_2O showing a significant change of nanopillar height from 181nm -390nm. This finding has shown the ability to control nanopillar height in PEGDA gels by swelling with water.

Using the molding protocol optimised on cicada wings, replica molding of silicon nanopillars was carried out. Fabrication of silicon nanopillars was achieved by annealing PS – *b* – P4VP BCP thin film using the solvothermal annealing chamber. SEM and AFM characterisation of the BCP pattern revealed ideal templates with few defects and perfect hexagonal ordering. Using an iron nitrate inclusion process, these BCP templates were successfully converted to a hard mask forming an iron oxide nanodot array, verified by SEM and AFM analysis. Etching of these samples was carried out by Tyndall National Laboratory to produce samples with varying pillar heights; sample 1 (~28nm) and sample 2 (~49nm). The surface features were characterised with SEM and AFM, which showed that the surfaces had pillars of mixed heights, as well as regions that were unpatterned. It is believed that this is a result of the difference in BCP film thickness across the wafer. The original film thickness was recorded to be 18nm. The pillars were also seen to have isotropic properties and were collapsed in areas; a result of over etching.

Nevertheless, although not optimal, these surfaces were replica molded to see if nanoscale features could be molded using protocols previously optimised. This successful molding was characterised with AFM. The molds were then tested for antibacterial properties by collaborators in Technische Universitat Dresden. Results revealed that sample 2 (~49nm pillars) had an antibacterial effect when compared to sample 1 (~28nm pillars) and the control; unpatterned PEGDA. This key finding gives valuable information that will aid future work to develop antibacterial polymer surfaces.

7.4 Future work

It has been demonstrated that nanopillar height can be controlled using the swelling properties of gels, however it must now be investigated how the mechanical properties affect antibacterial activity. As the gel swells and incorporates water into the matrix, the structure will become soft and supple. Although among debate in literature, it is thought that the bacteria on cicada wings are killed by the nanostructure through impalement. If the nanostructure is soft, this impaling of bacteria could be hindered, thus resulting in less antibacterial activity. Therefore, bacterial cell testing on each polymer mold would be key to further understanding the antibacterial mechanism.

It is evident that improvement of silicon nanopillar masters in needed. Having a perfect master with uniform nanopillars would aid the fabrication of optimal polymer replicas. It was seen in the SEM characterisation that the silicon master showed evidence of over etching and regions that were unpatterned. It is possible these unpatterned regions were formed through differences in film thickness, where the over etching is caused by the hard mask material being too thin (4nm shown in AFM analysis). Therefore, changing the thickness of the original BCP thin film should resolve these issues. This will allow a higher concentration of iron nitrate to be infiltrated into the P4VP core, resulting in larger iron oxide nanodots, which will be robust for the etch step. It goes without saying that the bacterial cell testing must be repeated to see if the antibacterial effect could be increased. Since these experiments were carried out by collaborators, repeating this in the short-term is not possible. However, investigating antibacterial activity of these surface with *E. coli* SM2029 cells, as well as other Gram-negative bacteria, will be the subject of future work.

Summary

In this thesis, the set-up and optimisation of a state-of-the-art solvothermal annealing chamber has been presented. The aim to overcome the dewetting limitation associated with static annealing of PS – *b* – P4VP and develop a highly controllable process was achieved. The results presented show the effective reproducibility of BCP films without polymer dewetting. A wide range of dynamic solvothermal annealing conditions have been investigated with 30°C for 30 minute anneal presenting cylindrical patterns with features of an average pitch of 25.5nm ± 2.4nm and an average diameter of 21.3nm ± 3nm. This work draws parallel to the solvent annealing chambers seen in the literature,[40, 42] with the chamber herein having the ability to process four-inch wafer, unlike that what is seen in the literature thus far. Following the work of Gotrik et al. the hexagonal ordering of PS – *b* – P4VP was improved by implementing a reflectometer to record *in situ* swelling measurements and by increasing the speed of the quench step.[27]

The development of a selective plasma etch process for the removal of P4VP cores from PS – *b* – P4VP nanopatterned film has been demonstrated. To the best of our knowledge, this is the first time this has been exhibited. Results showed that a nitrogen plasma has selectivity for P4VP of 2.2:1. The work presented suggested that the position of the nitrogen in the aromatic ring plays a key role in this selectivity, which was investigated further using *in situ* plasma etching and XPS spectrometry. Results confirmed the quick removal of P4VP by a nitrogen plasma when compared to the sterically hindered P2VP, concluding that the position of the nitrogen in the pyridine molecule is related to etch mechanism in nitrogen plasmas. XPS data revealed the incorporation of nitrogen and oxygen into the polymer film during the etch process, this correlates to the work carried out by Wagner et al. who also found the incorporation of nitrogen post plasma treatment. [138]

Motivated by work carried out by Oria et al. the aim to modify a preferential PS brush layer with oxygen plasma was investigated.[140] The intention being to convert PS from a preferential brush layer to a neutral brush layer using plasma. A detailed investigation into oxygen plasma treatment of PS thin films has been carried out. Changes in wettability, surface energy and film thickness post plasma treatment have been recorded. Results show that treating PS brush layers with oxygen plasmas significantly changes the wettability and surface energy. Initial BCP annealing on plasma treated films showed that plasma treated PS brush layer influenced PS – *b* – PMMA orientation. This work highlights the importance of controlling surface energy and functionality for BCP orientation. This preliminary results merits further investigation as BCP annealing on plasma treated films suggested a change in BCP orientation, similar to that seen by Oria et al.[140]

Cicada wings have recently been of interest due to their antibacterial properties exhibited by the nanopillar surface.[57, 150] These natural surfaces have been previously characterised and investigated,[59, 174] however, replica molding of such features has not been demonstrated to our knowledge. Herein, the successful molding of nanostructured cicada wings has been carried out by means of replica molding. Nanostructured gels of PEGDA, PEGDA 20% H_2O and PEGDA 40% H_2O have been prepared and characterised with SEM and AFM. The polymer structures showed excellent replica molding with nanopillar arrays seen across samples. Gels have the ability to swell and incorporate water into the matrix. To investigate how this swelling property would affect the nanostructured surface, liquid AFM was performed on the nanostructured gels. Height profiles were compared to the height profiles of the air AFM. Results showed each gel underwent swelling and this influenced nanopillar dimensions, with PEGDA 40% H_2O showing a significant change of nanopillar height from 181nm - 390nm. This finding has shown the ability to control nanopillar height in PEGDA gels by swelling with water. To our knowledge this is the first time this has been demonstrated using replica molded cicada wings. This replica molding and swelling properties corroborates to the work carried out by Kelleher et al. who demonstrated the swelling properties of molded trench structures.[167]

Using the molding protocol optimised on cicada wings, replica molding of silicon nanopillars was carried out. Little replica molding of sub-100nm features has been demonstrated in the literature. Fabrication of silicon nanopillars was achieved by annealing PS – *b* – P4VP BCP thin film using the solvothermal annealing chamber. SEM and AFM characterisation of the BCP pattern revealed ideal templates with few defects and perfect hexagonal ordering. These BCP templates were comparable to the excellent microphased arrays fabricated by Park et al.[40] Using an iron nitrate inclusion process, these BCP templates were successfully converted to a hard mask forming an iron oxide nanodot array, verified by SEM and AFM analysis. Etching of these samples was carried out by Tyndall National Laboratory to produce samples with varying pillar heights; sample 1 (~28nm) and sample 2 (~49nm). The surface features were characterised with SEM and AFM, unlike what was demonstrated in the literature, characterisation revealed that the surfaces had pillars of mixed heights, as well as regions that were unpatterned. It is believed that this is a result of the difference in BCP film thickness across the wafer prior to hardmask inclusion. The pillars were also seen to have isotropic properties and were collapsed in areas; a result of over etching.

These silicon nanopillars were replica molded to see if nanoscale features could be molded using protocols optimised using the cicada wings. This successful molding was characterised with AFM. The molds were then tested for antibacterial properties by collaborators in Technische Universitat Dresden. Although not as significant as demonstrated by Kelleher et al.,[59] results revealed that sample 2 (~49nm pillars) had an antibacterial effect when compared to sample 1 (~28nm pillars) and the control; unpatterned PEGDA. This key finding gives valuable information that will aid future work to develop antibacterial polymer surfaces.

References

1. G. Moore, *Electronics,* 1965, **38,** 114-117.
2. R. A. Robison, *World Neurosurgery,* 2012, **78,** 399-403.
3. S. E. Thompson and S. Parthasarathy, *Materials Today,* 2006, **9,** 20-25.
4. W. Holt, IEEE International Solid-State Circuits Conference, 2016,1, 8-135
5. B. Wu and A. Kumar, *Journal of Vacuum Science and Technology,* 2007, **25,**1743-1761.
6. M. A. Morris, *Microelectron Eng,* 2015, **132,** 207-217.
7. G. E. Molau, *Colloidal and Morphological Behavior of Block and Graft Copolymers,* Springer, 1970.
8. F. S. Bates, *Annu. Rev. Phys. Chem.,* 1990, **41,** 525-557.
9. B. R. Gallot, *Preparation and Study of Block Copolymers with Ordered Structures,* Springer, Berlin Heidelberg, 1978, p. 85.
10. I. W. Hamley, *Developments in Block Copolymer Science and Technology,* John Wiley & Sons, 2004.
11. W. Hamley, *Progress in Polymer Science,* 2009, **34,** 1161-1210.
12. L. Leibler, *ACS Macromolecules,* 1980, **30,** 1602-1617.
13. Y. Mai and A. Eisenberg, *Chem. Soc. Rev.,* 2012, **41,** 5969-5985.
14. R. A. Segalman, *Materials Science and Engineering: R: Reports,* 2005, **48,** 191-226.
15. P. Mansky, P. Haikin and E. L. Thomas, *Journal of Materials Science,* 1995, **30,** 1987-1992.
16. P. Mansky, C. K. Harrison, P. M. Chaikin, R. A. Register and N. Yao, *Appl. Phys. Lett.,* 1996, **68,** 2586-2588.
17. S. B. Darling, *Progress in Polymer Science,* 2007, **32,** 1152-1204.
18. S. Ji, L. Wan, C. Liu and P. F. Nealey, *Progress in Polymer Science,* .
19. S. O. Kim, H. H. Solak, M. P. Stoykovich, N. J. Ferrier, J. J. De Pablo and P. F. Nealey, *Nature,* 2003, **424,** 411-414.
20. M. P. Stoykovich, H. Kang, K. C. Daoulas, G. Liu, C. -. Liu, J. J. De Pablo, M. Müller and P. F. Nealey, *ACS Nano,* 2007, **1,** 168-175.
21. E. W. Edwards, M. F. Montague, H. H. Solak, C. J. Hawker and P. F. Nealey, *Adv Mater,* 2004, **16,** 1315-1319.
22. C. Liu, E. Han, M. S. Onses, C. J. Thode, S. Ji, P. Gopalan and P. F. Nealey, *Macromolecules,* 2011, **44,** 1876-1885.
23. P. Mansky, Y. Liu, E. Huang, T. P. Russell and C. Hawker, *Science,* 1997, **275,** 1458-1460.
24. J. Bang, U. Jeong, D. Y. Ryu, T. P. Russell and C. J. Hawker, *Advanced Materials,* 2009, **21,** 4769-4792.
25. C. M. Bates, J. R. Strahan, L. J. Santos, B. K. Mueller, B. O. Bamgbade, J. A. Lee, J. M. Katzenstein, C. J. Ellison and C. G. Willson, *Langmuir,* 2011, **27,** 2000-2006.
26. D. Y. Ryu, K. Shin, E. Drockenmuller, C. J. Hawker and T. P. Russell, *Science,* 2005, **308,** 236-239.

27. S. Ji, C. -. Liu, J. G. Son, K. Gotrik, G. S. W. Craig, P. Gopalan, F. J. Himpsel, K. Char and P. F. Nealey, *Macromolecules,* 2008, **41,** 9098-9103.
28. R. D. Peters, X. M. Yang, T. K. Kim, B. H. Sohn and P. F. Nealey, *Langmuir,* 2000, **16,** 4625-4631.
29. J. Y. Cheng, A. M. Mayes and C. A. Ross, *Nat. Mater.,* 2004, **3,** 823-828.
30. D. Borah, S. Rassapa, M. T. Shaw, R. G. Hobbs, N. Petkov, M. Schmidt, J. D. Holmes and M. A. Morris, *J. Mater. Chem. C,* 2013, **1,** 1192-1196.
31. S. Xiao, X. Yang, E. W. Edwards, Y. -. La and P. F. Nealey, *Nanotechnology,* 2005, **16,** S329.
32. D. Petera and M. Muthukumar, *J. Chem. Phys,* 1997, **107,** 9640-9644.
33. W. Li and M. Müller, *Progress in Polymer Science,* 2016, **54–55,** 47-75.
34. E. W. Edwards, M. Müller, M. P. Stoykovich, H. H. Solak, J. J. De Pablo and P. F. Nealey, *Macromolecules,* 2007, **40,** 90-96.
35. D. Borah, M. T. Shaw, J. D. Holmes and M. A. Morris, *ACS Appl. Mater. Interfaces,* 2013, **5,** 2004-2012.
36. J. W. Jeong, Y. H. Hur, H. -. Kim, J. M. Kim, W. I. Park, M. J. Kim, B. J. Kim and Y. S. Jung, *ACS Nano,* 2013, **7,** 6747-6757.
37. W. I. Park, K. Kim, H. -. Jang, J. W. Jeong, J. M. Kim, J. Choi, J. H. Park and Y. S. Jung, *Small,* 2012, **8,** 3762-3768.
38. F. Ferrarese Lupi, T. J. Giammaria, M. Ceresoli, G. Seguini, K. Sparnacci, D. Antonioli, V. Gianotti, M. Laus and M. Perego, *Nanotechnology,* 2013, **24,** 11-31.
39. H. Yokoyama, *Materials Science and Engineering: R: Reports,* 2006, **53,** 199-248.
40. S. Park, B. Kim, J. Xu, T. Hofmann, B. M. Ocko and T. P. Russell, *Macromolecules,* 2009, **42,** 1278-1284.
41. S. H. Kim, M. J. Misner, T. Xu, M. Kimura and T. P. Russell, *Adv Mater,* 2004, **16,** 226-231.
42. K. W. Gotrik and C. A. Ross, *Nano Lett.,* 2013, **13,** 5117-5122.
43. M. Y. Paik, J. K. Bosworth, D. -. Smilges, E. L. Schwartz, X. Andre and C. K. Ober, *Macromolecules,* 2010, **43,** 4253-4260.
44. K. Tu, W. Bai, G. Liontos, K. Ntetsikas, A Avgeropoulos and C. A. Ross, *Nanotechnology,* 2015, **26,** 375301.
45. G. B. Kang, S. -. Kim, Y. T. Kim and J. H. Park, *Curr. Appl. Phys.,* 2009, **9,** S84.
46. C. Cummins, D. Borah, S. Rasappa, A. Chaudhari, T. Ghoshal, B. M. D. O'Driscoll, P. Carolan, N. Petkov, J. D. Holmes and M. A. Morris, *J. Mater. Chem. C,* 2013, **1,** 7941-7951.
47. P. Mokarian-Tabari, R. Senthamaraikannan, C. Glynn, T. W. Collins, C. Cummins, D. Nugent, C. O'Dwyer and M. A. Morris, *Nano Letters,* 2017, **17,** 2973-2978.
48. M. W. Schulze, C. Sinturel and M. A. Hillmyer, *ACS Macro Lett.,* 2015, **4,** 1027-1032.

49. T. Ghoshal, R. Senthamaraikannan, M. T. Shaw, J. D. Holmes and M. A. Morris, *Nanoscale,* 2012, **4,** 7743-7750.
50. J. Gallo, M. Holinka and C. S. Moucha, *International Journal of Molecular Sciences,* 2014, **15,** 13849-13880.
51. T. Wei, Q. Yu, W. Zhan and H. Chen, *Advanced Healthcare Materials,* 2016, **5,** 449-456.
52. A. Tripathy, P. Sen, B. Su and W. H. Briscoe, *Advances in Colloid and Interface Science,* 2017, **248,** 85-104.
53. T. Huang, F. P. Yu, G. A. McFeters and P. S. Stewart, *Applied and Environmental Microbiology,* 1995, **61,** 2252-2256.
54. J. N. Anderl, M. J. Franklin and P. S. Stewart, *Antimicrobial Agents and Chemotherapy,* 2000, **44,** 1818-1824.
55. J. W. Costerton, B. Ellis, K. Lam, F. Johnson and A. E. Khoury, 1994, **38,** 2803-2809.
56. D. Davies, *Nature Reviews Drug Discovery,* 2003, **2,** 114-122.
57. A. Elbourne, R. J. Crawford and E. P. Ivanova, *Journal of Colloid and Interface Science,* 2017, **508,** 603-616.
58. E. P. Ivanova, J. Hasan, H. K. Webb, V. K. Truong, G. S. Watson, J. A. Watson, V. A. Baulin, S. Pogodin, J. Y. Wang, M. J. Tobin, C. Löbbe and R. J. Crawford, *Small,* 2012, **8,** 2489-2494.
59. S. M. Kelleher, O. Habimana, J. Lawler, B. O'reilly, S. Daniels, E. Casey and A. Cowley, *ACS Appl. Mater. Interfaces,* 2016, **8,** 14966-14974.
60. G. S. Watson, D. W. Green, L. Schwarzkopf, X. Li, B. W. Cribb, S. Myhra and J. A. Watson, *Acta Biomaterialia,* 2015, **21,** 109-122.
61. X. Zhao, Y. Xia and G. Whitesides, *Journal of Materials Chemistry,* 1997, **7,** 169-174.
62. Y. Xia and G. M. Whitesides, *Annual Review of Materials Science,* 1998, **28,** 153-184.
63. Y. Xia, E. Kim, X. Zhao, J. Rogers, M. Prentiss and G. Whitesides, *Science,* 1996, **273,** 347-349.
64. Y. Xia, J. J. McClelland, R. Gupta, . Quin, X. Zhao, L. L. Sohn, R. J Celotta and G. M Whitesides, 1997, **1,** 147-149.
65. S. S. Williams, S. Retterer, R. Lopez, R. Ruiz, E. T. Samulski and J. M. DeSimone, *Nano Letters,* 2010, **10,** 1421.
66. T. Senn, J. P. Esquivel, M. Lörgen, N. Sabaté and B. Löchel, *Journal of Micromechanics and Microengineering,* 2010, **20,** 115012.
67. T. Senn, J. P. Esquivel, N. Sabaté and B. Löchel, *Microelectronic Engineering,* 2011, **88,** 3043-3048.
68. S. Kang, T. Tai and T. Fang, *Current Applied Physics,* 2010, **10,** 625-630.
69. K. Park, K. J. Cha, I. Han, D. Shin, D. Cho, S. Lee and D. S. Kim, *Macromolecular Bioscience,* 2012, **12,** 1480-1489.
70. Y. Wei, X. Mo, P. Zhang, Y. Li, J. Liao, Y. Li, J. Zhang, C. Ning, S. Wang, X. Deng and L. Jiang, *ACS Nano,* 2017, **11,** 5915-5924.

71. W. A. Phillip, B. O'Neill, M. Rodwogin, M. A. Hillmyer and E. L. Cussler, *ACS Appl. Mater. Interfaces,* 2010, **2,** 847-853.
72. W. Song, B. Gan, T. Jiang, Y. Zhang, A. Yu, H. Yuan, N. Chen, C. Sun and Z. L. Wang, *ACS Nano,* 2016, **10,** 8097-8103.
73. C. Chiappini, J. O Martinez, E. De Rosa, C. S Almeida, E.Tasciotti and M. M Stevens, *ACS Nano,* 2015, **9,** 5500-5509.
74. T. Harland and I. Eugene, *Handbook of Ellipsometry,* William Andrew Publishing, Norwich, NY 13815, United States of America, 2005.
75. J.A. Woollam Co, https://www.jawoollam.com/resources/ellipsometry-tutorial/what-is-ellipsometry, (accessed 03/01/2018).
76. Hamamatsu Photonics K.K, http://www.hamamatsu.com/us/en/technology/innovation/spectroscopic/index.html, (accessed 03/01/2018).
77. R. Tadmor, *Langmuir,* 2004, **20,** 7659-7664.
78. H. D. Gesser and P. Krause, *J. Chem. Educ.,* 2000, **77,** 58-59.
79. Kruss Inc, https://www.kruss.de/services/education-theory/glossary/surfacefree-energy/, (accessed 27/10/2016).
80. L. Gao and T. J. McCarthy, *Langmuir,* 2006, **22,** 6234-6237.
81. H. B. Eral and J. M. Oh, *Colloid Polym. Sci.,* 2013, **291,** 247-260.
82. D. H. Kaelble, *The Journal of Adhesion,* 1970, **2,** 66-81.
83. D. K. Owens and R. C. Wendt, *J Appl Polym Sci,* 1969, **13,** 1741-1747.
84. G. Binnig, C. F. Quate and C. Gerber, *Phys. Rev. Lett.,* 1986, **56,** 930-935.
85. R. Daniel and H. Paul, *Physics Today,* 1990, **43,** 23-30.
86. B. Bhushan and O. Marti, in *Scanning Probe Microscopy, Scanning Probe Microscopy,* Springer, 2010.
87. Bruker Nano Inc., http://www.brukerafmprobes.com/, (accessed 25/07/2016).
88. Wikipedia.com, https://commons.wikimedia.org/wiki/File:AFM_schematic_(EN).svg, (accessed 26/07/2016).
89. C. A. J. Putman, Van der Werf, Kees O, B. G. De Grooth, N. F. Van Hulst and J. Greve, *Appl. Phys. Lett.,* 1994, **64,** 2454-2456.
90. R. Motamedi and P. M. Wood-Adams, *Sensors,* 2008, **8,** 5927-5941.
91. Nanoscale Function Group, http://www.nanofunction.org/, (accessed 27/09/2017)
92. R. F. Egerton, in *The Scanning Electron Microscope, The Scanning Electron Microscope,* Springer, 2005.
93. Encyclopedia Britannica Inc, https://www.britannica.com/technology/scanning-electron-microscope, (accessed 26/07/2016).
94. Nanoscience Instruments, http://www.nanoscience.com/technology/semtechnology/,(accessed 27/07/2016).
95. wikipedia.com, https://en.wikipedia.org/wiki/Electron_microscope, (accessed 27/07/2016).

96. The photoelectron effect, http://drgstoothpix.com/2012/10/31/attenuation-photoelectric-effect/, (accessed 03/01/2018).

97. D. P. Woodruff, *Modern Techniques of Surface Science,* Cambridge university press, 2016.

98. S. Hüfner, *Photoelectron Spectroscopy: Principles and Applications,* Springer Science & Business Media, 2013.

99. J. F. Watts and J. Wolstenholme, Wiley Online Library, 2004.

100. S. R. Leadley and J. F. Watts, Journal of Electron Spectroscopy and Related, Phenomena, 1997, 85, 107-121.

101. Physical Electronics, https://www.phi.com/surface-analysistechniques/xps-esca.html, (accessed 27/07/2016).

102. Benninghoven, F. G. Rudenauer and H. W. Werner, 1987.

103. P. Williams, *Applied Atomic Collision Physics: Condensed Matter,* 2013, **4,** 327-377.

104. London Centre of Nanotechnology, https://www.londonnano.com/sites/default/files/uploads/research/highlights/Time%20of%20Flight%2CSecondary%20Ion%20Mass%20Spectroscopy%20%28SIMS%29.pdf (accessed 09/12/2016).

105. J. Greener, B. Abbasi and E. Kumacheva, *Lab Chip,* 2010, **10,** 1561-1566.

106. Attenuated total reflectance, https://en.wikipedia.org/w/index.php?title=Attenuated_total_reflectance&oldid=808087172, (accessed 03/01/2018).

107. J. Shin and J. Mazumder, *Journal of Laser Applications,* 2016, **28,** 022008.

108. Kolpakov, P. Kudrna and M. Tich, *Proc. of 20th Annual Conference of Doctoral Students,* 2011, **2,** 180-185.

109. G. Alberda van Ekenstein, R. Meyboom, G. Brinke and O. Ikkala, *Macromolecules,* 2000, **33,** 3752-3756.

110. C. J. Clarke, A. Eisenberg, J. La Scala, M. H. Rafailovich, J. Sokolov, Z. Li, S. Qu, D. Nguyen, S. A. Schwarz and Y. Strzhemechny, *Macromolecules,* 1997, **30,** 4184-4188.

111. W. Zha, C. D. Han, D. H. Lee, S. H. Han, J. K. Kim, J. H. Kang and C. Park, *Macromolecules,* 2007, **40,** 2109-2119.

112. R. Lundy, S. P. Flynn, C. Cummins, S. M. Kelleher, M. N. Collins, E. Dalton, S. Daniels, M. A. Morris and R. Enright, *Physical Chemistry Chemical Physics,* 2017, 2805-2815.

113. R. De Oliveira, D. Albuquerque, F. L. Leite, F. M. Yamaji and T. Cruz, *Measurement of the Nanoscale Roughness by Atomic Force Microscopy: Basic Principles and Applications,* INTECH Open Access Publisher, 2012.

114. H. Yokoyama, *Materials Science and Engineering: R: Reports,* 2006, **53,** 199-248.

115. J. Won Jeong, W. I. Park, M. Kim, C. A. Ross and Y. S. Jung, *Nano Letters,* 2011, **11,** 4095-4101.

116. R. Guo, H. Huang, Y. Chen, Y. Gong, B. Du and T. He, *Macromolecules,* 2008, **41,** 890-900.

117. E. O. Ningrum, W. Lin and C. Lo, *Polymer Engineering & Science,* 2011, **51,** 1339-1346.
118. J. You, S. Zhang, G. Huang, T. Shi and Y. Li, *The Journal of Chemical Physics,* 2013, **138,** 244907.
119. K. Mori, H. Hasegawa and T. Hashimoto, *Polymer,* 1990, **31,** 2368-2376.
120. D. Kashchiev, *Nucleation,* Butterworth-Heinemann, 2000.
121. R. Seemann, S. Herminghaus and K. Jacobs, *Phys. Rev. Lett.,* 2001, **86,** 5534-5537.
122. R. Xie, A. Karim, J. F. Douglas, C. C. Han and R. A. Weiss, *Phys. Rev. Lett.,* 1998, **81,** 1251-1254.
123. S. Park, B. Kim, J. Xu, T. Hofmann, B. M. Ocko and T. P. Russell, *Macromolecules,* 2009, **42,** 1278-1284.
124. K. W. Gotrik, A. F. Hannon, J. G. Son, B. Keller, A. Alexander-Katz and C. A. Ross, *ACS Nano,* 2012, **6,** 8052-8059.
125. K. W. Gotrik and C. A. Ross, *Nano Letters,* 2013, **13,** 5117-5122.
126. G. Riess, *Progress in Polymer Science,* 2003, **28,** 1107-1170.
127. C. Cummins, T. Ghoshal, J. D. Holmes and M. A. Morris, *Adv Mater,* 2016, 5586-5618.
128. T. Ghoshal, R. Senthamaraikannan, M. T. Shaw, J. D. Holmes and M. A. Morris, *Adv Mater,* 2014, **26,** 1207-1216.
129. J. Yin, X. Yao, J. Liou, W. Sun, Y. Sun Y. Wang, *ACS Nano,* 2013, **7,** 9961-9974.
130. Chaudhari, T. Ghoshal, M. T. Shaw, C. Cummins, D. Borah, J. D. Holmes and M. A. Morris, *Advances in Patterning Materials and Processes Xxxi,* 2014, **9051,** 905110.
131. N. Layadi, J. I. Colonell and J. T. C. Lee, *Bell Labs Technical Journal,* 1999, **4,** 155-171.
132. D. B. Graves, *IEEE Transactions on Plasma Science,* 1994, **22,** 31-42.
133. M. Quirk and J. Serda, *Semiconductor Manufacturing Technology,* Prentice Hall Upper Saddle River, NJ, 2001.
134. F. D. Egitto, *Pure and Applied Chemistry,* 1990, **62,** 1699-1708.
135. G. Hong, A. S. Holmes and M. E. Heaton, *Dtip,* 2003, 268-271.
136. Vesel and T. Semenic, *Materials and Technology,* 2012, **46,** 227-231.
137. Zaitsev, A. Lacoste, F. Poncin-Epaillard, A. Bès and D. Debarnot, *Surface and Coatings Technology,* 2017, **330,** 196-203.
138. Wagner, D. Fairbrother and F. Reniers, *Plasmas and Polymers,* 2003, **8,** 119-134.
139. M. R. Sanchis, O. Calvo, O. Fenollar, D. Garcia and R. Balart, *Polymer Testing,* 2008, **27,** 75-83.
140. L. Oria, A. Ruiz de Luzuriaga, J. A. Alduncin and F. Perez-Murano, *Microelectronic Engineering,* 2013, **110,** 234-240.
141. T. Murakami, S. Kuroda and Z. Osawa, *J. Colloid Interface Sci.,* 1998, **202,** 37-44.
142. M. Tsuchida and Z. Osawa, *Colloid Polym Sci,* 1994, **272,** 770-776.

143. Larsson and H. Dérand, *Journal of Colloid and Interface Science,* 2002, **246,** 214-221.

144. Vesel, *Surface and Coatings Technology,* 2010, **205,** 490-497.

145. C. Dupont-Gillain, Y. Adriaensen, S. Derclaye and P. G. Rouxhet, *Langmuir,* 2000, **16,** 8194-8200.

146. Vesel, I. Junkar, U. Cvelbar, J. Kovac and M. Mozetic, *Surf. Interface Anal.,* 2008, **40,** 1444-1453.

147. F. Walther, P. Davydovskaya, S. Zürcher, M. Kaiser, H. Herberg, A. M. Gigler and R. W. Stark, *Journal of Micromechanics and Microengineering,* 2007, **17,** 524-531.

148. E. Huang, T. P. Russell, C. Harrison, P. M. Chaikin, R. A. Register, C. J. Hawker and J. Mays, *Macromolecules,* 1998, **31,** 7641-7650.

149. In, Y. La, S. Park, P. F. Nealey and P. Gopalan, *Langmuir:The ACS Journal of Surfaces and Colloids,* 2006, **22,** 7855-7860.

150. J. Hasan, R. J. Crawford and E. P. Ivanova, *Trends in Biotechnology,* 2013, **31,** 295-304.

151. S. M. Kelleher, O. Habimana, J. Lawler, B. O'reilly, S. Daniels, E. Casey and A. Cowley, *ACS Appl. Mater. Interfaces,* 2016, **8,** 14966-14974.

152. H. Chen, D. Che, X. Zhang, Y. Yue and D. Zhang, *Technical Note,* 2015, **25,** 017002.

153. W. Green, K. K. Lee, J. A. Watson, H. Kim, K. Yoon, E. Kim, J. Lee, G. S. Watson and H. Jung, *Scientific Reports,* 2017, **7,** 41023.

154. S. Hong, J. Hwang and H. Lee, *Nanotechnology,* 2009, **20,** 385303.

155. H. Xie, H. Huang and Y. Peng, *Nanoscale,* 2017, **9,** 11951-11958.

156. Y. Zhang, C. Lo, J. A. Taylor and S. Yang, *Langmuir,* 2006, **22,** 8595-8601.

157. S. Kobayashi and K. Millen, *Encyclopedia of Polymeric Nanomaterials,* Springer, 2015.

158. Priola, G. Gozzelino, F. Ferrero and G. Malucelli, *Polymer,* 1993, **34,** 3653-3657.

159. G. Malucelli, G. Gozzelino, F. Ferrero, R. Bongiovanni and A. Priola, *J Appl Polym Sci,* 1997, **65,** 491-497.

160. K. Studer, C. Decker, E. Beck and R. Schwalm, *Progress in Organic Coatings,* 2003, **48,** 92-100.

161. G. M. Cruise, D. S. Scharp and J. A. Hubbell, *Biomaterials,* 1998, **19,** 1287-1294.

162. N. C. Padmavathi and P. R. Chatterji, *Macromolecules,* 1996, **29,** 1976-1979.

163. S. Kelleher, A. Jongerius, A. Loebus, C. Strehmel, Z. Zhang and M. C. Lensen, *Advanced Engineering Materials,* 2012, **14,** 56-66.

164. M. D. Abrmoff, P. J. Magalhes and S. J. Ram, *Biophoton Int.,* 2004, **11,** 36-42.

165. P. J. Flory and J. Rehner Jr, *J. Chem. Phys.,* 1943, **11,** 512-520.

166. L. M. Lucht and N. A. Peppas, *Chem. Soc. Prepr. Div. Fuel Chem,* 1984, **19,** 213-219.

167. S. M. Kelleher, Z. Zhang, A. Lbus, C. Strehmel and M. C. Lensen, *Biomaterials Science,* 2014, **2,** 410-418.

168. P. Ivanova, J. Hasan, H. K. Webb, G. Gervinskas, S. Juodkazis, V. K. Truong, A. H. F. Wu, R. N. Lamb, V. A. Baulin, G. S. Watson, J. A. Watson, D. E. Mainwaring and R. J. Crawford, *Nat Commun,* 2013, **4,** 572-579.
169. T. Diu, N. Faruqui, T. Sjöström, B. Lamarre, H. F. Jenkinson, B. Su and M. G. Ryadnov, *Sci Rep,* 2014, **4,** 7122.
170. Xue, J. Liu, L. Guo, L. Zhang and Q. Li, *J. Theor. Biol.,* 2015, **385,** 1-7.
171. S. Pogodin, J. Hasan, V. Baulin, H. Webb, V. Truong, T. Phong Nguyen, V. Boshkovikj, C. Fluke, G. Watson, J. Watson, R. Crawford and E. Ivanova, *Biophysical Journal,* 2013, **104,** 835-840.
172. X. Li and T. Chen, *Phys. Rev. E,* 2016, **93,** 052419.
173. X. Li, *Pccp,* The Royal Society of Chemistry, 2008.
174. P. Ivanova, J. Hasan, H. K. Webb, V. K. Truong, G. S. Watson, J. A. Watson, V. A. Baulin, S. Pogodin, J. Y. Wang, M. J. Tobin, C. Löbbe and R. J. Crawford, *Small,* 2012, **8,** 2489-2494.